CONTROLLING THE NEAR-WAKE OF A CIRCULAR CYLINDER WITH A SINGLE, LARGE-SCALE TRIPWIRE

by

Tayfun Besim Aydin

A thesis submitted in conformity with the requirements
for the degree of Doctor of Philosophy

Graduate Department of Aerospace Science and Engineering
University of Toronto

Controlling the Near-Wake of a Circular Cylinder with a Single, Large-Scale Tripwire

Tayfun Besim Aydin

Doctor of Philosophy

Graduate Department of Aerospace Science and Engineering
University of Toronto

2014

Abstract

Control of the flow past a circular cylinder using a single tripwire on its surface has been studied experimentally as a function of the wire angular location for different wire-to-cylinder diameter ratios ($0.029 \leq d/D \leq 0.059$) and Reynolds numbers ($5{,}000 \leq Re_D \leq 30{,}000$). The use of an endplate with a sharp leading edge on each end of the cylinder yields adequate level of quasi two-dimensionality in the near wake.

For each Reynolds number and wire size considered, two types of critical angular locations for the implementation of the large-scale wire on the cylinder surface were shown to exist based on the changes in the flow features in accord with the existing literature. At the first critical wire angle, the vortex shedding ceases for the majority of the time during which the vortex formation length extends, and there exists short time intervals where regular shedding resumes similar to the smooth cylinder. The second critical wire angle is found to encompass a range of angles (50° to 70°) where significant increase in spectral amplitude of Karman frequency is observed together with contraction of the near-wake. The angular location of the first critical wire angle decreases with the wire size, and increases with Reynolds number up to Re_D = 15,000, after which it remains unaffected by the Reynolds number.

Furthermore, the variations of the Strouhal number and the coherency of Karman vortex shedding are found to be, roughly, inversely related with each other. This investigation explains the relationship between different sets of critical wire angles previously defined by other researchers. Finally, a model is established for the estimation of the Strouhal number as a function of the wire angle. This model requires only the wire size (d), cylinder diameter (D), and Reynolds number (Re_D) as inputs, and, therefore, is applicable without any prior knowledge on the flow structures. It yields a low average error (<6.2%) when compared with the experimental data.

to the memory of my Father,

Acknowledgements

First, I would like to acknowledge my supervisor, Prof. Alis Ekmekci, for her supervision and support during my doctoral studies. Her detailed analysis during our discussions, and consistent research methodology helped me improve my professional skills. In addition, Prof. David Zingg, and Prof. Omer Gulder guided me in thinking about my research from many different perspectives, and their feedback was a great source of guidance and support.

As a strong believer of team-work, and community, I want to extend my gratitude to University of Toronto Institute for Aerospace Studies, and Faculty of Aeronautics and Astronautics (Istanbul Technical University) for investing so much on me in this dissertation.

During these years, I have to say that I've faced challenges in the ways that I didn't think about before I came to Toronto. Looking back to those days, I can see how my journey gave me a chance of growing as an international student in University of Toronto, and as a foreigner in Canada. I am grateful for the programs within the university accessible to the graduate students, and for the memories in Toronto and Montreal Tango communities, and with the warm people of New Brunswick. Without these people, I wouldn't be able to call Toronto as another home.

There have been a lot of people whom I would like to thank individually for their support. While it is not possible to name everyone here, I need to name a few of these special people without any particular order; Adam Blackmore, Antrix Joshi, Emre Karatas, Patricia Morrison, Candace Morrison, Olga Oulanova, Petra Dreiser, Dionysius Prakash Sarvesvaran, Deniz Turkben, Pierre Mathias (R.I.P.), Anisha Abdulla, and Ronald Hanson.

Finally, I have to mention the importance of family in my life, and especially its role during my doctoral studies. My family, especially my mother and brother, have taught me what unconditional support is all about in the adversity of long distances in between. And, most importantly, they have shown me that we are not only a family-by-blood, but also a family-by-choice. Thank you very much for your belief in me.

Contents

List of Tables

List of Figures

List of Symbols

b, a	: Major and minor axes of the ellipse
d	: Diameter of the wire
d^*	: Ratio of the wire size to the unperturbed boundary layer thickness
D	: Cylinder diameter
ΔD	: Tolerance in the cylinder diameter
E_{corr}	: Voltage corrected for the temperature change in water
E_a	: Acquired voltage
f_c	: Input frequency for the water channel inverter
Δf_c	: Resolution in the frequency control of the water channel inverter
f_{aq}	: Frequency of data acquisition
L	: Length of the cylinder span
L_{TE}	: Distance between the endplate trailing edge and the cylinder base
L_{LE}	: Distance between the endplate leading edge and the cylinder front
L_F	: Length of vortex formation
n_{vsc}	: Number of vortex shedding cycles sampled
n_{aq}	: Number of data points acquired
N	: Number of data points
p_∞	: Reference pressure
p	: Pressure measured at a given point
P	: Pitch of the helical wires
Re_{δ^*}	: Reynolds number based on the displacement thickness
Re_D	: Reynolds number based on the cylinder diameter
St	: Strouhal number
St_{max}, St_{min}	: Maximum and minimum Strouhal numbers attainable in the presence of the wire
St_ϕ	: Strouhal number in the oblique shedding mode
S_u	: Auto-spectral density of the streamwise velocity component
$S_u(f_K)$	: Spectral amplitude of the velocity fluctuations at Karman frequency
ε_{St}	: Uncertainty in the determination of Strouhal number
t_{aq}	: Data acquisition time
T	: Temperature
T_w	: Hot temperature of the hot-film probe
T_0	: Ambient reference temperature

T_a : Ambient temperature during acquisition

T_{vs} : Vortex shedding period

u : Streamwise component of the flow velocity vector

U_K : Discrete transformation of the streamwise velocity component

U_c : Convection velocity of the Karman vortices

U_0 : Free-stream velocity

ΔU_0 : resolution in the free-stream velocity adjustment

u_s : Settling velocity of the seeding particles

w : Vorticity

θ : Wire angle

$\Delta\theta$: Range of effective wire angles

θ_t, θ_c, θ_m, θ_r, θ_b : Critical angles defined by Nebres and Batill (1993)

θ_{c1}, θ_{c2} : Critical angles defined by Ekmekci and Rockwell (2010)

$\Delta\theta_{corr}$: Wire angle correction

δ : Boundary layer thickness

δ^* : Displacement thickness

v : Kinematic viscosity of water

μ : Dynamic viscosity of water

$\vec{\mu}$: Vector of the critical wire angles and Strouhal number boundaries

x : Cartesian coordinate in the streamwise direction

y : Cartesian coordinate in the cross-flow direction

z : Cartesian coordinate in the spanwise direction

ρ_p : Density of the seeding particles

ρ_w : Density of the water

λ : Endplate leading edge distance parameter

$c_p(\theta)$: Circumferential distribution of the pressure coefficient

ψ : Streamlines

$\Delta\varphi$: Phase angle difference

ϕ : Vortex filament angle

ϕ_{vf} : Most probable vortex filament angle

Chapter 1

Introduction

External flow around cylindrical or near-cylindrical bodies has been a field of extensive research due to its application in a variety of engineering components/systems for a number of decades but still poses challenging problems. These types of flows are complex even for a simple geometry due to the coexistence of the boundary layer, free shear-layers and a significant region of recirculatory flow. In classical aerodynamics, these types of bodies are called as blunt/*bluff bodies* (Anderson 2001)

A traditional example of the bluff body wake flows is encountered around cylinders with a circular cross-section. Past a certain value of Reynolds number, periodic vortex shedding from the cylinder leads to pressure imbalances and, as a result, unsteady force loadings on the structure. Forces acting in the streamwise direction, defined as *drag* force, fluctuate around a non-zero mean drag at a frequency twice the vortex shedding frequency. On the other hand, *lift force*, acting on the body along the lateral (cross-flow) direction, fluctuates around a zero-mean value at the vortex shedding frequency. This fluid-structure interaction might lead to vortex-induced vibrations, in majority observed along the lateral direction, and threatens the fatigue life and integrity of the structure. Therefore, effective control of the vortex shedding is crucial in the control and/or avoidance of these detrimental effects.

The study herein will explore how the flow past a stationary bluff body with a circular cross-section can be manipulated to effectively battle against the challenging consequences of the above-mentioned vortex-induced vibrations. The passive flow control through the use of a single tripwire implemented on the surface of a circular cylinder will be investigated.

This chapter will continue with a brief description of the flow characteristics in the circular cylinder wake, and methods of vortex-induced vibration control with a focus on the use of geometric surface protrusions. After the related literature is introduced, unresolved issues on the literature and the scope of this dissertation will be given.

1.1. Brief Description of the Wake of a Circular Cylinder

In presence of a uniform oncoming flow, the basic mechanism of vortex shedding from a circular cylinder is related to the cut of the vorticity supply from the shear-layer onto the same signed growing vortex by the opposite signed vortex growing on the other side of the cylinder. This process repeats itself twice in a single vortex shedding period and results in two shed vortices, each with an opposite sign of vorticity shed from either sides of the cylinder (Gerrard 1966, Perry *et al.* 1982).

Prior to continuing to a more detailed review on the characteristics of the wake, three key elements of the flow field will be defined. *Wake width* is one of the two major length scales within the near wake region and is defined as the lateral distance at a given streamwise location between two points situated at the opposite sides of the cylinder centerline distinguishing the outer flow from the rotational wake flow (Roshko 1954). *Vortex formation length*, as a second length scale, is defined as the streamwise distance between the cylinder base and the point where a vortex is shed (Gerrard 1966). One method of determining the vortex formation is to identify the location of the maximum root-mean-square (r.m.s.) fluctuation in the streamwise velocity component (Williamson 1996). As a second method, the velocity field can be averaged over a sufficiently large amount of time, and, then, one can define a similar length scale referred to as "*mean recirculation bubble*" (Roshko 1993). The mean recirculation region is bounded by a closed streamline pattern and is symmetric with respect to the cylinder centerline. The streamwise distance between the cylinder base and the saddle point where the streamlines intersect can also be interpreted as a time-averaged vortex formation length. Another important definition is related to the negative (suction) pressure at the cylinder base and is referred to as "*base pressure*". The suction pressure is the major source for the mean drag force acting on the bluff body due to the separation of the boundary layer, and is inversely proportional to the vortex formation length (Bearman 1965).

A comprehensive review of vortex dynamics in the cylinder wake is given by Williamson (1996). The characteristics of the flow past a circular cylinder strongly depend on the oncoming flow Reynolds number. In the following, a summary of the flow regimes as a function of Reynolds number based on the cylinder diameter (Re_D) is given.

For Reynolds numbers smaller than approximately 49, the wake is considered to be steady. The flow field is laminar with two counter-rotating eddies in the wake. For $49 \leq Re_D \leq 190$, the wake becomes unstable and the associated flow is referred to as *laminar vortex shedding regime* with a well-defined vortex street. The oscillations of the wake are purely periodic when the end conditions of the cylinder are manipulated carefully. At the end of this regime around $Re_D \approx 190$, three dimensional effects start to appear in the wake due to the transition in the shed vortices. Within this *wake-transition regime*, two distinct secondary instabilities are identified, namely Mode A, and Mode B. They start approximately at $Re_D \approx 190$ and 260 respectively. The exact value for the critical Reynolds numbers of mode A is subject to hysteresis effects. In these Mode A and B secondary instabilities, streamwise vortices form in the wake with a spanwise wavelength. While Mode A has a spanwise wavelength of three cylinder diameters, Mode B is observed to have a finer wavelength of one cylinder diameter. Both of these secondary instabilities lead to discontinuities in the variation of Strouhal number, which is the non-dimensional form of the vortex shedding frequency, when plotted as a function of the Reynolds number. As Reynolds number is further increased from 260 to 1,000, the three-dimensional structure of the fine scaled streamwise vortices becomes disordered. This leads to a reduction in Reynolds stress, base suction, and an increase in the vortex formation length. For a Reynolds number range of $1{,}000 \leq Re_D \leq 200{,}000$, the wake regime is referred to as *shear-layer transition regime*. As Reynolds number is increased in this regime, two-dimensional Reynolds stresses increase. On the other hand, the Strouhal number and the vortex formation length decrease. In addition, the transition to turbulence in the wake also takes place at upstream locations in the shear layers where Kelvin-Helmholtz instability (shear-layer instability) arises. Within the free-shear layers, small-scale vortices form, and they generate oscillations at frequencies that roughly scale with $Re_D^{3/2}$, leading to an increase in the base suction pressure. For Reynolds numbers larger than 200,000, onset of transition to turbulence occurs at further upstream locations in the separating shear layers and reaches the boundary layer separation points at either side of the cylinder. The transition in the boundary layer initially occurs on one side of the cylinder and leads to a separation/re-attachment bubble on one side of the cylinder while the boundary layer flow separates in a laminar state on the other side of the cylinder. This asymmetrical condition in the state of the boundary layer prior to separation leads to large mean lift forces as opposed to a zero mean lift force for a symmetric flow. Past this *critical flow regime* follows the *supercritical regime* characterized by symmetric separation/re-attachment bubbles due to the transition in the boundary layers at both sides of the cylinder. At

this regime, the transition (for each side of the cylinder) occurs somewhere between the front stagnation point and the separation point. As Reynolds number is increased further until to the orders of 10^6 - 10^7, the transition point reaches the front stagnation point, and the boundary layer around the cylinder becomes fully turbulent. This regime is called as the *boundary-layer transition* or *post-critical regime*.

1.2. Control Methods of Vortex-Induced Vibrations in Cylindrical Structures

Vortex-induced vibrations (VIVs) are excited by the vortices shed from the structure. Detailed characteristics of this type of excitation are given in the book by Naudascher and Rockwell (2005). As described therein, the Karman instability of vortex shedding grows in space and leads to self-sustained flow oscillations in the near wake due to the unsteady pressure distribution around the cylinder surface. Within the cross-sectional plane of the cylinder, the majority of the fluctuating pressure forces are normal to the free-stream direction with a frequency equal to the vortex shedding frequency but minor fluctuating forces also act along the flow direction at a frequency twice the Karman frequency. In engineering examples of bluff body flows, the structures are not necessarily constrained in their movement as opposed to the laboratory experimental condition of stationary cylinders. When a rigid cylindrical body is free to vibrate, the vortex induced force loadings might lead to the vibrations of the cylinder depending on the structural damping and the structural natural frequency. The most important excitation occurs at the resonance conditions along the cross-flow direction and the flow becomes coupled with the cylinder vibration known as the *lock-in* phenomenon.

Today's engineers undergo cautious design procedures against wind-induced loads for tall buildings, which are major concerns for public comfort and safety issues. In general, avoidance of the resonance conditions can be achieved through the modification of the stiffness of these buildings and the use of vibration dampers. However, this is an expensive solution. Some cost-effective, applications include the variance of the cross-section, i.e. *tiering strategy*, rounding of the sharp corners and/or opening bleeding slots through the building that serve as means of flow control (Irwin 2010). Another practical example is the flow around the yawed stranded cables used in suspension bridges and transmission lines. The prediction of the fatigue life for these structures relies on understanding the flow and is affected by number of strands and the yaw angle (Nebres

1992). Marine cables, and offshore platforms are also applications where the significant vortex-induced vibration needs to be controlled by streamlining the cables with fairings (Kumar 2008).

Basic ideas lying under the control of the self-sustained oscillations of the near wake flow are to intervene with the mutual interaction of the shear layers and/or to modify the boundary layer characteristics in order to modify or, if possible, mitigate the process of vortex shedding. However, the flow behind a nominally two-dimensional bluff body is inherently three-dimensional due to the transition to turbulence within the near wake starting at $Re_D \approx 190$ and the transition point moves upstream within the flow field with increasing Reynolds number. The three-dimensional nature of vortex shedding in a turbulent wake affects the spanwise correlation of the shed Karman vortices. For example, the correlation length scales along the cylinder axis within the range of $10^4 < Re_D < 10^5$ are shown to be 3 - 6 cylinder for stationary cylinders (King 1977). When the actual body span is much larger than these length scales, the net force acting on the whole body is significantly smaller than its estimated value by integration of cross-sectional forces along the span due to out-of-phase cross-sectional loading along the span excited by the Karman vortices. Therefore, another category of flow control focuses on the correlation of the flow structures along the spanwise axis of the structure in order to obtain a reduction in the amplitude of the net force. Overall, a good method should demonstrate, at least, the capability to reduce the fluctuating lateral (lift) force amplitude, avoid *lock-in* region and reduce the mean streamwise (drag) force for a generality of flow conditions. These control variables are directly related to the coherency of Karman instability within the bluff body wake and the vortex shedding frequency.

Methods developed so far can be grouped as open or closed loop control methods based on whether feedback information from the wake flow characteristics is included in the control loop or not. Closed loop methods, which, in general, do not include feedback information, are studied more than their open loop counterparts due to their simplicity and cost-effectiveness in applications (Hangan and Kim 2003). Another approach of classifying the control mechanisms is given in one of the reviews by Zdrackovich (1981). According to his review, there are three main classifications for these methods; *(i)* surface protrusions, *(ii)* shrouds, and *(iii)* near-wake stabilizers. *Surface protrusions* are methods that affect the separation point of the boundary layer and/or separated shear layers. *Shrouds* affect the entrainment layers and *near wake stabilizers* affect the mutual interaction of the two separating shear layers. Among these categories, there is an additional sub-classification regarding the techniques' sensitivity to the flow direction. While the effectiveness of

the *omnidirectional* methods is not affected by the flow direction, the *unidirectional* methods are highly dependent on the flow direction. The following chapters will focus on both omni- and uni-directional types of surface protrusions.

1.3. Surface Protrusions Applied to the Cylinders

Surface protrusions are passive techniques of flow control and take the form of perforated plates, axial rods and slats, tripwires, and strakes in their application to bluff bodies. In principle, the surface non-uniformities introduced as flow perturbations within the boundary layer forming around the cylinder aim to promote turbulent transition as discussed by (Kumar *et al.* 2008, Naudascher and Rockwell 2005, Zdravkovich 1981, 2003). Most of the research is conducted within the sub-critical (wake transition) regime where the boundary layer is completely laminar and the promotion to turbulence acts as a simulator of the critical flow conditions occurring for Reynolds numbers greater than 200,000. When the state of the boundary layer is turbulent, the increased kinetic energy of the fluid close to the cylinder surface leads to an increased resistance to the basic mechanism of flow separation from a cylinder, i.e. adverse pressure gradient along the cylinder circumference (Schlichting 1968). This results in a delayed separation compared to the laminar case and is analogous to the famous drag-crisis around $Re_D \approx 3\text{-}4x10^5$ as mentioned in the book by Anderson (2001). At this point, the literature review will focus on tripwires and continue with their omnidirectional and unidirectional applications with strakes, rods and wires in particular.

1.4. Omnidirectional Applications

Helical wires, strakes and stranded cables are examples of omnidirectional surface protrusions. They aim to modify the flow separation line along the cylinder axis and introduce three-dimensionality into the near wake of a nominally two-dimensional cylinder. The suppression of VIVs with the use of these devices is summarized in the review articles by Zdravkovich (1981) and Kumar (2008). In one of the earliest studies, Scruton and Walshe (1957) showed the aerodynamic instability region reduced significantly when three sharp edged strakes with a height-to-diameter ratio of $h/D = 0.118$ were helically wound around the cylinder using a pitch of $15D$. Adverse effects of the helical wires in the structural response for eight wires and a single wire wound around the cylinder were also shown (Nakagawa *et al.* 1959, 1963). With the contributions of other researchers in this field, optimum configurations have been revealed by varying the

protrusion size (Weaver 1961, Every *et al.* 1982), number of protrusions (Weaver 1961), and pitch (Woodgate and Mabey 1959, Hirsch et al 1975).

Although helical wires and strakes have been used widely in various engineering applications, they exhibit some disadvantages. First of all, they result in an increase in the mean drag force and the structural base moments (Cowdrey and Lawes 1959). Thus the method requires additional structural modifications in their application. Secondly, the efficiency of helical protrusions is significantly reduced in the turbulent approach flow (Ruscheweyh 1981). Thirdly, they become inefficient below a certain mass-damping parameter (Gartshore *et al.* 1979). All the investigations presented above have considerably advanced our understanding on several aspects pertinent to the control of flow past cylinders with surface non-uniformities applied in helical forms. However, the knowledge on how they affect the vibrations and change the flow characteristics is still lacking mostly due to the complexity of the highly complex three-dimensional flow fields (Chyu and Rockwell 2002, Zhou *et al.* 2011).

1.5. Unidirectional Applications

In search of a physical understanding of the flow in the presence of surface perturbations, a number of investigators have turned their attention to two-dimensional geometric disturbances in the form of a spanwise (straight) tripwire. Studying these simpler geometries is considered a step towards understanding the physics involved in more complicated configurations. In the application of single or two symmetrically situated straight wire(s) on stationary cylinders, the characteristics of the flow have been shown to depend on the wire angle, the wire size and the Reynolds number (Alam *et al.* 2010, Ekmekci 2006, Ekmekci and Rockwell 2010, 2011, Hover and Triantafyllou 1999, 2000, James and Truong 1972, Nebres 1992, Nebres and Batill 1993).

Effect of the wire angle: The wire angle θ is defined as the circumferential angle between the wire location and the front stagnation point of the cylinder, where $\theta = 0°$. In the presence of a single spanwise wire, the vortex shedding frequency, i.e. Strouhal number (St), varies from its reference value within a certain range of wire angles; it initially decreases, and increases back to its reference value as the wire angle is increased. At the beginning and end of this crater-like distribution, the value of Strouhal number may exceed its value observed for a smooth cylinder depending on Reynolds number and wire size (Nebres 1992, Nebres and Batill 1993).

In addition to the changes in the vortex shedding frequency, the flow topology on the wire side of the cylinder has also been shown to undergo significant alterations as the wire is implemented on the cylinder surface at different angular locations. Depending on the wire angle, four flow regimes are identified based on the transition and separation characteristics of the boundary layer at subcritical Reynolds numbers (Fujita *et al.* 1985, Igarashi 1986, Nebres 1992, and Nebres and Batill 1993). The following is a brief summary of these flow regimes encountered in the order of increasing wire angle. In the first regime, the boundary layer separates at the wire location and re-attaches to the cylinder surface without turbulent transition. Downstream of the re-attachment point, laminar separation occurs from the cylinder. As the wire angle is increased, boundary layer separation at the wire location and re-attachment to the cylinder downstream of the wire are still observed. In contrast to the first regime, however, the re-attached boundary layer undergoes turbulent transition. This leads to a delayed final separation from the cylinder surface compared to the first regime described above. With further increase in the wire angle, as a third regime, the flow separates at the wire and does not re-attach to the cylinder surface. Finally, in the fourth flow regime, being in the base region of the cylinder, the wire has an insignificant effect on the overall flow structure. In all these flow regimes, Nebres and Batill (1993) showed that the tripwire effectively leads to a pressure drop across its cross-section and the value of this pressure drop is closely related to the variations in the aforementioned flow regimes.

The changes in the characteristics of the boundary layer around the cylinder fitted with a single, spanwise wire are directly correlated with the changes in the vortex shedding frequency. Based on the aforementioned typical variation of Strouhal number, Nebres and Batill determined five critical wire locations on the cylinder surface defined as θ_t, θ_c, θ_m, θ_r, θ_b in the order of increasing angular location θ (Nebres 1992, Nebres and Batill 1993). θ_t defines the boundary between the first two regimes mentioned previously; *(i)* final laminar separation downstream of the wire for $\theta < \theta_t$, and *(ii)* final turbulent separation downstream of the wire for $\theta_t \leq \theta \leq \theta_c$. Within the wire angle range of $\theta_t \leq \theta \leq \theta_c$, Strouhal number may increase depending on the wire size and Reynolds number, and, for the cases where an increase in *St* is observed, it reaches its maximum value at $\theta = \theta_c$. At this point, an increment in the wire angle as small as 1° yields a dramatic decrease in Strouhal number values. The angular location of the wire at $\theta = \theta_m$ corresponds to the global minimum point of Strouhal number distribution. The fourth critical wire angle, θ_r, marks the end of the flow regime where the flow separates at the wire. Finally, the fifth critical angle, θ_b, defines the angular location

after which a further increase in θ does not lead to any significant changes in the values of Strouhal number.

Recent work by Ekmekci (2006) and Ekmekci and Rockwell (2010, 2011) revealed two locations that are critical for the implementation of a single, spanwise wire on the basis of the near-wake characteristics. These critical locations on the cylinder surface were designated as θ_{c1} and θ_{c2}. By utilizing Particle Image Velocimetry (PIV), they showed that a surface wire (d/D = 0.029) at θ_{c1} location leads to significant amount of extension in the streamwise length of the time-averaged near-wake bubble, while a wire at θ_{c2} yields contraction for Re_D = 10,000. As a further distinguishing characteristic of the critical locations, Ekmekci and Rockwell (2010) also revealed that the spectral amplitude of velocity fluctuations at Karman frequency significantly mitigates when the wire (which is larger than the unperturbed boundary-layer thickness) is positioned at θ_{c1} and amplifies when the same wire is at θ_{c2}. This implies that the coherence and strength of Karman vortex shedding can be altered drastically by employing a large-scale spanwise surface wire at critical locations. Soon after, Ekmekci and Rockwell (2011) extended this study onto smaller scale wires (d/D = 0.005 and 0.012) for Re_D = 10,000. However, a wire smaller than the unperturbed boundary layer thickness was found to have no significant effect on the coherence and strength of the Karman instability at critical locations.

In addition to the flow regimes mentioned above, the works of Ekmekci (2006) and Ekmekci and Rockwell (2010, 2011) revealed a new regime for cylinders fitted with a single spanwise wire. In this regime, the shear layer separating at the wire goes intermittently between the states of reattachment and no-reattachment at a broadband low frequency. This bistable regime occurs just when the wire is at the critical location θ_{c1}, which is found to be at the border of the previously-defined regimes (the continual state of reattachment and no-reattachment of the shear layer), and leads to a flow rate imbalance downstream of the wire due to the intermittency of the flow state. This imbalance in the flow rate significantly disrupts the formation of the vortex on the wire side, and leads to the attenuation of Karman vortex shedding. Another recent, independent study conducted by Alam *et al.* (2010) showed that the same bistable phenomenon appears also for the case of a cylinder fitted with a pair of spanwise wires (placed symmetrically with respect to the forward stagnation point of the cylinder).

In addition to the variations in the vortex shedding frequency, and its correlation with the changes in the characteristics of the boundary layer, other flow features are also affected as the location of

the tripwire is systematically varied. If one defines the shear layer spacing as the lateral distance between two points located at either side of the cylinder where the velocity reaches to its maximum, then, its variation follows an approximately inverse relationship with the variation of Strouhal number as shown by Nebres (1992) and Ekmekci (2006). Interestingly, the critical wire locations based on the distribution of the shear layer spacing are observed to stay the same as the critical angles defined based on the variation of Strouhal number, i.e. θ_t, θ_c, θ_m, θ_r, θ_b (Nebres 1992, Nebres and Batill 1993). On the other hand, the vortex formation length follows a roughly similar trend with Strouhal number with the exception of the angular location of $\theta = \theta_{c1}$; the streamwise extent of the mean recirculation region reaches to its maximum at $\theta = \theta_{c1}$, but Strouhal number reaches to its maximum at $\theta = \theta_c$ which comes slightly earlier than θ_{c1} (Ekmekci 2006, Ekmekci and Rockwell 2010, 2011). Also, the base pressure and the mean drag coefficients show roughly and inverse relationship with the vortex shedding frequency while fluctuating lift force coefficient varies similar to Strouhal number according to the findings of Nebres and Batill (1993).

Effect of the wire size and Reynolds number: The earliest investigation on the effect of the wires was performed on cylinders fitted with two longitudinal tripwires placed at ±65° from the front stagnation point Fage and Warsap (1929) in the sub-critical regime. They showed that the tripwires with a cross-sectional diameter within the range from 0.03δ to 1.61δ, where δ represents the estimated boundary layer thickness, can lead to a reduction in the drag force and alterations in the pressure distribution around the cylinder. These effects were enhanced at higher Reynolds numbers and an increase in the wire diameter was shown to lead to transitional characteristics of a higher Reynolds number flow at lower Reynolds numbers. While their study did not consider the effect of the wire angle, they argued that the wire-induced disturbances are most significant when the wires are located prior to the flow separation in absence of the wires.

James and Truong (1972) demonstrated the existence of a strong dependence of the drag force on the wire size and the wire angular position for a single straight wire. Wire angle was considered as a stronger parameter compared to the wire size. Overall, the changes in drag were reported to be within ±40% of its nominal value. They also determined, from a hot-wire probe behind the perturbation, that the turbulence level increases for the case corresponding to the minimum drag coefficient, which occurred in their case around a wire angular location of 55°.

The effects of two thin, longitudinal wires, wire-to-cylinder diameter ratios of $d/D = 0.003$, on stationary and oscillating cylinders have been investigated by Hover *et al.* (2001) at a wire angle

of ±70° for a sub-critical Reynolds numbers range up to $Re_D = 4.6x10^4$. Significant reductions in of drag and lift coefficients together with an increase in Strouhal number as a function of Reynolds number have been reported.

The range of effective wire angles ($\Delta\theta = \theta_b - \theta_t$), the range of wire angles where a turbulent, delayed separation occurs ($\theta_c - \theta_t$), and the maximum attainable Strouhal number (St_{max}) increase with increasing Reynolds number or the wire size as shown by several researchers (Alam *et al.* 2010, Nebres 1993, Ekmekci and Rockwell 2011). On the other hand, the minimum Strouhal number (St_{min}) is observed to be relatively constant around 0.17. The angular location of the critical angles θ_t, θ_c, θ_r, θ_b also strongly depend on a given set of wire size-to-cylinder diameter ratio (d/D), and Reynolds number (Re_D). However, the critical angle where St reaches its global minimum value, $\theta = \theta_m$, stays constant around $\theta = 69°$ (Nebres 1992, Nebres and Batill 1993). While increase in Reynolds number leads to larger values for θ_b and smaller values for θ_t, larger wires result in smaller angular locations for the critical angles; θ_t, θ_c, θ_{c1} and θ_{c2} (Alam *et al.* 2010, Nebres 1993, Ekmekci and Rockwell 2011).

1.6. Unresolved Issues

The main motivation of the present research on straight tripwire(s)/rod(s) is to obtain further understanding of the flow features as a response to the perturbation and guide the applications of more complex protrusion devices for vortex-induced vibration control. While the previous studies mentioned above provide valuable insight on the flow field and the resultant forces acting on the cylinder in presence of tripwires, the following points need to be further investigated.

(i) The research methodology employed by Nebres and Batill is based on the pointwise measurements of the vortex shedding frequency and the classification of flow regimes are based on the St-θ curves. While this investigation has an advantage in the accuracy of the spectral analysis and involves some qualitative understanding into the flow topology via smoke visualization, it lacks quantitative information about the flow structures within the near-wake and the shear-layer regions perturbed by the wire. The second methodology used by Ekmekci and Rockwell focuses on the attenuation/amplification of Karman shedding, and the modified flow structures in the near-wake and shear layer regions by sampling of the velocity field using Particle Image Velocimetry (PIV) but has a disadvantage in the precision of spectral analysis for St-θ curves due to a limited sampling capability of their PIV system compared to the hot-wire measurements. Due to the

differences in their parameter space, experimental techniques and the principles for the classification of the flow regimes, the relationship between the critical angles defined by Nebres and Batill (θ_t, θ_c, θ_m, θ_r, θ_b), and those defined by Ekmekci and Rockwell (θ_{c1}, θ_{c2}) is still unknown.

(ii) In the presence of a large-scale tripwire, i.e. a wire larger than the unperturbed boundary layer thickness, the attenuation/amplification of the Karman vortex shedding has not been studied for varying Reynolds numbers and wire sizes.

(iii) The data presented by Nebres and Batill are based on hot-wire signals sampled away from the cylinder, and do not show any evidence of bi-stable oscillations. According to Ekmekci's study, the influence of the bistable oscillations is constrained to the upstream regions of the shear-layer separating from the wire side of the cylinder, which is upstream of Nebres and Batill's measurement point. This makes the identification of the bistable oscillations almost impossible in the experiments of Nebres and Batill. Therefore, the information available in the literature does not clarify if the bistable oscillations for a large-scale wire when the wire angle is at the critical angle $\theta = \theta_{c1}$ still exist or not at higher Reynolds numbers and/or larger wire sizes.

(iv) Nebres and Batill focused on different universal Strouhal numbers proposed by Fage and Johanssen (1927), Roshko (1955), Bearman (1967), and Griffin (1981) as summarized in the book by Zdravkovich (2003) in order to establish an estimation model for the St-θ curves. In his study, he was able to obtain an average error level of 2.5% for a reference Strouhal value of $St = 0.2$ based on a single set of his experimental data (Re_D = 30,000 and d/D = 0.09) using a modified wake similarity parameter. Although his results are promising, this approach requires prior knowledge of the wake-flow length scales, e.g. time-averaged spacing between the shear layers, and the base pressure parameter. In addition, these estimation techniques have been tested for a single set of experimental data and lacks generality. Therefore, a generally applicable model for the prediction of vortex shedding frequencies is still not established.

1.7. Scope of the Current Study

The main goals of this dissertation are to address the unresolved issues highlighted in the previous section. The objectives can be summarized as *i)* the identification of whether the critical wire angles (θ_{c1}, θ_{c2}) and bistable flow exist for various large-scale wires for different Reynolds numbers, *ii)* if these critical flow conditions exist, the effects of the wire size and Reynolds number on these critical angular locations, *iii)* the relationship between the different sets of critical wire

angles defined by Nebres and Batill (1993) and by Ekmekci and Rockwell (2010), and *iv)* establishment of a model for the estimation of *St* variation as a function of the wire angle for a given wire size and Reynolds number. In order to successfully achieve these goals, the experimental setup is of crucial importance since the cylinder wake flow is sensitive to the experimental conditions. Therefore, the determination of the optimum experimental setup conditions is an additional, but a secondary goal of the study.

Particular focus is placed on the flow past a circular cylinder fitted with a single, large-scale tripwire for different wire sizes (d/D = 0.029, 0.039, 0.059) and Reynolds numbers ($5{,}000 \leq Re_D \leq 30{,}000$). The research methodology employs pointwise hot-film measurements for accurate spectral analyses, planar Particle Image Velocimetry for the quantitative visualization of the flow structures, and hydrogen bubble flow visualization for the qualitative long-time sampling of the flow streaklines.

This dissertation consists of six chapters. In the present chapter, the literature review on the flow dynamics for the circular cylinder wakes, and the effects of the surface protrusions on the flow are given together with the unresolved issues and the scope of the study. In Chapter 2, the details of the experimental methodologies and data analyses techniques are provided. In order to support the interpretations of the experimental results for cylinders fitted with a spanwise tripwire, considerable effort is given to the understanding of the quantitative features of the flow field in absence of the tripwire. Chapter 3 presents a detailed review on the literature related to the junction flows and wake quasi two-dimensionality, followed by the characterization of the wake features under different experimental conditions in absence of a wire with the aim of identifying the appropriate experimental configuration. Chapter 4 focuses on the effects of a single, large-scale tripwire and demonstrates the flow response to the surface protrusion for the above-mentioned parameters. Chapter 5 presents a model established for the estimation of the vortex shedding frequency as a function of the wire angle at a given Reynolds number and wire size. This model is constructed based on the experimental data presented in Chapter 4. Finally, Chapter 6 summarizes the major conclusions of this dissertation with a discussion on how the results can be applied, and the recommendations for future research on the topic.

Chapter 2

Experimental Methodologies and Data Analysis Techniques

This chapter provides an overview of the experimental facility, test, methodologies and data analysis techniques used for the exploration of the effects introduced by a single tripwire onto the overall near-wake flow topology as well as the determination of the flow characteristics around the circular cylinder in the absence of the wire. Details of the experimental facility, given in section 2.1, will be followed by the descriptions of the experimental configurations and methods used in sections 2.2, and 2.3 respectively. Finally, the data analysis techniques will be given in section 2.4.

2.1. Flow Facility

Throughout this study, experiments were conducted in a recirculating water channel located in Experimental Fluids Research Laboratory at the Institute for Aerospace Studies, University of Toronto.

The water channel is manufactured by Engineering Laboratory Design (ELD) Inc. The channel has a capacity of approximately 10,675 litres of water and its overall dimensions are 11.59 m (length), 2.12 m (width), and 3.00 m (height). The flow generated within the test section is continuous through the closed loop driven by the pump/motor assembly. The pump is a single stage, axial flow, 3-propeller type and is connected to a 20 HP motor via a pump/motor sheave belt. Upstream of the test section and prior to the contraction chamber, the water flow goes through the flow conditioning components consisting of 1 stainless steel perforated plate, 1 honeycomb with a stainless steel screen and 3 additional high porosity screens. Following these components, the flow speed is increased along a contraction section with a 6:1 area ratio. This contraction is symmetrical with respect to the channel centerline. For all the Reynolds numbers considered in this study, the streamwise turbulence intensity was lower than 0.5%, and the flow uniformity was better than 0.3%. The test sections are made of acrylic glass to enable visual access with a wetted cross-section of 0.610 m (width) and 0.685 m (height). At the downstream end of the test sections, the return plenum guides the water flow to the settling chamber through a pipe within the closed flow loop circuit. More details on the components of the system can be found in the manual

provided by ELD Inc. (2009). All components of the channel except the test sections are covered on the top. This enables the facility to be used as a free-surface experimental facility if necessary. However, throughout this study, the test sections are covered with additional plates of acrylic glass fitted to the top of the channel, making the facility a water tunnel. This modification is used to avoid the formation of free-surface waves at the free-stream velocities necessary for high Reynolds numbers.

The motor running the main propeller was controlled by a frequency inverter with an input range of 0 to 60 Hz at a resolution of 0.1 Hz. The relationship between the frequency (f_c), at which the motor is run, and the free-stream velocity (U_0) was established, based on the measurements with Particle Image Velocimetry, with a linear curve-fit given in Eqn. (2.1),

$$U_0 = 6.2 + 12.54 f_c \qquad (2.1)$$

where U_0 and f_c are in terms of mm/s and Hz respectively. As the frequency inverter control resolution is $\Delta f_c = 0.1$ Hz, the uncertainty in the free-stream adjustment is $\Delta U_0 = 1.25$ mm/s. The temperature of the water was not controlled and, thus, depended on the ambient temperature in the laboratory. In order to keep the changes in Reynolds number minimum (due to the temperature fluctuations), free-stream velocities were adjusted after the fluid temperature was measured using a thermocouple based sensor with a measurement accuracy of ±0.1 °C, and the kinematic viscosity was determined. The values of fluid temperature (T), kinematic viscosity (ν), the cylinder diameter (D), the corresponding free-stream velocities (U_0) and the inverter frequencies (f_c) are given in Table 2.1 for each Reynolds number used in the experiments. Uncertainty values for the temperature measurements and the tolerance in the cylinder diameter are also given.

Table 2.1 Free-stream velocities and inverter frequencies as a function of the Reynolds number.

Re_D	T, [°C]	ν, [m²/s]	D, [mm]	U_0, [mm/s]	f_c, [Hz]
5,000	26.0±0.1	8.822e-7	50.8±0.35	86.8±1.25	6.4
10,000				173.6±1.25	13.4
15,000				260.5±1.25	21.8
20,000				466.15±1.25	36.7
30,000				520.98±1.25	41.0

2.2. Experimental Configurations

All cylindrical models used in the experiments had a circular cross-section and were made of solid acrylic glass rods with a diameter of $D = 50.8$ mm. The models were mounted vertically within the

water tunnel, equidistant from the channel side walls. Figure 2.1 shows the experimental setup using an endplate on each end of the cylinder and the close-up view of the cylinder/rotary stage arrangement. For more details on the dimensions of the setup and the models, Figure 2.2 depicts schematics of the experimental setup and the cross-sectional view of the cylinder/wire models. The wire angle, denoted as θ, is measured from the time-averaged front stagnation point of the cylinder to the wire location along the cylinder circumference. All the wires were made of circular nylon fishing line. They were stretched straight along the cylinder axis and glued to the cylinder surface ensuring that there is no gap between the wire and the outer surface of the cylinder. The diameter of the tested wires were 1.5, 2.0, and 3.0 mm, yielding a wire-to-cylinder-diameter ratio of d/D = 0.029, 0.039, 0.059. Reynolds numbers ranged from 5,000 to 30,000 based on the cylinder diameter as given in Table 2.1. During the experiments involving the tripwire, the wire angle was varied from $\theta = 0°$ to $\theta = 180°$ by rotating the cylinder-wire arrangement around the longitudinal axis of the main cylinder. The rotation was achieved by using a B4872TS type rotary stage, attached to the main cylinder above the tunnel ceiling, controlled by a computer with a positioning accuracy of 0.0125°/step. The angular error in the alignment of the wire with the front stagnation point of the cylinder was quantified to be $\Delta\theta_{corr} = 1°$ to 2° by employing the symmetry property of St-θ curves. This error in the wire angle is corrected in the results given in Chapter 4.

Two different experimental configurations, shown in Figure 2.2, were tested for all Reynolds numbers in order to quantify the effects of the symmetry in the experimental end-conditions on the degree of quasi two-dimensionality within the near-wake in conjunction with, and addition to the studies reported in Khoury (2012). The end configurations were twofold. One configuration had symmetrical boundary on both ends of the cylinder, while the other had asymmetric end boundary. The symmetrical end configuration, shown in Figure 2.2(a), involves an end-plate on both ends of the cylinder yielding a smaller cylinder aspect ratio of L/D = 10.5. For the asymmetrical end configuration, shown in Figure 2.2(b), the cylinder is bounded by the water tunnel ceiling at the top and an end-plate at the bottom yielding a higher aspect ratio of L/D = 12.1. The endplates had a rectangular area with dimensions of 12D (cross-stream) and 7.5D (streamwise), where D represents the cylinder diameter. The end plates were made of acrylic glass. The distance between the cylinder axis and the leading edge of the endplates was kept at 3D, following the recommendations of Stansby (1974), Szepessy and Bearman (1992), Szepessy (1993), and Khoury (2012). The blockage ratio based on the cylinder diameter is 8.3%.

In addition, two different geometries of endplate leading edge were investigated for the determination of the junction flow characteristics for Re_D = 10,000. While one leading edge geometry was sharp with bevel angle of 23.6°, as shown in Figure 2.2, the other leading edge geometry was selected to be a super-ellipse with an axis ratio of 8. The distance between the endplate leading edge and the cylinder front was 2.5D. The results of these investigations are presented in Chapter 3 and are the continuation of the thesis work by Blackmore (2011).

2.3. Experimental Methods

This section presents the experimental methods and instruments used throughout this study. The use of three different techniques, as mentioned in section 1.5, reveals different features of flow and are supplementary to each other. Initially, the details of the Constant Temperature Anemometry (CTA) technique and relevant data acquisition instruments will be given. This will be followed by the details of the Hydrogen Bubble Flow Visualization, Particle Image Velocimetry (PIV) methods, and surface pressure measurements.

2.3.1. Constant Temperature Anenometry (CTA)

The constant temperature anemometer is a transducer that senses the variations in the heat transfer from a small, electrically heated sensor exposed to the motion of fluid. The hot-film anemometers are widely used due to their high spatial resolution in the measurements, little interference with the flow, a high-frequency response, a high sensitivity at low velocities, low cost, and an output signal in the form of voltage for convenient data analysis (Lekakis 1996).

In spite of the advantages of the hot-film sensors over the hot-wire sensors, the use of hot-film probes in liquids is complicated by factors like probe fouling, bubble formation on film elements and the sensitivity of the calibration in relation to the small changes in the liquid temperature due to a low overheat ratio.

The formation of bubbles on a heated surface immersed in air saturated water was demonstrated by Rasmussen (1967). It was observed that the bubble problem mainly occurred if the bubbles of a certain size were already suspended in the water flow. To minimize this problem in the experiments, the water was allowed to stand before use. The problem of bubble formation was also minimized by restricting the temperature difference between the hot-film and water to about 20°C (overheat ratio = 1.08) following the suggestions of the review article by Bruun (1996). Reported

optimum overheat ratios used in other hot-film measurements are, 1.05-1.1 (Bruun 1996), 1.05-1.08 (Samways *et al.* 1994), 1.03-1.04 (Zabat *et al.* 1992), and 1.02-1.10 (Warschauer *et al.* 1974).

Another important factor in CTA data acquisition is the calibration drift due to the temperature effects. In addition, probe-surface contamination is considerable for hot-film probes in liquids, much more than that of the hot-wire probes in gases. The net effect of these factors is a rapid degradation in the calibration characteristic of the hot-film probe as discussed by Samways *et al.* (1994) and Zabat *et al.* (1992). Bruun showed that the temperature drift of 1 °C can result in a drop in the converted velocity values up to 17% for hot-film probes used in water flows (Bruun 1996). The uncertainty in CTA measurements are quantified to be lower than $0.056U_0$ when compared with the calibration data acquired by Particle Image Velocimetry, which was also used in Eqn. 2.1. In order to avoid calibration drift due to the temperature effects, water temperature was monitored using a thermocouple based sensor with a measurement accuracy of ±0.1 °C, and temperature correction was applied to the data where necessary using Eqn. (2.2)

$$E_{corr} = \left(\frac{T_w - T_0}{T_w - T_a} \right)^{0.5} \cdot E_a \qquad (2.2)$$

according to the recommendations in Jorgensen (2002). In this equation, E_{corr}, E_a, T_w, T_0, T_a denote the corrected voltage prior to the data conversion, acquired voltage, sensor hot temperature, ambient reference temperature, and ambient temperature during data acquisition, respectively.

A typical CTA system consists of a probe, a probe support, an anemometer, and a data acquisition computer. A representative schematic of the experimental setup is shown in Figure 2.3 with a single CTA probe in place together with the data acquisition system. In the experiments, heavy coated hot-film probes (type 55R11) were used with an overheat ratio of 1.08 to measure the time traces of the streamwise velocity component. The probes had a sensor resistance of 7.23 Ω, sensor lead resistance of 0.5 Ω, and a sensor temperature coefficient of resistance (TCR) value of 0.38 %/°C. The probe supports (type 55H22) were right angled and had a resistance of 0.42 Ω. For each probe, a single-channel mini-CTA anenometer was used. Data acquisition system consisted of an NI BNC 2110 terminal, and an NI PCI 6251 data acquisition card.

There are two types of experiments in which CTA hot-film probes were used. The details of the data acquisition parameters for both types of experiments are given in Table 2.2. One type of experiments was conducted in absence of the tripwires in order to quantify the phase difference of

vortex shedding between two points positioned 3*D* apart from each other around the cylinder mid-span (z/*D* = ±1.5*D* based on the coordinate system depicted in Figure 2.3). These experiments are denoted as "Q2D" experiments in Table 2.2, where Q2D refers to quasi two-dimensionality. Another type of experiments, denoted as "*St-θ*" experiments in the table, are aimed to evaluate the variation of vortex shedding frequency as a function of the wire angle. Both types of the experiments were performed at Re_D = 5,000, 10,000, 15,000, 25,000, 30,000 for both the symmetrical and asymmetrical end conditions as discussed in the section 2.2, and schematically shown in Figure 2.2. In Table 2.2, the positions of the probes are also given with respect to the geometrical center of the cylinder at its mid span. The *x*, *y*, and *z* coordinates correspond to the distances between (the reference point) point O in Figure 2.3 and the CTA probe along streamwise, lateral (cross-flow), and spanwise axes, respectively. The use of an endplate at the top end of the cylinder, for the symmetrical end conditions, required the CTA probe to be positioned at 4.3*D* away from the cylinder axis along the streamwise direction due to the length of the trailing edge of the endplate, (L_{TE} = 4*D*). However, for the asymmetrical case, the probe was positioned 3*D* away from the cylinder axis along the streamwise direction.

In Table 2.2, f_{aq}, n_{aq}, T_{aq}, and n_{vsc} represent the data acquisition frequency, number of samples, sampling time, and approximate number of vortex shedding cycles samples (for *St* = 0.2) respectively. Four ensembles of 2,048 discrete readings were collected for ensemble averaged spectral analysis regarding the *St-θ* experiments. The number of vortex shedding cycles sampled during one ensemble (for *St-θ* experiments) varied between 15-60 depending on Reynolds number due to a constant sampling time (41 s), and a varying vortex shedding frequency. For the experiments related to the wake quasi two-dimensionality (Q2D), the sampling frequency was varied with a constant number of samples in order to ensure approximately 1,200 vortex shedding cycles were sampled. For these experiments, the sampling frequencies were f_{aq} = 22, 44, 65, 110, 131 Hz from Re_D = 5,000 to Re_D = 30,000, which correspond to sampling times of T_{aq} = 3,636, 1,818, 1230, 727, 610 s respectively.

Table 2.2 Details of CTA data acquisition parameters, (*) exact values for these parameters are given within the text

Experiment	***x/D***	***y/D***	***z/D***	f_{aq}**, [Hz]**	n_{aq}	t_{aq}**, [s]**	n_{vsc}
St-θ	Varies (*)	3	0	50	2,048	41	15-60
Q2D	Varies (*)	2.5, 3	1.5, -1.5	Varies (*)	80,000	Varies (*)	1,200

2.3.2. Hydrogen Bubble Flow Visualization

Hydrogen bubble flow visualization technique is one of the qualitative flow analysis tools for water flows as reviewed by Clayton and Massey (1967). This technique relies on the visualization of the flow structures by hydrogen gas bubbles produced by the electrolysis of water. These bubbles of hydrogen can be generated along a wire acting as an anode in the form of a sheet or a filament and are introduced as tracer particles to the flow. In unsteady flows, the flow visualization experiments with this technique reveal streaklines and caution is necessary in their interpretations for the flow structures according to Hama (1962).

The major challenging factors with this technique for a good quality in the flow visualization results are buoyancy effect, the required rate of hydrogen bubbles generation for high-speed water flows, wire aging, and the half-life of the hydrogen bubbles in water. The diameter of the hydrogen bubbles are less than the wire diameter in general and have a negligible buoyancy effect when the flow velocities are large (Okamoto *et al.* 1971). During the experiments, the sheet of bubbles generated was observed to be horizontal with respect to the channel floor at the upstream side of the experimental model. This implies the effect of buoyancy is negligible on the motion of these tracer particles. The voltage applied to water for electrolysis dictates the amount of bubbles generated at the wire per unit time. While Asanuma and Takeda (1965) used 2,000 Volts to acquire good quality flow visualization images for high-speed flows at 7m/s, applied direct current voltage should be less than 100 Volts in order to avoid damage to the facility according to Schraub *et al.* (1965). Following the suggestions given in Schraub *et al.* (1965) for the bubble generation rate, approximately 2 kg of $NaSO_4$ (0.19 g/litre) was added to the water as an additive in order to increase the ionization of the water. The cathode (copper plate) / anode (platinum wire) distance was also kept minimum. This arrangement required an applied voltage of approximately 50 Volts for sufficient bubble generation. Wire aging is related to the non-uniform bubble generation along the anode wire and can be resolved with temporary reversal of electrical current polarities. The hydrogen bubbles are soluble in water and the half-life of the bubbles limit the spatial extent of the flow region being visualized. To keep the area of flow visualized during the experiments maximum, the wire is kept as close to the experimental model as possible.

Flow visualization experiments were conducted for the qualitative assessment of two types of flows; *(i) the cylinder/wire arrangement wake* for Re_D = 10,000 and d/D = 0.029, 0.039, 0.059 and *(ii) the cylinder/endplate junction* (with the sharp leading edge) for Re_D = 3,205 and 7,630. A

representative schematic view of the experimental setup is given in Figure 2.4 for the cylinder/wire arrangement. The anode served as a wire holder (together with the platinum wire); its prongs were 450 mm apart (for the cylinder/wire arrangement) and 400mm apart (for the cylinder/endplate junction study) and were electrically isolated to avoid hydrogen bubble production on the prongs. In both cases, the prongs were centered on the cylinder axis, holding a platinum wire with a diameter of 50 μm to generate a sheet of hydrogen bubbles. The wire was stretched tight horizontally along the cross-flow (lateral) direction. For all of the experiments, the wake of the platinum wire was observed to lack vortex shedding (because $Re < 49$, based on the platinum wire diameter). The sheet of hydrogen bubbles was generated at the mid-span of the cylinder for the cylinder/wire arrangement shown in Figure 2.2(a), and ~1 mm above the endplate for the cylinder/endplate junction study, which corresponds to a submerged wire holder depth of 358 mm and 627 mm for each case, respectively. Maximum operational Reynolds numbers for the experiments was Re_D = 10,000 in hydrogen bubble flow visualization experiments for the cylinder/wire arrangement due to the limited generation of hydrogen bubbles per unit time and Re_D = 7,630 for the cylinder/endplate junction due to the vortex-induced vibrations of the prongs. The platinum wire was placed approximately 95 mm upstream of the cylinder axis for the cylinder/wire arrangements and 40 mm upstream of the endplate leading edge for cylinder/endplate junction configuration. A variable voltage DC power supply (Kaito HY5005E2 0-5 A) was used to apply a potential difference between the copper plate (cathode) and the platinum wire (anode). A light sheet was formed by using an array of flashlights behind a carton board having an opening of 300 mm by 10 mm. The light sheet was applied horizontally from one side of the channel; passing through the transparent side wall and illuminating the bubble sheet. The visualized flow patterns were recorded using a camcorder (Cannon, VIXIA HFM300) at a framing rate of 30 frames per second (fps). The recorded videos were then converted to pictures with a commercial software (Aoao Video to Picture Converter).

2.3.3. Particle Image Velocimetry (PIV)

Planar Particle Image Velocimetry (PIV) is a non-intrusive, optical flow diagnosis technique for the instantaneous measurement of two velocity components within a planar domain of interest. This technique relies on the statistical determination of the displacement of naturally buoyant tracer particles in the flow. Various aspects related to the theoretical background of this technique are given in a recent book by Raffel *et al.* (2007). More details on its historical development and

reviews on the technique are given by Adrian (1991, 2005), Willert and Gharib (1991), and Willert (1996). Typical state-of-the-art PIV systems include a dual cavity laser, CCD camera, a synchronizer, data acquisition computer and can yield velocity fields with dynamic ranges in the order of 10^2 according to Raffel *et al.* (2007) based on the developments on the cross-correlation algorithms such as discrete window offset proposed by Westerweel *et al.* (1997). This quantitative flow visualization technique can also act as a supplementary tool in the validation of the computational fluid dynamics (Gharib 1996).

In order to determine the velocity field in the plane of interest, the flow is seeded with naturally buoyant tracer particles and a pair of images, each synchronized with the laser pulses, is captured with a known time interval in between the images. The synchronization of the laser pulses and the camera image capturing is maintained such that the first frame of the image pair, *Frame A*, is exposed to the laser light reflected by the particles for a very short amount of exposure time. This effectively captures the snapshot of the particle locations at that particular time. After the digital information on the CCD array is transferred onto the data acquisition medium, the second frame, *Frame B*, is recorded within the second pulse of the laser after a certain amount of time. This type of data acquisition is referred to as *double frame-single exposure* and the synchronization method is known as *frame straddling* (Raffel *et al.* 2007). While this method is limited in the maximum measurable velocity, especially for supersonic flows, due to the timing limitations between the laser pulses, it lacks the directional ambiguity in the velocity vector and provides an advantage over its previous version of *double exposed-single frame recording*. Once the image pair, defined as a *PIV recording*, is transferred to the computer, cross-correlation of these images within small interrogation windows is performed for the statistical determination of the particle displacements. In PIV literature, the physical size and the overlapping ratio of these interrogation windows define the vector resolution in a given velocity vector field.

The seeding particles were hollow glass spheres, with a mean diameter of 10μm, and a specific density of 1.08. Calculated settling velocity for these particles, $u_s = 7.81 \times 10^{-2}$ *mm/s* using Eqn. (2.3)

$$u_s = d_p^{\,2} \frac{(\rho_p - \rho_w)}{18\mu} g \qquad (2.3)$$

from Raffel *et al.* (2007) is negligible when compared to the free-stream velocity (U_0 = 197 mm/s). In this equation, d_p, ρ_p, ρ_w, μ, and g represent the particle diameter, particle density, density of

water, viscosity of water and the gravitational acceleration, respectively. For the illumination of these particles, a double cavity Nd:Yag laser with a maximum energy output of 200 mJ/pulse at a wavelength of 532 nm was used. The thickness of the laser sheet was kept at 1 mm by using a spherical lens (1000 mmϕ of focal length) after a cylindrical lens (50 mmϕ of focal length) used to transform the laser beam to a laser sheet. The time difference between Frame A and Frame B is selected sufficiently large to allow the particles move approximately $1/4^{th}$ of the interrogation window size between the frames but small enough so that the effects of the out-of-plane motion on the resultant cross-correlation map is reduced to minimum. Images of the illuminated particles were captured with a CCD (Powerview, 2MP) camera having an effective pixel array size of 1600 pixels × 1200 pixels. The synchronized operation of the camera with the laser at a recording capture rate of f_{aq} = 14.5 Hz was accomplished with a model 610035 synchronizer. The synchronization was computer controlled via TSI 3G INSIGHT software. Other details of data acquisition are given in Table 2.3. In this table, components of the fields of view and the vector resolutions are given first along the streamwise direction, and then the cross-flow (lateral) direction. The parameter for the distance of the leading edge of the endplate to the cylinder front, represented by L_{LE}, is normalized by the cylinder diameter D.

In this study, the quantitative assessment of the flow structures with PIV was carried out for two types of flow configurations and a variety of experimental parameters. It has been used as the main tool in determination of the boundary layer thickness growing on the endplates and the tunnel wall for Re_D = 10,000 in absence of a cylinder. In these experiments, the water temperature, the kinematic viscosity, and the free-stream velocity were 20 °C, 1.0×10^{-6} m^2/s, 197 mm/s respectively. The details of the data acquisition, vector resolution and the magnification factors are given in Table 2.3. These experiments are supplementary studies to the work by Blackmore (2011) and discussed in Chapter 3.

The second flow configuration investigated with PIV involved the cylinder/wire model. The wire-to-cylinder-diameter ratio was kept constant at d/D = 0.059 and two different Reynolds numbers were tested; Re_D = 10,000, and 25,000. The values of the free-stream velocity, and the water temperature follow the values given in Table 2.1. The aim of these experiments was to evaluate structure of the flow within the shear-layer on the wire side of the cylinder/wire model and the near-wake region as a function of the wire angle (θ) at two different Reynolds numbers. A representative schematic of the PIV setup used in these experiments is given in Figure 2.5. The

seeding particles, laser, synchronizer, and the data acquisition computer were same as those described in the previous paragraph. However, two CCD cameras were used as shown in Figure 2.5; one was focused on the shear-layer region with an effective pixel array size of 2048 pixels × 2048 pixels (Powerview, 4MP), and another camera was focused on the near-wake region with an effective array size of 1600 pixels × 1200 pixels (Powerview, 2MP). Data acquisition from these cameras was not simultaneous and an imaging lens with 50 mm focal length was used for each camera. The fields of view covered an area of $2D \times 2D$, and $2.5D \times 1.84D$ (streamwise dimension × cross-flow dimension) with magnification factors of 19.87 pixels/mm, and 12.36 pixels/mm and vector resolutions of $0.015D$ and $0.025D$ for the shear-layer and near-wake regions, respectively. Sampling frequency was 14.5 Hz for the near-wake region but was 7.25 Hz for the shear-layer region due to the increased size of the CCD array (4MP). The number of PIV recordings captured per ensemble was 200 rec/ensemble, and 59 rec/ensemble with 3 and 5 ensembles for the near-wake and shear-layer regions respectively.

Table 2.3 Details of PIV data acquisition for different experimental configurations during the investigation of junction flow characteristics. Reynolds number is kept constant at Re_D = 10,000 for all cases.

Experimental configuration	*Tunnel wall*	*Endplate (Ellp)*	*Endplate (Sharp)*
Aim of the experiment	Measurement of boundary layer thickness along the wall or endplate surface		
Imaging Lens	105 mm		
$\lambda = L_{LE}/D$	n/a		
Field of view dimensions	$2.97D \times 2.19D$	$0.39D \times 0.29D$	
Magnification factor	9.6 pixels/mm	66.7 pixels/mm	
Vector resolution	$0.03D \times 0.03D$	$0.004D \times 0.004D$	
Number of recordings	200		
Sampling frequency	14.5 Hz		

Following the acquisition of raw PIV images, the velocity fields were retrieved through the cross-correlation of the interrogation windows from Frame A and Frame B of each PIV recording. Hart correlation was used during this process due to its higher correlation speed and lower memory requirements in accord with Hart (1998). In addition, an iterative method on grid refinement was adapted to increase the final resolution of the velocity vectors. This method initially defines the size of the interrogation windows as 64 pixels × 64 pixels, and then refines the same window into

4 smaller windows with a size of 32 pixels × 32 pixels while using the velocity information from the previously defined coarser area for the cross-correlation in the smaller windows. This recursive algorithm enhances the probability of finding a valid displacement vector peak without the need for a heavily seeded flow (Scarano and Riethmuller 1999, 2000) and is compatible with Hart's correlation technique (Hart 1998, 1999). The interrogation window overlap ratio was set to 50%. The detection of the peak in the cross-correlation map for the displacement vector is accomplished with a Gaussian peak fit function. The primary parameter in the validation of the retrieved velocity vector is its Signal-to-Noise (SNR) ratio and the values for SNR below 1.5 are considered as invalid. All of the data processing was carried out in INSIGHT 3G software supplied by TSI Inc., and the resulting vector fields had a rectangular grid of 99 vectors × 73 vectors for 2MP camera, and a square grid of 127 vectors × 127 vectors for 4MP camera. The uncertainty in PIV measurements are lower than $0.026U_0$ (see App. A.2 for details).

During the post-correlation stage, the vector field was checked for *spurious vectors*; vectors which passed SNR test in the cross-correlation algorithm but exhibited an "unexpectedly large" deviation with respect to nearby vectors were identified. For the detection of these spurious vectors, also called *outliers*, a PIV vector validation software, *CleanVec*, was used. The number of outlier vectors is less than 5% of the total number of velocity vectors in a PIV measurement. This software (*CleanVec*) was released in 1999 by Soloff and Meinhart and applies two tests on each vector within the vector field. Initially, a comparison is made between the values of each velocity component with a cut-off value. This procedure is a global validation test and is only able to detect the vectors with velocity components outside the specified range. The second procedure is based on dynamic median operator and detects smaller deviations in the vectors with respect to their neighbouring vectors. This method is widely used in PIV literature and is a version of the dynamic mean value operator (Raffel et al 2007). The use of a median operator instead of a mean value operator makes the procedure more efficient and independent of the existence of other spurious vectors in the neighbouring region, defined as a grid of 3 × 3 vectors excluding the vector being tested (Westerweel 1994). Following the removal of the detected outliers from the velocity field, the empty grid spots are replaced with artificially created vectors using another in-house software, *PostProcess*, coded in 2003 by Fu. This program calculates the replaced vectors using a Singular Value Decomposition method on a system of linear equations for a bilinear least squares fit based on 5 nearest neighbouring vectors. In addition, PostProcess software also applies data smoothing

to the velocity field prior to the calculation of velocity moments in order to minimize the noise. Further details on the data smoothing and vector replacement procedures by PostProcess software can be found in the dissertation work by Ekmekci (2006).

2.3.4. Pressure measurements

Pressure measurements were done along the circumference of the cylinder in absence of the tripwire for Re_D = 5,000 and 10,000. Mean pressure values, sampled for 10 seconds with a sampling frequency of 100 Hz, were converted to pressure coefficient, $c_p(\theta)$, using

$$c_p = \frac{p - p_\infty}{0.5\rho_w U_0^{\,2}} \qquad (2.4)$$

for the estimation of the boundary layer thickness based on the method described by Nebres (1992). The value of the reference pressure, p_∞, is calculated using,

$$p_\infty = p(\theta = 0°) - 0.5\rho_w U_0^{\,2} \qquad (2.5)$$

where $p(\theta=0°)$ is the stagnation point pressure. During the measurements, the pressure tab was located at the mid-span of the cylinder and the angular location of the tab was varied from 0° to 90° with an angular increment of 5°, and from 100° to 180° with an increment of 10°. Pressure transducer was a Model 209 (SETRA) with a pressure range from 0 to 13.78 kPa and a measurement accuracy of ±35 Pa.

2.4. Data Analysis Techniques

In this section, techniques of data analysis and definition of certain flow quantities will be presented. Results obtained from these analyses are presented in Chapter 3 and 4 for different flow configurations.

2.4.1. Time-averaged flow quantities

Based on the time-averaged flow fields from PIV data, two quantities are important for the understanding of the flow physics involved in the cylinder/wire arrangements. These are *vortex formation length* (L_F) and the *wake width* (w). Vortex formation length is measured in the streamwise direction along the cylinder symmetry axis from the base of the cylinder to the saddle point. This saddle point defines the boundary between the mean-recirculation region and the outer

flow region as mentioned in section 1.1, and is shown using the time-average streamlines $<\psi>$ and the iso-contours of the time-averaged streamwise velocity component $<u>$ in Figure 2.6(a) and Figure 2.6(b), respectively. In this study, the width of the wake (w) is defined as the lateral distance between two points, each located at either side of the cylinder symmetry line, where the profile of the streamwise velocity component reaches the free-stream velocity value. The profile is extracted from the time-averaged velocity field at the vortex formation length. Determination of the wake width is shown in Figure 2.6(c).

The time-averaged velocity fields, used to determine the vortex formation length and the wake width, are considered as statistically converged for Re_D = 10,000 according to Dong *et al.* (2006), where the comparison of between PIV data and DNS yielded a satisfactory agreement on the velocity fields by using 600 samples of PIV recordings. For the flow fields sampled for Re_D = 25,000, the number of samples is selected to be 200 samples with 3 ensembles (600 samples as a total) for consistency with the experiments at Re_D = 10,000.

2.4.2. Spectral analysis

Spectral analysis is a useful tool in determining the frequency components of a signal and their associated power distributions. This analysis is mainly used for the quantification of the predominant frequencies in acquired velocity signals, i.e. vortex shedding frequencies. In addition, the autospectral amplitude of these velocity fluctuations at the predominant frequency can be considered as an indication of the coherency and strength of the vortex shedding. This analysis is also performed to evaluate the unsteady flow characteristics encountered in the junction of the cylinder with a wall boundary.

Since the analyzed data is the time trace of the streamwise velocity component with a finite number of samples, the discrete Fourrier Transformations (DFT), given by,

$$U_k = \sum_{n=1}^{N} u_n e^{-i2\pi(k-1)\left(\frac{n-1}{N}\right)} \qquad k = 1,2,\ldots, N \qquad (2.6)$$

is applied to the signal followed by the calculation of the auto-spectral density using Eqn. (2.7).

$$S_u = U_k^{*} U_k \qquad (2.7)$$

In Eqn. 2.6, u_n, U_k, and N represent the analyzed signal, its discrete Fourier Transform, and number of data points respectively. In Eqn. (2.7), U_k^* denotes the complex conjugate of the discrete Fourier Transform for the signal U_k. Finally, the auto-spectral density S_u, is normalized using Eqn. (2.8).

$$\tilde{S}_u = \frac{2\sqrt{S_u}}{N} \qquad (2.8)$$

Although the same spectral analysis has been applied to the data acquired data with CTA and PIV techniques in the experiments related to the cylinder/wire arrangements, the data sampling frequencies and sampling times are different as mentioned earlier and given in Tables 2.2 and 2.3. While the CTA data consists of 4 ensembles (for the *St-θ* data), and 39 ensembles for (for Q2D data) each with 2,048 data points/ensemble, PIV data contains 200 data points per ensemble. Due to the finite sampling size, the uncertainties in the cylinder diameter (ΔD = 0.35 mm) and the free-stream velocities (ΔU_0 = 1.25 mm), the uncertainties arise in the resulting Strouhal numbers, *St*. These uncertainties are determined using the Root-Sum-Square equation as suggested by Moffat (1988) and given in Table 2.4. Details of this error analysis can be found in App. A.1.

Table 2.4 Estimated values of uncertainty in Strouhal numbers, ε_{St}, for different Reynolds numbers and experimental techniques. ε_{St} is given in percentile of a reference Strouhal number of 0.2.

Reynolds number	**Uncertainty in Strouhal number, ε_{St}/St, [%]**		
	CTA data		**PIV data**
	Q2D	***St-θ***	
5,000	1.76	3.67	n/a
10,000	1.73	2.05	5.40
15,000	1.10	1.36	n/a
25,000	1.00	0.97	2.10
30,000	1.02	0.88	n/a

In addition, the values for the vortex shedding frequencies are corrected to account for the blockage effect imposed by the cylinder, which is 8.3%. The frequency data, presented in this work, are corrected using the method proposed by Maskell (1965). The details of this procedure can be found in App. B. Values of the drag coefficient and the base pressure parameter, required for this correction procedure, are taken from Hover *et al.* (2001) and Norberg (1994), respectively.

2.4.3. Time-frequency analysis

The Fourier analysis described in section 2.4.2 produces a set of time-averaged spectral coefficients over the whole data acquisition time. These coefficients are useful in identifying the dominant frequency in the velocity fluctuations. However, the Fourier spectrum fails to

demonstrate the time dependence of the dominant frequency in a signal. In the present investigation, a time-frequency analysis is used to investigate the temporal dependency of the dominant frequency peak using short-time Fourier transformation (STFT).

The major difference between STFT and DFT is the data window size while the algorithm is the same. STFT breaks the signal into smaller windows (segments) and performs FFT to each window. This allows for the detection of changes in the autospectral density with time. A small window size increases the temporal resolution, while reducing the frequency resolution. Therefore, the window size in STFT must be chosen carefully. During the present analyses, each window was sized to contain 512 data points (for *St-θ* experiments) and 128 data points (for Q2D experiments). In addition, an overlap between the consecutive windows by about 94% is applied to achieve adequate compromise between the frequency and temporal resolutions.

2.4.4. Phase analysis and vortex filament angle

Vortex filament angle is defined as the angle between the shed Karman vortex filaments and the cylinder axis when viewed from the side of the cylinder. The acquisition of the time traces of the streamwise velocity component, *u(t)*, at two discrete points with a spanwise distance quantifies the phase difference in the vortex shedding process between the two cross-sectional planes.

The phase angle difference ($\Delta\varphi$) between the two CTA velocity signals was evaluated from the cross-correlation of the time-frequency analyses employing short-time Fourier transformation (STFT), as mentioned in section 2.4.3. For details on these analyses, the reader can refer to Khoury (2012). Using the phase angle difference ($\Delta\varphi$) information, the vortex filament angle, ϕ, between the two points was calculated with respect to the cylinder axis as a function of time simply from

$$\phi(t) = \tan^{-1}\left(\frac{U_c T_{vs} \Delta\varphi(t)}{2\pi(3D)}\right) \qquad (2.9)$$

where U_c is the convection speed of vortical structures, $\Delta\varphi$ is the phase angle difference between the two hot-film signals, T_{vs} is the vortex shedding period and $3D$ (which appears in the denominator of the formula) is the spanwise distance between the two CTA probes. The value of the convection speed U_c was taken to be about $0.85U_o$, based on the measurements of Lin and Hsieh (2003) at $4.3D$ downstream of the cylinder. This analysis revealed that the vortex filament angle, ϕ, between the two spanwise points changes as a function of time.

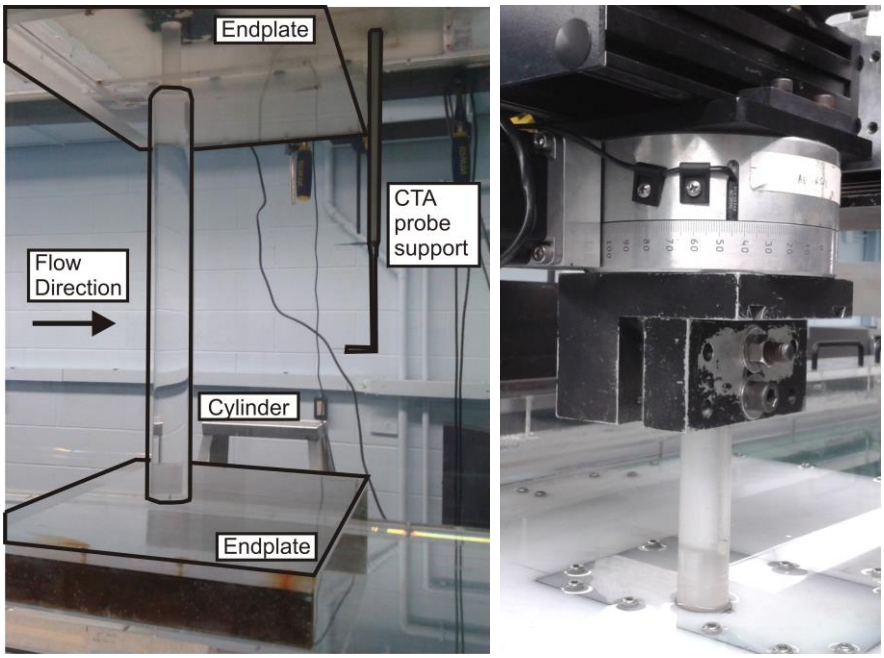

Figure 2.1 Experimental setup employing an endplate on each end of the cylinder (on the left) and a close-up view of the cylinder/rotary stage arrangement (on the right).

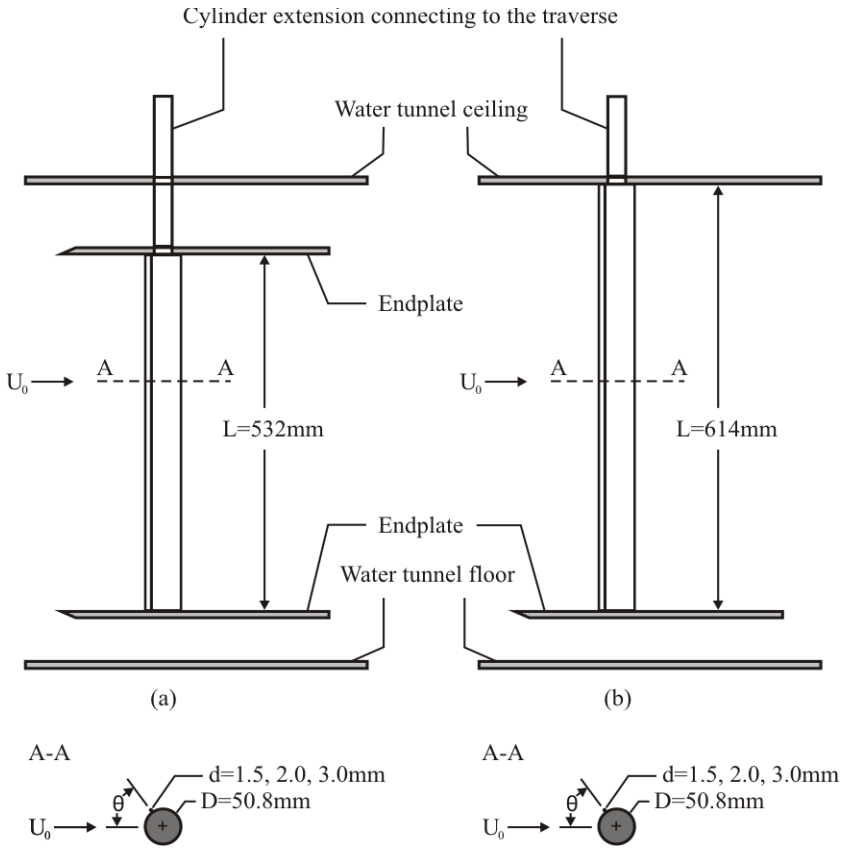

Figure 2.2 Schematic side view of the experimental setup and cross-sectional details of the cylinder/wire arrangement in the experimental configurations with symmetrical, given in part (a), and asymmetrical, given in part (b) end conditions.

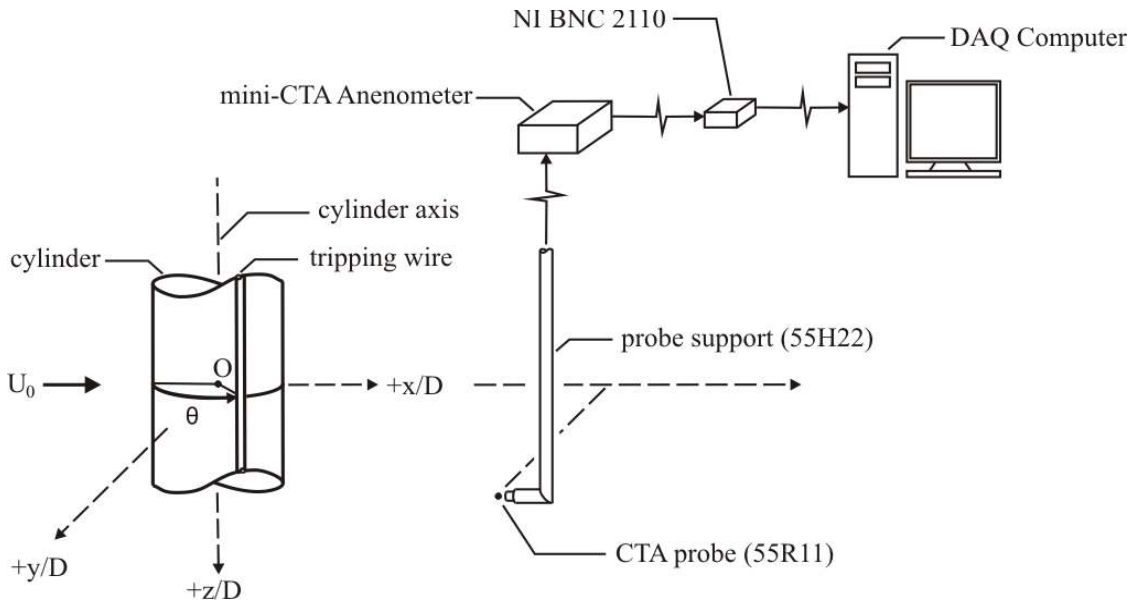

Figure 2.3 A representative schematic of the experiment setup employing the CTA system with a single probe. The cylinder/wire and the probe holder drawings are not scaled.

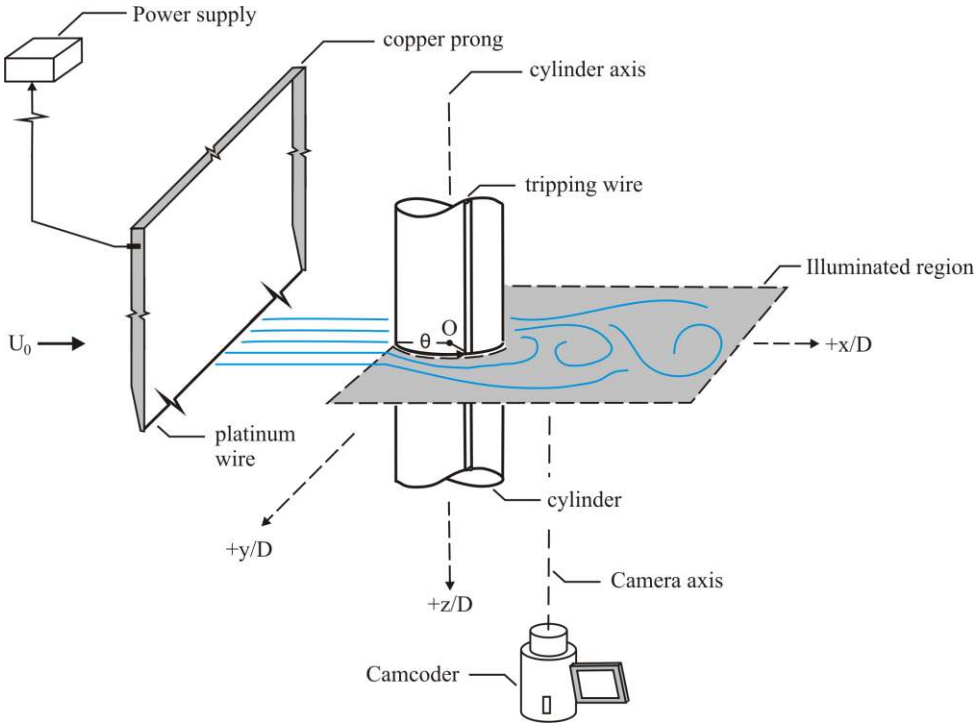

Figure 2.4 A representative schematic of the experimental setup employing the hydrogen bubble flow visualization system. The cylinder/wire and the platinum wire holder drawings are not scaled.

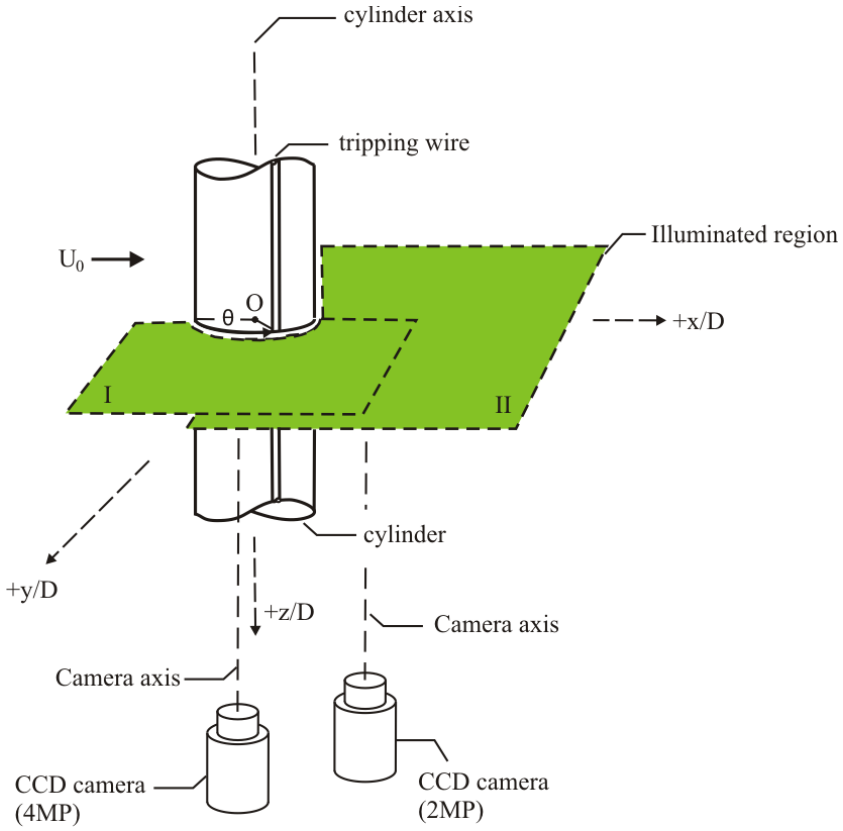

Figure 2.5 An isometric schematic of the experimental setup employing PIV system for the quantitative assessment of the flow in the shear-layer (I) and near-wake (II) regions of the cylinder/wire experimental model.

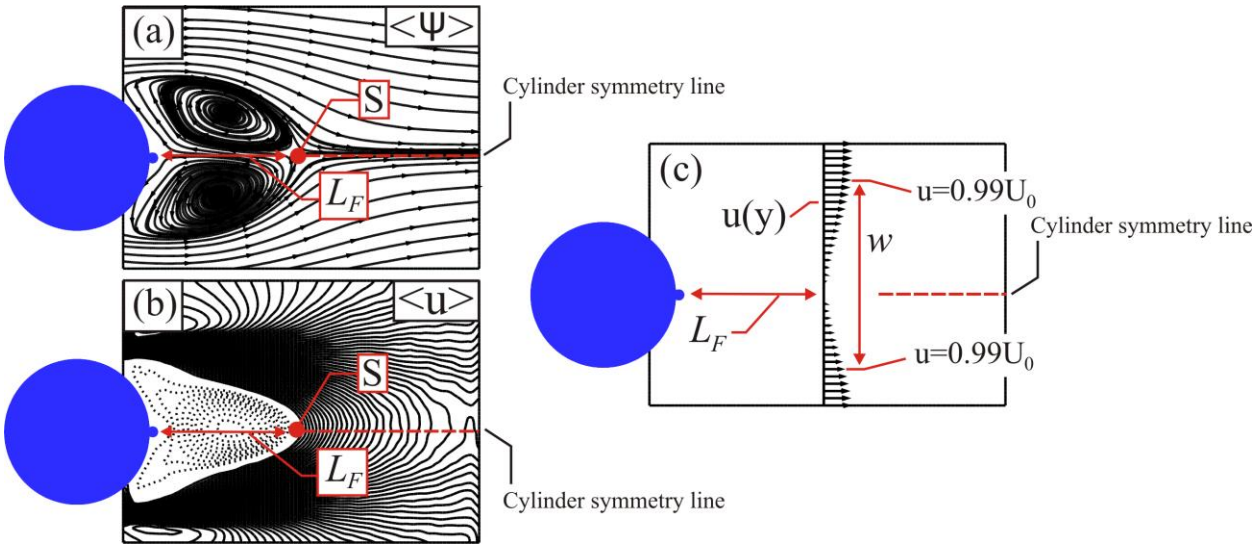

Figure 2.6 Sketch defining the vortex formation length (L_F) on the left and wake width (w) on the right based on the time averaged velocity fields.

Chapter 3

Flow Characteristics in Absence of a Tripwire

In this chapter, efforts are put forward towards understanding the flow features around the cylinder in absence of a wire, and to find the optimum experimental configuration that provides a quasi two-dimensional vortex shedding process so that the effects of the tripwire can be evaluated later using that configuration in Chapters 4 and 5 with a greater confidence. Due to their relevance, this chapter presents experimental results in two main topics: *(i)* the junction flow at the end of the cylinder, and *(ii)* the degree of the flow two-dimensionality in the near-wake of the cylinder.

Vortex shedding from a finite, circular cylinder can exhibit three-dimensional flow features due to the interaction of the boundary layer growing along the wall which constrains the cylinder with the cylindrical body and the inherent secondary instabilities arising in the wake. The contribution from these sources to the spanwise disturbances in the shed Karman vortices can be minimized with the use of endplates. In the first part of this chapter, a review of the literature on the wake quasi two-dimensionality and the junction flow dynamics will be given. The second part of the chapter will present the experimental results on the features of the horseshoe vortex systems encountered in the junction region of a cylinder for Re_D = 10,000 with different oncoming boundary layer characteristics and two different geometries of the endplate leading edge. In the final section, how the symmetry of the cylinder end conditions influence the degree of quasi two-dimensional vortex shedding will be addressed for the Reynolds number range of $5{,}000 \leq Re_D \leq 30{,}000$.

3.1. Review of the Literature

3.1.1. Quasi two-dimensional vortex shedding

In the case of a truly two-dimensional vortex shedding from a circular cylinder, the wake flow at a cross-sectional plane is representative of and in phase with the flow at any other planes along the entire span (excluding the end regions). In addition, the orientation of the shed Karman vortices is

parallel to the cylinder axis in a truly two-dimenional vortex shedding (Williamson 1989). However, the vortex shedding behind a finite, i.e. nominally two-dimensional, circular cylinder can deviate from this ideal case due to the inherent secondary instabilities of the wake, oblique vortex shedding, vortex splitting and vortex dislocations. Below, summary of the past research is given.

A well-known effect of the wake three-dimensionality on vortex shedding characteristics are discontinuities in the variation of Strouhal number as a function of Reynolds number encountered at $Re_D \approx 190$, and 260. These discontinuities are due to Mode A and Mode B secondary instabilities in the wake transition regime respectively (Williamson 1996), and were previously mentioned in section 1.1. In addition, there is little agreement on the distribution of Strouhal number within the laminar regime, i.e. $49 \leq Re_D \leq 190$, as some discontinuities were observed in St-Re_D curves by a number of researchers and were hypothesized to be caused by an intrinsic "fluid-mechanic" phenomenon (Tritton 1959), flow non-uniformities (Gaster 1969), regime transition for vorticity diffusion in vortex shedding (Gerrard 1978), and cylinder vibrations (Van Atta and Gharib 1987). In absence of the cylinder vibrations and flow non-uniformities, the discontinuity in St-Re_D curve has been shown to exist at $Re_D = 64$ and has been related to a transition in the modes of oblique shedding by Williamson (Williamson 1988, 1989). *Oblique shedding* is a mode of vortex shedding from a cylinder where the vortex filaments are shed with a non-zero angle relative to the spanwise cylinder axis. Non-parallel orientation of vortex filaments with respect to the cylinder spanwise axis is a result of the difference in the base pressure at the mid-span and the ends of the cylinder. That is, the base pressure near the cylinder ends is higher and leads to a longer vortex formation region with a vortex shedding frequency lower than its counterpart in the mid-span. This dictates the bending of the filaments along the span even for very long cylinders, $L/D \approx 10^3$ (Williamson 1989).

Some researchers have been able to obtain parallel shedding conditions for low Reynolds numbers by manipulating the end conditions of the cylinder via various techniques; application of suitably inclined end plates (Williamson 1989, 1988), use of coaxial end cylinders of slightly larger diameter (Eisenlohr and Eckelmann 1989), the transverse control cylinder technique (TCCT) (Hammache and Gharib 1989, 1991), and the suction tube technique (Miller and Williamson 1994). For higher Reynolds numbers in the shear-layer transition regime, fewer studies have been successful in the control of vortex shedding mode. Prasad and Williamson used (inwards) inclined

endplates and achieved parallel shedding for a Reynolds number range up to 6,000 (Prasad and Williamson 1997). In addition, Luo and Xia showed that the use of transverse control cylinders placed upstream of the main cylinder, i.e. TCCT technique, promotes the invariance of the time-averaged base pressure and surface pressure distributions along the span for Reynolds numbers at the order of $O(10^4)$ (Luo and Xia 2005). Among the methods of promoting parallel shedding, the use of endplates aligned with the free-stream direction will be focused on from this point forward.

In general, the use of the endplates, when aligned with the free-stream direction, aims to restart the boundary-layer growth along the wall boundary constraining the cylinder. This effectively reduces the oncoming boundary-layer thickness upstream of the cylinder ends. Bearman (1965) showed that the distribution of the base-pressure along a cylinder is not constant near the ends of the cylinder for $Re_D = 1.4_{\times}10^5$ when the endplates are omitted. This variance suggests a pressure gradient driven (spanwise) inflow towards the middle of the cylinder span. However, with the introduction of endplates, the pressure gradient reduces due to the reduction in the boundary layer thickness along the endplates. For a low Reynolds number range of $50 \leq Re_D \leq 250$, Gerick and Eckelmann studied the influence of the end-plates and free ends on the vortex shedding frequency (Gerick and Eckelmann 1982). They show that near the spanwise ends of a cylinder, the boundary (be it an endplate or a free-end) directly affects the vortex shedding, resulting in a vortex shedding frequency 10 to 15% lower than its counterpart in the mid-span of the cylinder. These regions, referred to as *affected regions*, are shown to scale in their size inversely with the end-plate size and the cylinder diameter (Gerich and Eckelmann 1982). Stager and Eckelmann studied the shedding characteristics within the end regions of the cylinder for a Reynolds number range of $300 \leq Re_D \leq$ 4,000. Through a systematic investigation by varying the endplate and cylinder diameter, they showed that the size of the affected region decreases with increasing Re_D (Stager and Eckelmann 1991).

At the boundary of the affected regions with the unaffected region, the amplitude of the velocity fluctuations are shown to be modulated at a beating frequency, as a result of the difference in the vortex shedding periods between these neighbouring cells for $200 < Re_D$ (Gerich and Eckelmann 1982, Williamson 1988, 1989). Variance in the shedding frequency across this boundary results in a phase difference in the same signed vortices shed from the body. This phase relationship is unsteady, and leads to complex interaction of the vortices; *vortex splitting* (Eisenlohr and Eckelmann 1989), or *vortex dislocations* (Williamson 1988, 1989, 1992, Miller and Williamson

1994). While there is loss of coherency within the vortex filaments during a vortex dislocation, vortex splitting involves the branching of a single vortex filament onto two separate filaments. Both of these phenomena are three dimensional flow structures and occur at the beating frequency for low Reynolds numbers ($200 < Re_D$).

For higher Reynolds numbers, Prasad and Williamson (1997) showed that vortex dislocations continue to occur and lead to oblique shedding within the sub-critical regime for $1{,}600 \leq Re_D \leq 2{,}600$. Based on their flow visualization and hot-wire measurements, they report instantaneous filament angles of about 4°-6° when the endplates are aligned with the free-stream direction. The level of three-dimensionality (the vortex filament angle ϕ) is shown to lead to a deviation in the vortex shedding frequency (ΔSt) in the mid-span. This deviation is shown to be smaller than 1% of its value for the parallel shedding condition for $\phi \leq 6°$ (Prasad and Williamson 1997). In an earlier study, the relationship between the angle of obliqueness and the vortex shedding frequency for parallel vortex shedding was established through a cosine function, $St = St_\phi / cos\phi$, within the laminar regime. In this equation, St, St_ϕ, and ϕ represent the Strouhal numbers in the parallel and oblique shedding configurations, and the angle of obliqueness, i.e. vortex filament angle, respectively (Williamson 1989). In addition to the variance of the Strouhal number due to the obliqueness of the wake, the velocity spectra also is affected by the oblique shedding; the spectra broadens around the shedding frequency as the filament angle increases (Prasad and Williamson 1997). Szepessy investigated the spanwise correlation of vortex shedding in the high sub-critical regime at $Re_D = 4.3\times10^4$ by simultaneous measurements of pressure from three surface taps around the mid-span. He showed that as the correlation of the pressure signals, i.e. quasi two-dimensionality, decreases, the probability density function of the vortex shedding phase drift broadens while its mean remains centered around $\phi = 0°$. This implies a parallel shedding in the time-averaged sense but reveals that even such a flow configuration can exhibit a wide range of filament angles at a high sub-critical Reynolds number (Szepessy 1994). For $Re_D > 5{,}000$, Prasad and Williamson (1997) postulate that the vortex dislocations are inherent to the flow, regardless of the end conditions due to a transition in the wake even with parallel shedding conditions; the spectral bandwidth undergoes a sudden increase at $Re_D = 5{,}000$ and increases with further increase in Reynolds number. The increase in the bandwidth of the autospectral density for parallel shedding is similar to the broadening of the velocity spectra encountered in the oblique shedding

configuration, and is due to vortex dislocations at these Reynolds numbers (Prasad and Williamson 1997).

Within the range of Reynolds numbers considered in this dissertation ($5{,}000 \leq Re_D \leq 30{,}000$), it is understood from the previous studies that the degree of wake quasi two-dimensionality will be affected by the presence of vortex dislocations (Szepessy 1994, Prasad and Williamson 1997) and/or vortex splitting (Khoury 2012). In addition, the aspect ratio of the cylindrical model, the ratio of the length to its diameter, should be at least 60 for $4\times10^3 \leq Re_D < 1\times10^4$, and 25 for $1\times10^4 \leq Re_D \leq 4\times10^4$ to avoid direct effect(s) of the end conditions on the wake flow according to Norberg's study (Norberg 1994). However, the aspect ratio (L/D) can be 13.5 at most based on the dimensions of the test section, and the model as given in section 2.1, and 2.2 respectively. On the other hand, when the endplates are used, Fox and West (1990) required that L/D ratio must be greater than 7. In this study, the aspect ratios of the cylinder (L/D) satisfy this requirement. At this point, it is necessary to extend the literature review onto the dynamics of the junction flows for a better understanding of how the upstream flow conditions near the cylinder ends are affected by the cylinder/wall boundary junction.

3.1.2. Junction flows

The boundary layer growing along a wall surface undergoes a three-dimensional flow separation when it faces an obstacle due to the imposed adverse pressure gradient at the upstream part of the obstacle. As a result of this pressure gradient, the boundary layer separates, rolls up, stretches around the obstacle, and forms a system of vortices known as horseshoe or necklace vortices. Some examples of the effects of horseshoe vortices (HSV) include erosion in the river bed around the bridge piers, interference drag arising from the aircraft wing/fuselage junctions, changes in the heat transfer of the turbo-machinery components. The dynamics of horseshoe vortices can exhibit either steady or unsteady features in size, location or circulation of the vortices depending on the Reynolds number, obstacle aspect ratio, and boundary layer characteristics (Baker 1978, 1980, 1985, Simpson 2001).

Systems of horseshoe vortices were investigated by Baker by experimenting on a circular cylinder/wind tunnel wall junction for a laminar approaching boundary layer. He classifies the systems of horseshoe vortices as a function of Re_D and D/δ^*, where D is the cylinder diameter and δ^* is the boundary layer displacement thickness. It was observed that an increase in Re_D yields an

increase in the number of vortices, from 2 to 6, for the steady systems (Baker 1979). Greco's study (1990) reveals the mechanisms leading to five different flow regimes in a horseshoe vortex system. In his discussion about the steady regimes, the stability of the vortex systems is related to the balance between the convection of vorticity downstream from the upstream boundary layer and the vorticity diffusion via vortex stretching (Greco 1990).

Different values have been reported for a threshold of Reynolds number where laminar, unsteady systems are observed. The system of horseshoe vortices becomes unsteady for $Re_D > 5000$ (Baker 1979), $Re_D > 4000$ (Visbal 1991), $Re_D > 1000$ (Thomas 1987), and $Re_D > 1700$ (Greco 1990). Based on hot-wire measurements, Baker reports two different frequencies of oscillations, namely a low frequency at $St = 0.26$ (for $Re_D = 4{,}720$), and a high frequency at $St = 0.40$-0.60 (for $Re_D = 4{,}790$), where $St = fD/U_0$. If Re_D is increased further, an irregular regime is dominant in the junction region (Baker 1979). Thomas found that the frequency of formation and the convection speed of vortices towards the cylinder increases with increasing Reynolds number for $3{,}000 \leq Re_D \leq 13{,}000$. For $Re_D = 10{,}000$, he determined a Strouhal number of $St = 0.32$ (Thomas 1987).

In Simpson's review, the horseshoe vortices, referred to as *primary vortices*, are shown to have the same rotational orientation as the boundary layer generated vorticity leading to the entrainment of high speed free stream fluid, which enhances mixing in the junction region (Simpson 2001). Seal *et al.* (1995) investigated a laminar, unsteady horsehoe vortex system at the junction of a rectangular block and flat plate for a Reynolds number based on the boundary layer displacement thickness of $Re_{\delta^*} = 298$. One of the conclusions, based on their hydrogen bubble flow visualization and PIV measurements, indicate that the horseshoe vortices interact with the surface fluid adjacent to the plate, and generate vortices with opposite-signed vorticity, referred to as *secondary vortices*. The fluid affected by the secondary vortices ejects from the surface, and surround the primary vortices. This leads to a vortex shedding via the cut off of vorticity supply from the boundary layer (Seal *et al.* 1995). After a certain Reynolds number, the disturbances in the vortices are amplified and fed upstream in the form of hairpin vortices. This leads to a non-uniform vortex stretching along the vortex tube, and thus to a loss of coherency in the large scale vortex (Greco 1990).

Some studies have focused on junction flows with a turbulent oncoming boundary layer. Davenport and Simpson (1990) performed an experimental study with a wing/wall junction, revealing time-dependent and time-averaged turbulent structures in the symmetry plane of the junction. Two distinct time-averaged flow regions were reported; a thin upstream region with a

low mean backflow, and a relatively thick downstream region, with intense circulation of the junction vortex. Bi-modal histograms of velocity fluctuations indicate a significant increase in turbulent stresses, i.e. a bi-stable velocity variation (Davenport and Simpson 1990). Using the same wing shape and a wind tunnel wall junction, Fleming *et al.* (1993) studied the junction and the wake flow together. Based on their hotwire data and the comparison with past researchers' data sets, they concluded that the difference in the thickness of the turbulent boundary layer has a secondary influence on the flow structure. The primary factor given is the pressure field associated with the wing/wall junction, and it was found that the flow features scale with the characteristic length scale of the obstacle (Fleming *et al.* 1993).

In a study of turbulent systems of horseshoe vortices, Baker (1980) tested the physics of the flow in a circular cylinder-flat plate junction over a large range of Reynolds numbers from Re_D = 4,000 to 9×10^4. The streamwise distance of the formed horseshoe vortices was found to be inversely proportional to the Reynolds number and increase with increasing displacement thickness (Baker 1980). Combining available experimental results on laminar and turbulent systems, Baker (1985) developed formulations for predicting the streamwise locations of the vortex as a function of displacement thickness and Reynolds number.

Numerical studies on the systems of horseshoe vortices were performed by Deng and Piquet (1992), Escauriaza and Sotiropoulos (2011a, 2011b), and Gand *et al.* (2010). Deng and Piquet performed 3-D incompressible Navier Stokes calculations, using an algebraic viscosity model for the turbulent closure. The computations compared well with the previously reported experiments, and the main features of the HSV systems were captured. Escauriaza and Sotiropoulos performed comprehensive Detached Eddy Simulation (DES) computations for a cylinder-flat plate junction flow at multiple Reynolds numbers ($Re_D = 2\times10^5$ and 3.9×10^5). The results compared well with the existing experimental data, and provided insights into the small scale eruptions that change the coherent structure dynamics of the HSV system in the junction. In addition, budgets of turbulent kinetic energy (TKE) were computed and compared to the available experimental data. These demonstrated the applicability of DES to properly capture the complex flow physics around a circular cylinder-flat plate junction (Escauriaza and Sotiropoulos 2011a). Escauriaza and Sotiropoulos also performed a numerical study of the dynamics of inertial particles within a junction flow using a Lagrangian model and DES. The study neglected particle to particle interactions and found that the model was able to reproduce the findings of many sediment

transport experiments (Escauriaza and Sotiropoulos 2011b). Gand *et al.* (2010) performed a Large Eddy Simulation (LES) on a wing-body junction at Reynolds number of $Re_D = 2.8\times10^5$, which concentrated on the legs of the HSV system swept around the root of the wing. The simulations successfully captured the main features of the flow, but the strength of circulation in vortex legs appeared to be underestimated in the LES computations.

Wei *et al.* performed smoke and Laser Induced Fluorescence (LIF) flow visualization experiments supported with Laser Doppler Velocimetry (LDV) measurements on the horseshoe vortex systems formed in the junction of a flat plate and obstacles of various cross sections. It was found that as the bluntness of the obstacle is decreased by varying the model cross sections from a square to a circle and then a prism, a decrease in the horseshoe vortex strength was found, and the vortices formed closer to the object. These findings were related to the reduction in the adverse pressure gradient imposed by the obstacle due to the changes in its cross section (Wei *et al.* 2008). Simpson (2001) also reviewed the effect of the increase in the bluntness factor for a wing nose in the wing/wall junction, and pointed out that an increase in the vortex strength is proportional to the increase in the bluntness factor (Simpson 2001).

Lin *et al.* (2002) investigated the effect of the height-to-width ratio of a vertical plate positioned on a flat plate for $400 < Re_D < 11{,}000$. They also observed four different regimes: steady systems, unsteady systems with small displacements, periodic breakaway systems and turbulent systems. For both of the oscillatory systems, the Strouhal number based on the boundary layer thickness (St_δ) change slightly between 0.0611 and 0.0896. It is discussed that the boundary layer thickness is a key parameter for the systems of unsteady horsehoe vortices (Lin *et al.* 2002).

Szepessy (1993) shows that the Karman instability of the wake is decoupled with the flow instability of the junction region. In two other studies, Baker (1979), and Thomas (1987) independently tested the effect of vortex shedding on the behaviour of the horseshoe vortex systems. In their experiments, a splitter plate was used to prevent the formation of regular Karman vortices. Disruption of the regular vortex shedding in the wake had no impact on the development of the horseshoe vortices. Thus, it was concluded that the behaviour of horseshoe vortex systems depends on the junction flow physics, and is not related to the instability in the wake region (Baker 1979, Thomas 1987). Sahin *et al.* (2007) performed PIV experiments on the flow past a circular cylinder in the junction and wake regions to identify the flow interaction between these regions. It was found that the vortex formation length is the smallest near the entrainment region; a high

mixing region formed between the cylinder shear layers and the horseshoe vortices as the horseshoe vortices are swept around the cylinder. In addition, the wake region varied along the span of the cylinder close to the cylinder ends (Sahin *et al.* 2007).

3.2. Scope of the Current Chapter

This chapter is related to the characteristics of the sub-critical wake flow around a nominally two-dimensional circular cylinder in absence of a tripwire. Based on the review of the literature provided on the wake quasi two-dimensionality, the flow is expected to exhibit features of three-dimensionality such as oblique shedding, vortex dislocations and/or vortex splitting. It is also understood that the promotion of wake quasi two-dimensionality is attainable with the endplates aligned with the free-stream direction.

The remaining sections of this chapter initially focus on how the geometry of the endplate leading edge is affecting the flow conditions in the junction. There are two geometries tested; *i)* sharp leading edge, and *ii)* elliptical leading edge. The distance between the endplate leading edge and the cylinder front is kept constant at $\lambda = 2.5$ for both of the endplates based on the suggestions in the literature (Stansby 1974, Szepessy and Bearman 1992, Szepessy 1993, Khoury 2012). The Reynolds number is kept constant at $Re_D = 10{,}000$ throughout this investigation. The results on the junction flow characteristics, given in section 3.3, build largely on the work reported in Blackmore (2011) with the new findings of the current study by presenting the boundary layer growth rate along the endplates and the tunnel wall, and the flow visualization results on the junction flow around the cylinder/endplate configuration with the sharp leading edge. Then, the selection on the leading edge geometry for the endplates is made such that the resulting flow configuration near the cylinder ends experiences a slight increase in the time-averaged streamwise velocity. This objective is in accord with the main goal of the promotion of two dimensionality, as reviewed in section 3.1.1.

In the remainder section of this chapter, the vortex shedding characteristics at two distinct points in the wake are compared in order to quantify the effect of the symmetric end conditions on the cylinder wake flow for all Reynolds numbers under consideration, i.e. $5\times10^3 \leq Re_D \leq 3\times10^4$. During this part of the study, the symmetry is maintained in terms of the boundary layer thickness and the flow conditions at the upstream portion of the cylinder/wall junction. For the symmetrical case, one endplate is employed at each end of the cylinder, as shown in Figure 2.2(a). On the other

hand, the asymmetrical case includes a cylinder/endplate junction at the bottom and a cylinder/tunnel wall junction at the top, as shown in Figure 2.2(b). The geometry of the endplate leading edge is based on the aforementioned selection (to be discussed in section 3.3), and is identical for all of the endplates. The overall goal of this last section (section 3.4) is twofold: *(i)* to quantify the degree of two-dimensionality for both of the symmetrical and asymmetrical configurations, and *(ii)* to determine the optimum experimental configuration promoting the most two-dimensional vortex shedding mode in the wake.

3.3. Flow Dynamics in the Junction

3.3.1. Characteristics of the approach flow

In order to study the effects of the endplate leading edge geometry on the dynamics of horsehoe vortices formed in the junction, the thickness of the boundary layer and its transitional characteristics need to be understood. In this section, the variance in the oncoming boundary layer features will be presented prior to the discussion of the horseshoe vortices.

As mentioned in sections 2.2 and 3.2, two different geometries of endplate leading edge were tested. Initially, the tip geometry was designed using an elliptical geometry such that the flow remains attached at the leading edge of the endplate in order to obtain a thinner, newly emerging laminar boundary layer. The selection of the geometry for the elliptical leading edge was based on Narasimha's numerical study (Narasimha 1994), which was related to the prediction of the flow separation at the tip of a flat plate for different leading edge geometries. According to his results, a set of values for the axis ratio of 8 ($a/2b = 4$) and $n = 2$, based on

$$y = b\left(1 - \left(\frac{(a - x)}{a}\right)^{n}\right)^{1/n} \qquad (3.1)$$

promotes attached flow at the tip region, and was chosen to define the tip of endplate. In this equation, x, and y define the coordinates along the streamwise and lateral directions, respectively. The second endplate was designed with a sharp leading edge, which had a bevel angle of 23.6° relative to the approach flow on the side facing away from the cylinder. The other side of the endplate is kept flat. This configuration is designed to force flow separation/re-attachment around the endplate tip. A discussion on the effects of this flow separation was given in Blackmore (2011).

The boundary layer thickness, $\delta(x)/D$, along the water tunnel wall and along the endplates with two different leading edge designs is presented in Figure 3.1 based on the time-averaged flow fields obtained from PIV measurements for a free-stream velocity of U_0 = 197 mm/s. During the measurement of the boundary layer thickness, the cylinder was not in place within the test section. In addition, the theoretical variations in the thicknesses of the laminar and turbulent boundary layers from (Schlichting 1968) are superimposed for comparison with the measurements. The experimental values of the boundary layer thickness increase approximately from $0.1D$ to $0.225D$ for $5 \leq x/D \leq 23$ along the tunnel wall, and from $0.05D$ to $0.1D$ for $0.9 \leq x/D \leq 5.2$ along the endplate with an elliptical leading edge. In these results, the streamwise distance of the measurement point is referenced from the entrance of the water channel test section, or from the endplate tip. For the endplate with the sharp leading edge, the variables x and δ_1/D used in the calculations of the theoretical boundary layer thicknesses represent the streamwise distance of a point to the time-averaged re-attachment point on the endplate, and the boundary layer thickness measured immediately downstream of this re-attachment point respectively. It can be observed from Figure 3.1(c) that the thickness of the boundary layer increases from $0.18D$ to $0.36D$ for $0.9 \leq x/D \leq 5.2$. The thickness of the boundary layer along the tunnel wall stays lower than the value of $0.25D$, which is well below the height of the endplates ($1.25D$). The growth of the boundary layer aligns well with the laminar boundary layer growth for the case of the water tunnel wall, and for the case with the attached flow along the endplate, i.e. endplate with the elliptical leading edge. On the contrary, it follows the growth for a turbulent boundary layer in the case of a re-attached flow along the endplate that had the sharp leading edge.

At this point, a new convention for the ease in naming of the experimental configurations is proposed: cylinder/tunnel wall junction: *Case I*, cylinder/endplate junction with the sharp leading edge: *Case II*, and cylinder/endplate junction with the elliptical leading edge: *Case III*. Based on the experimental data, the approach boundary layer flow is considered to be laminar for the cylinder/tunnel wall junction *(Case I)*, and for the cylinder/endplate junction with attached flow (*Case III*), while it is turbulent when the flow is separated at the endplate tip (*Case II*). Following the classification of the boundary layer states, the Reynolds numbers based on the boundary layer displacement thickness, Re_{δ^*}, and cylinder-diameter-to-displacement thickness ratio, D/δ^*, are given in Table 3.1 for all cases under consideration. In this table, the displacement thickness, δ^*, is calculated using the formulations of $\delta^* = 0.344\delta$ for a laminar boundary layer, and $\delta^* = 0.125\delta$

for a turbulent boundary layer for a flat plate as given by Schlichting (1968). Based on the vector resolution in the experiments, the uncertainty in the boundary layer thickness is estimated to be in the order of 0.03D for *Case I*, and 0.004D for both *Case II* and *Case III*. A conservative measure for the statistical uncertainty on the time-averaged streamwise velocity component is calculated as 0.014U_0 (Blackmore 2011).

Table 3.1 Cylinder-diameter-to-displacement thickness-ratio, Reynolds numbers based on boundary layer displacement thickness, and the cylinder diameter for all of the flow configurations. (*Case I*: cylinder/tunnel wall, *Case II*: cylinder/endplate with the sharp tip, *Case III*: cylinder/endplate with the elliptical tip)

Quantity	***Case I***	***Case II***	***Case III***
		λ=2.5	*λ=2.5*
D/δ^*, [-]	12.9	31.7	37.5
Re_{δ^*}, [-]	773	315	267
Re_D, [-]	10,000		

3.3.2. Characteristics of the flow at the junction

The characteristics of the horseshoe vortices encountered in the junction of the cylinder with the endplates having either a sharp leading edge or an elliptical leading edge have been reported by Blackmore (2011) under identical flow conditions. Prior to going over the findings of the current study, it is imperative to review the previous results.

The system of horseshoe vortices in the vicinity of the cylinder/endplate junction with an elliptical leading edge (*Case III* with λ = 2.5) consists of a well-defined periodic shedding of vortices (St = 0.86) with qualitatively similar aspects to the system of horseshoe vortices encountered in the cylinder/tunnel wall junction. In the vortex shedding process for the cylinder/endplate junction (with the elliptical leading edge), the vorticity is supplied into the growing vortex by the boundary layer flow and the supply in vorticity is cut via the secondary vortex with the opposite sign of vorticity (compared with the growing vortex). The system is a laminar, unsteady 4-horseshoe vortex system with 2 primary vortices (Blackmore 2011). On the other hand for the endplate with a sharp leading edge (*Case II*), the significant increase in upstream vorticity, which originates from the flow separation at the sharp leading edge, causes the primary vortex to entrain additional vorticity and prevent the periodic decrease in magnitude and size associated with the regular behavior of the system. The horseshoe vortex system for the cylinder/endplate junction with a sharp leading edge do not show a well-defined periodicity (Blackmore 2011).

Additional hydrogen bubble flow visualization experiments are conducted to further understand the system of horseshoe vortices seen in the junction of the cylinder end with the endplate having a sharp leading edge (λ = 2.5). Figure 3.2 shows two representative images from these flow visualization experiments, conducted at two different values of Re_D, to be exact at Re_D = 3,205 and 7,630. In both of the images, the flow is from top to bottom. On the upper image of this figure (Re_D = 3,205), a single vortex filament, denoted as primary vortex, is captured while it is stretching around the cylinder and another one rolls up upstream of this vortex. In fact, recorded video for this flow configuration reveals an unsteady system such that a single vortex filament is formed, shed towards the cylinder, and then stretched. When Re_D is increased from 3,205 to 7,630, the coherency of the primary vortex filament is lost, and it breaks down to smaller scaled structures. The disorganization of these structures is consistent with the findings presented in Blackmore (2011) for Re_D = 10,000. Therefore, at the flow configuration with a turbulent approach boundary layer (λ = 2.5 and Re_D = 10,000) for the endplate with the sharp leading edge, combined analysis of the flow visualization results with the previous study by Blackmore (2011) shows a turbulent system of horseshoe vortices inhabiting breakdown of the primary vortex filaments onto small scale structures, consistent with the discussions of Baker and Greco on turbulent systems (Baker 1979, Greco 1990).

3.3.3. Selection of the endplate leading edge geometry

So far, the characteristics of the oncoming boundary layer along the endplates in absence of the cylinder, and features of the horseshoe vortex systems were discussed (in conjunction with the previous studies) in sections 3.2.1 and 3.2.2, respectively. In absence of the cylinder, the sharp leading edge leads to a flow separation/re-attachment, while the elliptical geometry of the endplate yields an attached flow at the tip (Blackmore 2011). The flow re-attachment around the sharp leading edge promotes boundary layer transition, and the boundary layer thickness exceeds the thickness encountered in absence of the endplate for the case where the tunnel wall constrains the cylinder.

At the cylinder front-to-endplate leading edge distance of $\lambda = 2.5D$, the cylinder/endplate junction flow exhibits a laminar system of horseshoe vortices for an elliptical leading edge, and a turbulent system for the sharp tip. Both of the vortex systems encountered within these junctions are unsteady. While the laminar system oscillates at a non-dimensional frequency of St = 0.86, the

turbulent system does not inhabit a dominant frequency but shows irregular oscillations. In the turbulent system, the vorticity supply into the single vortex is through disorganized structures as opposed to the feeding of vorticity within the boundary layer into a newly growing vortex in the laminar system. While the magnitude of vorticity for the primary vortices is similar in both laminar and turbulent systems, the size of the turbulent vortex is slightly larger than its laminar counterpart. In addition, the vorticity field in the turbulent case extends further away from the endplate wall along the wall normal direction compared to the laminar case. The ejection of low momentum fluid from the endplate surface, induced by the primary vortex, is also evident with the opposite signed vorticity and is more pronounced in the turbulent system (Blackmore 2011).

At this point, it is worthwhile to remember that the Karman instability in the wake of a circular cylinder (near its ends) is decoupled with the unsteady characteristics of the flow field at cylinder/wall junctions (Szepessy 1993, Baker 1979, Thomas 1987). However, the time-averaged flow features within the junction region is effective on the vortex shedding behind the cylinder. Therefore, the selection on the leading edge geometry is based on how the horseshoe vortex system affects the upstream time-averaged velocity field at the close proximity of the cylinder/endplate junction rather than their associated unsteady flow characteristics. Based on the analyses provided in the previous paragraph, it is understood that turbulent vortex system promotes mixing of the low momentum fluid close to the endplate wall with the high momentum fluid away from the wall as evident in the more pronounced secondary vortices. It also exhibits a larger vortex which oscillates in a smaller spatial interval, thus increases the time-averaged circulation near the wall compared to the laminar case. These findings encourage the selection of the endplate leading edge as the sharp geometry. Another supporting evidence for this decision comes from the study of Khoury (2012) who determined the probability density functions (PDF) for the vortex filament angles at Re_D = 10,000 employing endplates with both leading edge geometries at either side of the cylinder (Khoury 2012). His results for λ = 2.5 show that both of the endplates lead to vortex filament angles centered on a filament angle of zero. However, the elliptical endplate results in a broader PDF for the vortex filament angles, and a lower probability for parallel vortex filaments (filaments with zero angle). Therefore, the geometry to be used for the endplate leading edge is selected to be sharp for the remaining parts of this dissertation.

3.4. Effects of the Symmetry in the End Conditions on the Wake Quasi Two-Dimensionality

The effect of the variance in end conditions was studied by two groups for low Reynolds numbers. Slaouti and Gerrard (1981) studied various end constructions on the wake flow behind a circular cylinder for $60 \leq Re_D \leq 200$. They conclude that if the effect of one cylinder end was more dominant than the other end, then oblique vortex shedding is observed (Slaouti and Gerrard 1981). Miller and Williamson (1994) imposed various flow velocities near the cylinder ends for the manipulation of the vortex shedding mode by using suction tubes for $Re_D \leq 205$. They observed that the difference in the suction leads to oblique shedding.

As a first step in search of the degree of quasi two-dimensionality, the probability density function of the vortex filament angles and the velocity spectra obtained from the analyses of two simultaneous CTA signals are given as a function of Reynolds number in Figure 3.3. The first two columns from the left give the velocity spectra at each Reynolds numbers increasing from Re_D = 5,000 (top row) to Re_D = 30,000 (bottom row). The columns on the left and the middle give the autospectra of streamwise velocity signals for the asymmetrical case, denoted as *C1*, and the symmetrical case, denoted as *C2*, respectively. In each of these plots, the dashed and solid lines distinguish velocity spectra of different hot-film signals. The vertical and horizontal axes of these plots represent the normalized autospectral density, $S_u/S_{u,max}$, and Strouhal number, St, respectively. At the right column of this figure, probability density functions (PDF) for the vortex filament angles are given for each Reynolds number (increasing from top to bottom) and both asymmetrical (*C1*), and symmetrical cases (*C2*). For this column, the vertical and horizontal axes represent the probability value of the vortex filament angle, and the filament angle in degrees, respectively.

Initially, let's turn our attention to the left and middle columns, i.e. velocity spectra plots. The velocity spectra from both of the signals show the same predominant frequency, i.e. peaks of dashed and solid lines coincide at the same Strouhal number value, independent of Reynolds number. This result implies the absence of variance in the vortex shedding frequency along the span in the time-averaged sense under the following limitations; *(i)* within the experimental uncertainty bounds, given in Table 2.4, and *(ii)* within a spanwise extent $\pm 1.5D$ away from the cylinder mid-span.

On the other hand, the distribution of the vortex filament angles shows a variation as a function of time. The probability density functions (PDF), obtained from the time traces of vortex filament angles, have the shape of a Gaussian function centered around a mean value. This mean value (ϕ_{vf}) represents the filament angle most probable to be encountered within 1,200 vortex shedding cycles between two probe locations. It varies with the Reynolds number and the experimental configuration. The mean value of the filament angle (ϕ_{vf}) for the asymmetrical case, denoted as C1, is greater than or equal to the symmetrical case, denoted as C2, for all the Reynolds numbers. The difference in between the mean filament angle of the two cases is more pronounced for small Reynolds numbers; $5{,}000 \leq Re_D \leq 10{,}000$. One interesting and novel observation worth mentioning here is that the PDF curve for the smallest Reynolds number value investigated herein (Re_D = 5,000) has the narrowest band of filament angle (ϕ) values and the sharpest peak distribution; whereas, with an increase in Reynolds number, the broadness in the PDF distribution increases. This observation implies that as the Reynolds number increases, the variability of ϕ with time increases. If thought carefully this should be of no surprise to us since an increase in Reynolds number is expected to increase the intrinsically-developed turbulence in the shear layers and the wake, affecting the stability of the vortices. This result is in accord with the findings of Szepessy (1994) which shows that the probability density functions at Re_D = 43,000 is broad and centered on the mean value.

The most probable vortex filament angle (ϕ_{vf}) has been determined for all Reynolds numbers and experimental configurations in question of the present investigation, and are presented in Figure 3.4. The symmetrical end conditions lead to the filament angles between 2° to 3° (circular symbols), which represent more quasi two-dimensional vortex shedding compared to their counterparts for the asymmetrical case where filament angles vary between 3° to 8° (square symbols).

Having quantified the effects of the symmetry in end conditions, now we can focus on the comparison of the Strouhal numbers with the values obtained by previous researchers for similar Reynolds numbers. The predominant Strouhal number *St* values, determined from the spectra plots in Figure 3.3 (the middle column), are compared with those documented in the literature for varying Reynolds number. As can be seen in Figure 3.5, the Strouhal values are about 0.2 over the range of Re_D, and in good agreement with the previous literature (Norberg and Sunden 1987, Nebres 1992, Hover *et al.* 2001, Alam *et al.* 2010).

3.5. Chapter Conclusions

In this section, the effects of the endplate leading edge geometry on the horseshoe vortices are determined for two distinct tip geometries for Re_D = 10,000. As a reference case, the cylinder/tunnel wall junction is also studied in absence of the endplates. At λ = 2.5D, the cylinder/endplate junction exhibits a laminar and a turbulent system of horseshoe vortices when an elliptical and a sharp geometry is used as the endplate tip, respectively. The difference in these vortex systems is due to the boundary layer transition (upstream of the junction region) caused by the steady flow separation/re-attachment at the sharp endplate tip. While both the laminar and turbulent systems are unsteady, it is clear that the turbulent system promotes mixing of the low momentum fluid close to the endplate wall with the high momentum fluid away from the wall more than the laminar system. Therefore, the geometry to be used at the endplate tip is selected to be a sharp geometry as its effects are in accord with aforementioned techniques for the promotion of parallel vortex shedding in the wake of a circular cylinder.

In the final section of this chapter, the vortex shedding characteristics at two separate points in the wake are compared in order to quantify the effects of the symmetry of the cylinder end conditions on the wake flow for all the Reynolds numbers considered, i.e. $5{,}000 \leq Re_D \leq 30{,}000$. The geometry of the endplate leading edge is sharp and identical for all of the endplates. The symmetry in the end condition leads to smaller values in the most probable vortex filament angle (ϕ_{vf}), i.e. $2° \leq \phi_{vf} \leq 3°$, compared to the angles determined for the asymmetrical case, i.e. $3° \leq \phi_{vf} \leq 8°$, for the range of Reynolds numbers. Strouhal numbers obtained for the symmetrical case are also in good agreement with previous measurements of vortex shedding frequencies by other researchers.

During the investigation of the effects of a single, straight tripwire on the cylinder wake, the experimental setup has been decided to include two endplates with a sharp leading edge, one at each end of the cylinder, for all the Reynolds numbers.

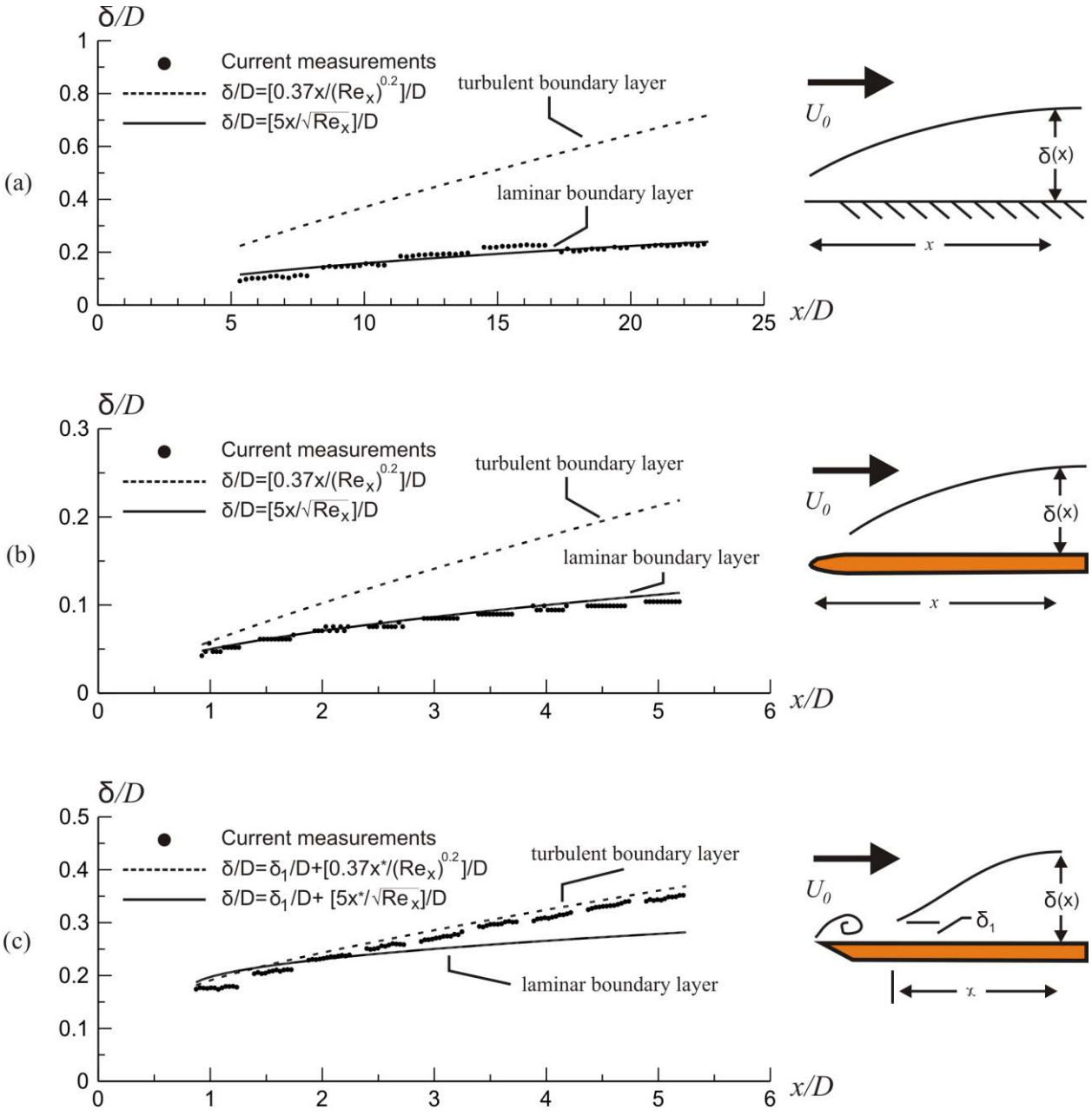

Figure 3.1 Variation of the boundary layer thickness along the wall for different experimental configurations in absence of cylinder. U_0 = 197 mm/s, D = 50.8 mm, (a) water tunnel wall, (b) endplate with an elliptical leading edge, (c) endplate with a sharp leading edge.

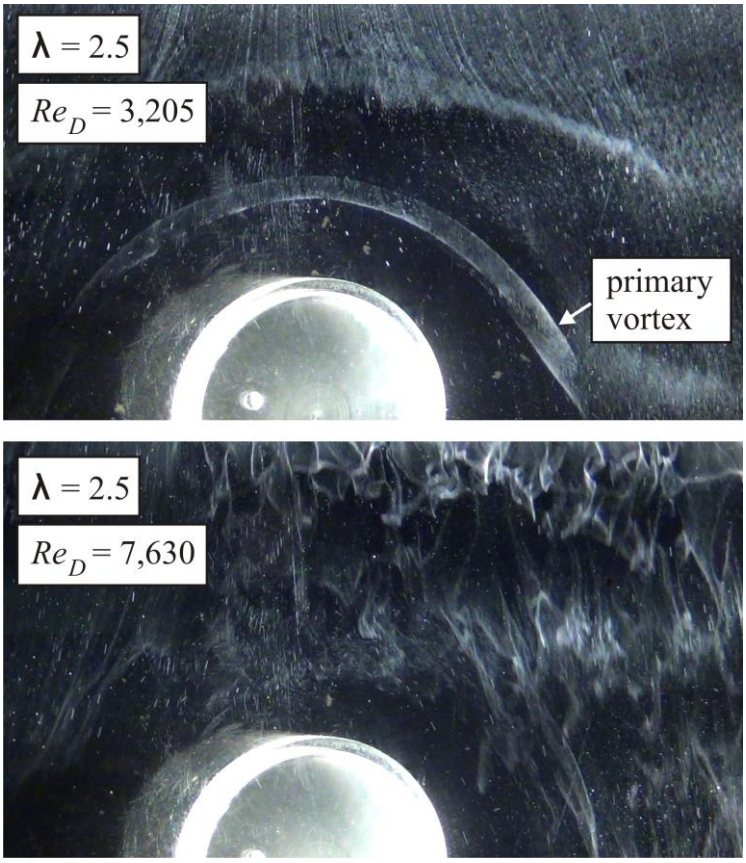

Figure 3.2 Hydrogen bubble flow visualization on a plane perpendicular to the cylinder span for Re_D = 3,205 and Re_D = 7,630 (both for λ = 2.5) in the cylinder/endplate junction with a sharp leading edge. Flow is from top to bottom.

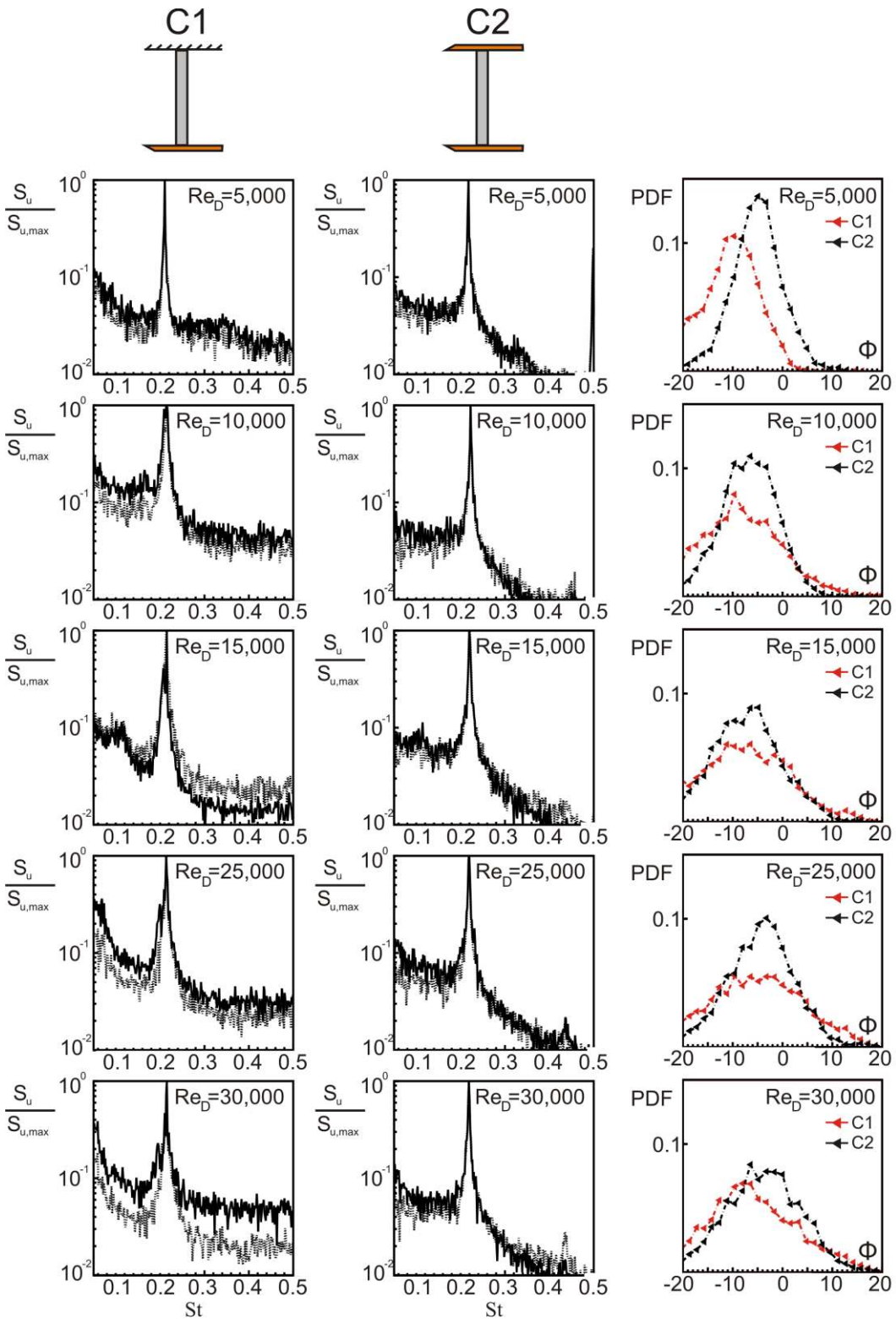

Figure 3.3 Velocity spectra from both hot-film signals for (i) asymmetrical case on the left column (C1), and (ii) symmetrical case in the middle column (C2), and probability density functions for the vortex filament angles for both experimental configurations (C1 and C2). Reynolds number increases from Re_D = 5,000 at the top to Re_D = 30,000 at the bottom.

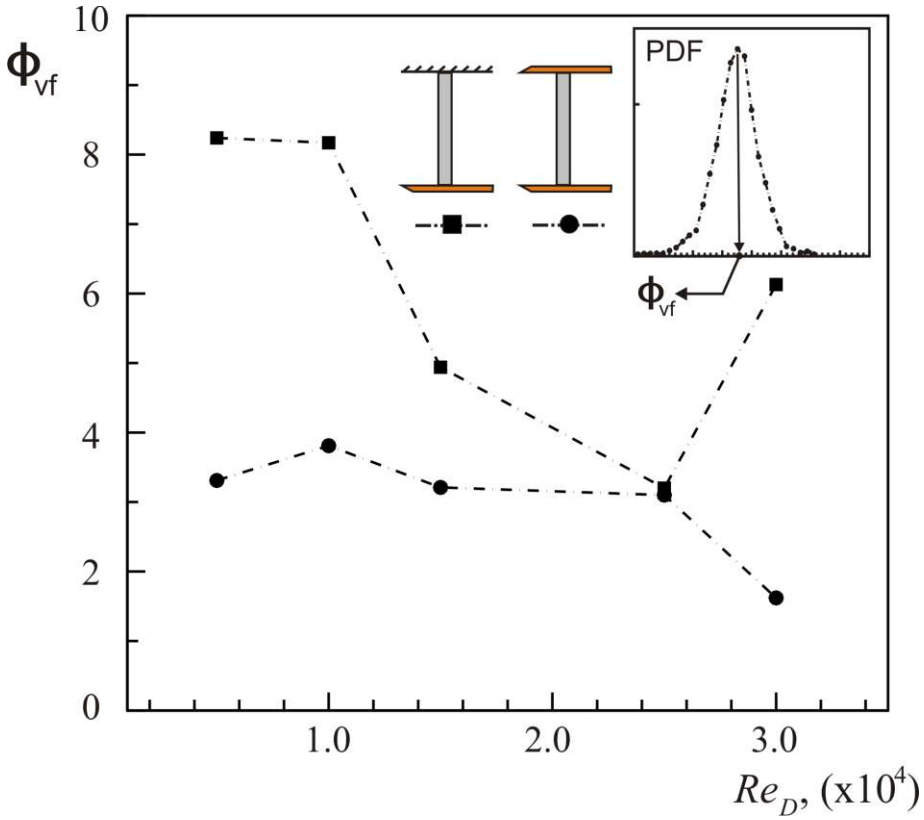

Figure 3.4 Most probable vortex filament angle, ϕ_{vf}, as a function of Reynolds number for asymmetrical (square symbols), and symmetrical (circular symbols) end conditions. Dashed line is for illustrative purposes only.

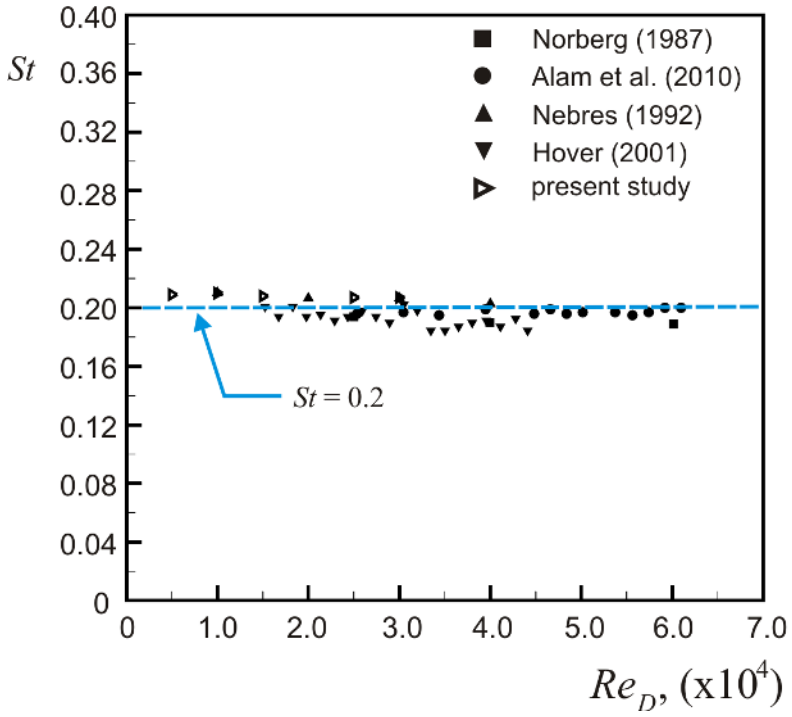

Figure 3.5 Variation of the Strouhal number (St) with Reynolds number (Re_D) for a smooth cylinder.

Chapter 4

Effects of a Single, Straight Wire on the Near Wake

This chapter presents the experimental results obtained by using Constant Temperature Anemometry (CTA), Particle Image Velocimetry (PIV) and hydrogen bubble flow visualization techniques in the flow around a circular cylinder fitted with a single, straight surface wire. Considering the unresolved issues on the application of a single surface wire on a circular cylinder, and the scope of this dissertation put forward in Chapter 1, the results will focus on: *(i)* the attenuation or amplification in Karman vortex shedding, *(ii)* relationship between different sets of critical wire angular locations, *(iii)* effects of Reynolds number and wire size on the critical flow states and wire angles, *(iv)* unsteady characteristics of the Karman vortex shedding, and *(v)* quantitative features of the wake flow structures.

The structure of the chapter is as follows. Initially, the scale of the surface protrusions is determined since small-scale wires are shown to be ineffective on promoting attenuation or amplification in Karman vortex shedding at critical wire locations (Ekmekci and Rockwell 2011). The following section focuses on the cylinder fitted with the tripwire having a wire-to-cylinder diameter ratio of d/D = 0.029, at a Reynolds number of Re_D = 10,000 for the comparison of the current results with the previous findings of Ekmekci (2006), and Ekmekci and Rockwell (2010). This will be followed by the effects of the wire size and Reynolds number on the wake flow response to the surface wire. Then, temporal variations in strength and coherence of the Karman instability at critical wire locations will be evaluated via the use of qualitative flow visualization and hot-film investigation. Quantitative features of the near-wake and shear-layer regions, sampled by PIV, will be given for two cases; *(i)* low-Reynolds number (Re_D = 10,000), and *(ii)* high-Reynolds number (Re_D = 25,000) at a constant wire size of d/D = 0.059. After characterizing various aspects of attenuation or amplification of the Karman shedding and the general flow structures, another section is devoted for the discussion of the relationship between the critical flow states and the critical wire angles defined by Nebres and Batill (1993), and Ekmekci and Rockwell (2010). In the final section, the findings of the current chapter will be summarized.

4.1. Scale of the Tripwires

The variation of the thickness of the laminar boundary layer (δ/D) forming around a smooth cylinder at Re_D = 5,000 (which is the lowest Reynolds number investigated in this study) was estimated based on the Blasius method described by Schlichting (1968) with the aim of quantifying the relative scale of the surface wires. This method required the knowledge of the surface pressure distribution around the cylinder, as detailed in App. C. To this end, a pressure port was opened on the surface of a smooth cylinder of equivalent diameter at its mid-span and a Setra model pressure sensor was connected to this pressure port. Rotating the cylinder around its axis, the location of the port was varied from θ = 10° to 75° at 5° increments, and at each angular location, surface pressure data was collected at 100 Hz acquisition rate for a duration of 10 seconds. The plot provided in Figure 4.1 clearly shows that at Re_D = 5,000 (and thereby, of course, at higher Re_D values), the surface wires considered in this investigation are larger than the boundary-layer thickness at all circumferential locations between θ = 10° to 75°. It was, therefore, concluded that all the wires used in this study are large-scale wires.

4.2. A Comparison with Previous Findings and Furthering of the Understanding at Critical States

In what follows, focus will be on the spectral nature of the streamwise velocity signals obtained from CTA measurements conducted at a point in close proximity to the cylinder wake. During these endeavors, comparisons with the findings of the previous studies will be made and an elaborated look into the wire induced critical effects will be presented.

Let's start with the scenario where the wire diameter was 2.9% of the cylinder diameter and the flow Reynolds number was 10,000 for the comparison of the current findings with the previously reported flow conditions by Ekmekci and Rockwell (2010, 2011). In Figure 4.2(a), autospectral density S_u of the streamwise velocity signals, obtained from CTA measurements, are provided for this case at selected wire locations, θ. As discussed in Ekmekci and Rockwell (2010), the amplitude of the spectral peak $S_u(f_K)$ (which occurs at the characteristic Karman frequency f_K) can be viewed as an indirect indicator of the coherence and strength of Karman vortex shedding. It is clear from Figure 4.2(a) that the peak amplitude in velocity spectra becomes significantly attenuated or amplified for certain locations of the wire in comparison to the reference case (θ = 180° wire location). To depict the overall picture, the amplitude of this peak (i.e., $S_u(f_K)$) is plotted against

the wire angle from $\theta = 0°$ to 180° in Figure 4.2(b). The wire locations that have a critical impact on the strength of the Karman instability can be deduced from considerations of Figure 4.2(a) and 4.2(b). It can be seen that the most substantial variation in the peak spectral amplitude $S_u(f_K)$ occurs when the wire is located within a certain range of angular positions. This range is marked as $\Delta\theta$ in Figure 4.2(b). As the wire angular location θ is increased starting from 0°, amplitude in spectral peak $S_u(f_K)$ remains relatively uninfluenced till this range of angles is reached. Then, between 43° to 48°, the peak amplitude $S_u(f_K)$ gradually drops to significantly low values. Given that the most attenuated $S_u(f_K)$ occurs at $\theta = 48°$, this location can be distinguished as the first critical angle θ_{c1}, in accord with the designation made previously by Ekmekci (2006) and Ekmekci and Rockwell (2010). After $\theta_{c1} = 48°$, as the wire angular location θ is increased further, the peak spectral amplitude shows a gradual increase, attaining the highest levels over a range of wire locations in the vicinity of $\theta = 63°$. These locations are marked in Figure 4.2(b). Consequently, here, rather than a single θ value, a range of angles near 63° are identified as the second critical locations θ_{c2} on the cylinder surface. Past the θ_{c2} range, a further increase in θ results in a gradual decrease of the peak spectral amplitude to the levels encountered between $\theta = 108°$ to 180°, where the wire (being at the base region) shows no detectable influence on the strength of the Karman instability.

Another interesting observation involves the frequency at which the spectral peak appears. This frequency is indeed the predominant frequency of velocity fluctuations associated with the shedding of Karman vortices. Its value is indicated in terms of Strouhal number (St) and plotted in Figure 4.2(c) against the wire angular location θ from $\theta = 0°$ to 180°. It can be seen from this St-θ plot that the surface wire affects the value of St only when it is deployed over a certain range of locations (marked by $\Delta\theta$), while outside of this range, no significant effect is detectable. Two characteristics are prominent: there is *(i)* a crater-like St variation over the angular range $\Delta\theta$, and *(ii)* a slight rise in St at the beginning and end of this crater-like change. These observations from Figure 4.2(c) are in perfect agreement with those of Nebres and Batill (1993) and Ekmekci and Rockwell (2010).

When the CTA findings of the present study in Figure 4.2 are compared with the previously published PIV findings of Ekmekci and Rockwell (2010, 2011), one can identify notable differences in the exact values of the critical wire locations such that: *(i)* the first critical location reported by Ekmekci and Rockwell has a value higher than that found in the present study (i.e., θ_{c1} was determined to be 55° by Ekmekci and Rockwell, whereas it is 48° in the present), and *(ii)* as

the second critical location, Ekmekci and Rockwell provided a single location θ_{c2} = 65° on the cylinder surface; while, in the present investigation, a range of locations in the vicinity of 63° are found to amplify the spectral peak and, therefore, that range of angles is identified as the second critical location θ_{c2} for wire application. These differences can be attributed to a number of reasons: First of all, the water channels were different between the two studies. Dissimilar free-stream turbulence levels in the two facilities may affect the critical location θ_{c1}. Secondly, although in both studies the angular positions, θ, on the cylinder surface was defined referencing the forward stagnation point, the way they determine the zero reference was different. In the earlier studies of Ekmekci and Rockwell (2010, 2011), the stagnation point was found merely through visual inspection and therefore approximately ±4° human error is estimated in their determination of the stagnation point position. This corresponds to a very-easily-doable ±1.8 mm wire-positioning error on the circumferential surface of the cylinder. In the present study, however, the exact location of the reference zero angle (the forward stagnation point) was determined from the distinctiveness of the θ_{c1} location in both the positive and negative angular directions as this critical location has very discernible characteristics in both $S_u(f_K)$-θ and St-θ variations. Also, Ekmekci and Rockwell (2010) studied θ variation in coarser (5°) increments, while the present study selected the θ increments of wire placement to be 1° to 2° especially near the critical states to increase accuracy in the determination of the critical places. Therefore, the critical locations determined through the present CTA measurements are more accurate (within 1° to 2°).

Unlike the PIV findings in Ekmekci and Rockwell (2010), it can also be noted in Figure 4.2(a) that, at the first critical angle θ_{c1}, the velocity spectrum formed using the CTA data does not show a pronounced low-frequency peak. This should, in fact, be expected because the low-frequency velocity fluctuations (associated with the bistable oscillations of the shear layer) were detected only toward the separation region close to the wire (Ekmekci and Rockwell 2010). Herein, the location of the CTA probe (4.3D downstream and 3D lateral from the cylinder center) is far away from the separation region in the vicinity of the wire and, therefore, the CTA data cannot detect the low frequencies associated with the bistable shear-layer oscillations reported previously by Ekmekci (2006) and Ekmekci and Rockwell (2010).

Taken overall, it follows from all the foregoing that the CTA data can easily detect the attenuation or amplification in Karman instability, it can be used as a means to determine the critical locations

for wire application on a cylinder. In what follows, we will use CTA to question the effect of the wire size on the locations of the critical angles discussed in this section.

4.3. Effect of the Wire Size

To study the effect of the wire size, CTA measurements have been conducted for cylinders fitted with different-size wires. The diameters of these wires were 2.9, 3.9 and 5.9% of the cylinder diameter. During this phase of the investigation, the Reynolds number was fixed at Re_D = 10,000 and the angular location of the wire was changed from $\theta = 0°$ to 180°. It is known from Figure 4.1 that the wires under consideration here are larger than the boundary-layer thickness (i.e., they are large-scale wires). In Figure 4.3, the streamwise velocity spectra S_u, calculated from the CTA data, are given at selected wire locations, and in Figure 4.4, the overall variation of the spectral amplitudes at Karman frequency $S_u(f_K)$ and the Strouhal number St are provided as a function of the wire angle from θ = 0° to θ = 180° for all three different-size wires. From left to right, the results are presented for d/D = 0.029, 0.039 and 0.059, respectively. Figures 4.3 and 4.4 clearly show that all three wires induce similar effects on the velocity spectra and shedding frequency. The effect of the wire is most notably perceived if it is deployed over a range of angular positions ($\Delta\theta$) on the cylinder surface. It can be seen that this range of angles ($\Delta\theta$) increases with the increasing size of the wire ($\Delta\theta$ = 60°, 65° and 75° for d/D = 0.029, 0.039 and 0.059, respectively). For each wire, a critical location θ_{c1} that leads to the most attenuated spectral amplitude associated with the Karman instability $S_u(f_K)$, and a range of critical locations θ_{c2} that brings the spectral amplitude to peak levels can be identified. From here, one can conclude that attenuation and enhancement in the strength and the coherence of the Karman instability can be achieved by large-scale straight wires of different diameter. Interestingly, although the range of θ_{c2} locations is generally unchanged, the θ_{c1} location is found to vary with the wire size. According to the spectral results presented in Figures 4.3 and 4.4, θ_{c1} is found to be 48° for d/D = 0.029, 47° for d/D = 0.039 and 43° for d/D = 0.059. Hence, as the surface wire gets larger, the angular value of the critical wire location that attains the largest attenuation in Karman instability (i.e., θ_{c1}) becomes smaller, which is consistent with Ekmekci and Rockwell (2011).

For all the wires investigated, the Strouhal number of the Karman vortex shedding exhibits the same characteristic variation with the wire location (see the St-θ plots in the bottom row of Figure 4.4). That is, within the range of effective wire locations ($\Delta\theta$), as the wire angular position θ

increases, Strouhal number undergoes a crater-like distribution, characterized by a gradual decrease followed by a gradual increase, and at both the beginning and end of this crater-like change, *St* generally is larger than the reference *St* value (which is observed outside of the range of effective wire locations $\Delta\theta$). An interesting observation, also consistent with the findings of Nebres and Batill (1993), is that the overshoot at the beginning of the crater-like distribution increases with the increasing wire size; $St = 0.215$ for $d/D = 0.029$, $St = 0.221$for $d/D = 0.039$, and $St = 0.235$ for $d/D = 0.059$. On the other hand, the minimum value of vortex shedding frequency is rather constant at $St = 0.175$, 0.168, and 0.168 for d/D=0.029, 0.039, and 0.059 respectively. The angular values of wire locations at which the minimum Strouhal number is achieved lie within a range of wire angles centered around $\theta = 70°$ for all of the wires and are consistent with the findings presented in Nebres (1992), and Nebres and Batill (1993).

Comparing the top- and bottom-row plots of Figure 4.4 suggests an inverse relationship between the distribution of the spectral amplitudes at Karman frequency $S_u(f_K)$and the variation of Strouhal number over the range of effective wire angular locations ($\Delta\theta$). The general trend is that as $S_u(f_K)$ decreases with a change in θ, *St* shows an increase, and vice-versa. However, it should be emphasized that what is being mentioned here is a somewhat superficial association. For example, θ_{c1}, which is the critical location where placing the wire attenuates the spectral amplitude the most, does not coincide with the wire location where *St* makes a peak. In addition, it should be noted that the angular location where *St* reaches its minimum value (around $\theta \approx 66°$-$70°$) does not correspond to the wire angle with the most amplified vortex shedding, i.e. $\theta_{c2} = 50°$-$65°$.

4.4. Effect of Reynolds Number

Now, the effect of the Reynolds number is presented in order to study whether the critical wire locations can still be detected at Reynolds numbers other than 10,000, and if so, how the Reynolds number affects these locations. Consideration is given to a Reynolds number range from Re_D = 5,000 to 30,000. For the sake of brevity, in this section, the spectral results will be discussed only for one of the wire sizes (largest wire size considered in this study with $d/D = 0.059$). Yet, it should be noted that the conclusions drawn regarding the Reynolds number effect were common to all three wire sizes of this study.

For the cylinder with this large-scale spanwise wire, Figure 4.5 shows the autospectral density S_u of the streamwise velocity fluctuations, determined through the CTA measurements, for Re_D =

5,000 in the first column to Re_D = 30,000 in the fifth column. For all the Reynolds numbers investigated herein, a critical wire location leading to the most significant attenuation in the spectral amplitude at the Karman frequency is encountered. The second row in Figure 4.5 presents the spectra at this wire angle for each Re_D. The values of this critical wire angle, θ_{c1}, are 42° and 43° for Re_D = 5,000 and 10,000, respectively. On the other hand, for 15,000 ≤ Re_D ≤ 30,000, it remains constant at θ_{c1} = 46°. After this critical position (θ_{c1}) of the wire, as the value of θ is increased, the spectral amplitude increases, eventually resulting in the highest spectral peak at the range of the second critical angles, θ_{c2}. Similar to the results given in Figure 4.3, the velocity spectra associated with the most amplified Karman shedding is given in the third and fourth rows of Figure 4.5 for each Re_D. The location of the second critical angle represents a range of angular locations of the wire, 50° ≤ θ_{c2} ≤ 70° as can be seen from Figure 4.5, and is generally not affected by the changes in Reynolds number. Past the second critical angle θ_{c2}, as θ is increased, the spectral amplitude of the Karman instability gradually decreases to moderate levels, as observed at θ = 180°. At this point, one can conclude that the critical angular locations θ_{c1} and θ_{c2} exist for all the subcritical Reynolds numbers studied herein.

St-θ variations, given in the bottom row of Figure 4.6, once again show the same characteristic distribution over the angular range (marked as $\Delta\theta$) for all the Reynolds numbers under consideration. That is, a crater-like variation is observed and the value of *St* rises towards the beginning and end of this variation, which is consistent with previous studies by Nebres (1992), Nebres and Batill (1993), Ekmekci (2006), Ekmekci and Rockwell (2010). One can see that the range of the wire angles ($\Delta\theta$) where the wire is leads to variations in *St* increases with the Reynolds number. Such that, $\Delta\theta$ = 75°, 90°, 83°, 86°, 85° in the order of increasing Reynolds number from Re_D = 5,000 to 30,000. Furthermore, the peak in *St* at the beginning of the crater-like variation also generally shows an increase with Reynolds number. That is, St = 0.214, 0.235, 0.251, 0.253, 0.253 in the order of increasing Re_D. The influences of the Reynolds number in the *St*-θ variation are also completely consistent with the previous studies of Nebres (1992) and Nebres and Batill (1993).

Another understanding from Figure 4.6 is the relationship between the vortex shedding frequency, *St*, and the coherency of the Karman vortex shedding $S_u(f_K)$. For all Reynolds numbers in question, the distributions of these two quantities are related to each other as explained previously for Figure 4.4. That is, roughly speaking, the strength of Karman vortex shedding $S_u(f_K)$ decreases as *St* increases, and vice versa. Again, the angular wire location at which maximum *St* is achieved does

not coincide with the wire location where the vortex shedding strength reaches its minimum, θ_{c1}, and the angular location of the minimum *St* (around $\theta \approx 66°$-$70°$) does not correspond to the most amplified vortex shedding, i.e. $\theta_{c2} = 50°$-$65°$.

Interestingly, the values for the first critical angle, θ_{c1}, show a dependency on the wire size and Reynolds number as discussed above. In order to demonstrate the general trend in the location of θ_{c1}, the distribution of its angular locations are given in Figure 4.7 for all the wire sizes tested as a function of Reynolds number. For the Reynolds number range investigated here, it is evident from this plot that, for any given wire size, the θ_{c1} location increases with an increase in Reynolds number up until Re_D = 15,000, and above this Reynolds number value, it remains unaffected by the Reynolds number changes and becomes only a function of the wire size. On the other hand, an increase in the wire size at a constant Reynolds number results in a decrease in the angular location of θ_{c1} for all the Reynolds numbers.

4.5. Unsteady Characteristics of the Near-Wake

After presenting the effects of the Reynolds number and wire size on the spectral and vortex shedding characteristics of flow past a circular cylinder fitted with a single large-scale wire in the foregoing, the unsteady characteristics of the near-wake are examined in this section. As a first step, it is worthwhile to compare CTA velocity signals for different locations of the surface wire. To this end, in Figure 4.8, time traces of the streamwise velocity component are given at selected wire angles for a representative case where the Reynolds number is Re_D = 10,000 and wire diameter is $d = 0.059D$. The presented signals, whose velocity spectra were previously given in the third column of Figure 4.3, clearly show that the velocity fluctuations lose their ordered periodicity, exhibiting large irregularities at the first critical angle θ_{c1}, i.e. $\theta = 43°$, compared to the velocity signals at other angular locations of the wire. On the other hand, the signals at θ_{c2}, i.e. $\theta = 56$ and $70°$, show an increased amplitude of fluctuations compared to the reference case. These observations are consistent with the work by Ekmekci and Rockwell (2010, 2011) which previously reported a similar characteristic for a different wire size at the same Reynolds number ($d/D = 0.029$ and Re_D = 10,000).

The use of the hydrogen bubble technique in the present study provided new visual insights into the critical wire effects. Let's now turn our attention to these visualization tests and discuss the key findings. In Figure 4.9, representative hydrogen bubble images are provided for the case where the

Reynolds number is Re_D = 10,000 and the wire diameter is $d = 0.059D$. From the left column to the right, the streakline images in this figure correspond to θ_{c1}, θ_{c2} and 180° wire locations, respectively.

For the θ_{c1} location, the video recording of the hydrogen-bubble patterns revealed an interesting phenomenon: there exist times with no rhythmic development of Karman vortex clusters and times during which the regular formation of Karman vortices resumes for no more than a couple of shedding cycles. Notice that the first column of Figure 4.9 shows two streakline images. The top image (Fig 4.9a) depicts a representative snapshot from the no-shedding phase of the flow and the bottom image (Figure 4.9b) shows a snapshot from the regular shedding phase. During the entire visualization duration (over 1-minute long), switching between these two flow modes is observed to occur many times over and over again, the ceasing of the regular shedding mode dominating the majority of the time. Highly irregular velocity signals (in Figure 4.8) and the significant reduction observed in the peak spectral amplitude (in Figure 4.3) when the wire is placed at this critical location (θ_{c1}) make complete sense under these observations. Previously in Ekmekci and Rockwell (2010), the short-time movie (lasting for 13.3-s long) of PIV images also showed the attenuation phase of the Karman vortex shedding for the θ_{c1} wire location for d/D = 0.029 and Re_D = 10,000. This animation is available online in Ekmekci and Rockwell (2010). However, the resumption phase of the regular Karman shedding (mostly lasting for a couple of shedding cycles) is a new observation revealed here thanks to the longer-time records of hydrogen-bubble images.

As for the θ_{c2} wire location, coherent formations of large-scale Karman vortices were evident from the video recording of the hydrogen-bubble patterns. For this wire location, particularly the oscillations in the separating shear layers and the vortex clusters appeared much more pronounced compared to the reference scenario (θ = 180° wire location). This observation also correlates well with the relatively enhanced spectral peak, seen earlier in Figure 4.3 for the θ_{c2} location.

The hydrogen bubble visualization study brings another interesting understanding to the fore. To see this, the reader can inspect the streamwise length of the near-wake bubble on the snapshots provided in Figure 4.9. For the first critical wire location θ_{c1}, the near-wake bubble extends significantly in the streamwise direction during the phase when the Karman vortex shedding is disrupted (Figure 4.9a). On the other hand, for this same critical location, during the phase when the Karman vortex shedding resumes (Figure 4.9b), the streamwise extent of the near-wake bubble becomes analogous to that of the reference scenario (θ = 180° wire location, given in Figure 4.9d).

These observations explain why maximum near-wake extension was a distinguishing feature for the θ_{c1} wire location in time-averaged patterns (Ekmekci and Rockwell 2010). As for the second critical wire location, it can be seen that the bubble length is extremely contracted. This observation is also consistent with the significant near-wake contraction reported previously for having the wire at a θ_{c2} location in the time-averaged results (Ekmekci and Rockwell 2010).

The velocity spectra presented in the foregoing (in Figures 4.2 to 4.6) were generated using the classical Fourier analysis, which merely yields the time-averaged spectral properties. Thus, these results cannot reflect any time-dependent spectral changes. For example, for the θ_{c1} wire location, the switching between the no-shedding and regular-shedding modes, as observed in the hydrogen bubble images (Figure 4.9), cannot be quantified on the time-averaged velocity spectra; all we can see is remarkably reduced peak spectral amplitude. In order to study whether the dominant frequency of velocity fluctuations undergoes a change in time, time-frequency analyses were performed by applying short-time Fourier transformation (STFT) to the streamwise velocity signals determined through CTA for varying wire locations. In Figure 4.10, time-frequency spectrograms, determined via STFT, are presented for selected wire angles for a representative case where the Reynolds number is Re_D = 10,000 and the wire diameter is $d = 0.059D$. These spectrograms are built by stacking the sequence of velocity spectra in time and indicating the amplitude of the autospectral density as a contour map. The horizontal axis shows the time, the vertical axes shows the non-dimensional frequency (the Strouhal number St), and the amplitude of the spectral density at a particular frequency and a particular time is represented by grayscale colors. In order to explore the intermittency of the dominant frequency, in these plots, the spectra at every window of time is normalized with its maximum (i.e, $S_u/S_{u,max}$). The color coding of the grayscale is such that the white regions mark the maximum spectral amplitude at a given time. In Figure 4.10, next to each time-frequency spectrogram, the corresponding (regular, time-averaged) velocity spectrum is also presented with its St axis aligned with the vertical axis of the spectrogram. As would be expected, the uncertainty for the St value in STFT results was much higher than that in the classical FFT results ($\pm$0.014 and $\pm$0.003, respectively). This leads to slight differences in the dominant frequencies determined by the two methods. Before we start discussing the results of the spectrogram analysis, it should be emphasized that similar time-frequency variations were also detected for other Reynolds numbers and wire diameters. Therefore, the conclusions drawn

below for the particular Reynolds number and wire size in question are representative of the general picture.

Initially, let's focus on the second, fourth and the fifth rows of Figure 4.10 for a discussion on the time dependence of the vortex shedding at the critical angles, θ_{c1} and θ_{c2}, and the wire angle of θ = 180° for the reference case. When the wire is located at the first critical angle, $\theta = \theta_{c1}$, the predominant frequency based on STFT analysis, i.e. white iso-contours of $S_u/S_{u,max}$, is observed to scatter between $0.05 \leq St \leq 0.3$. This time-varying nature of the dominant frequency can be attributed to the intermittent switching between the no-shedding and shedding modes, observed during the aforementioned hydrogen bubble tests, and leads to the lower-amplitude, broad spectral peak in the (time-averaged) velocity spectrum compared to the velocity spectrum of the reference case (θ = 180°, given in the fifth row). As for the θ_{c2} location, the dominant frequency about which the spectral energy is concentrated generally appears to be independent of the time. Once again, this observation is consistent with the large-amplitude peak observed in the (time-averaged) velocity spectrum (given next to the spectrogram plot) and the persistent shedding of the Karman vortices seen in the flow visualization results for this location of the wire.

After seeing that the regular shedding of Karman vortices from a cylinder gets interrupted for the majority of the time by the effect of a spanwise wire at θ_{c1} location, one question comes to mind: can this critical effect still be observed if the wire is placed not necessarily at θ_{c1} but at a location in close proximity? In pursuit of an answer, the time-frequency spectrogram and the (time-averaged) spectrum of the CTA signals were inspected for locations near θ_{c1}. In the first and third rows of Figure 4.10, findings are presented for θ_{c1} - 2° and θ_{c1} + 2°, respectively. As can be seen from both spectrogram plots, throughout the duration examined, the dominant frequency, where the spectral energy is concentrated, generally appears to be independent of time. Distinctive peaks observed in the (time-averaged) velocity spectra, given next to the spectrogram plots, also point out the mostly periodic aspect of the Karman vortex shedding for both θ_{c1} - 2° and θ_{c1} + 2°. However, this phenomenon is not investigated for the wire locations that are closer to θ_{c1} (e.g. θ_{c1} - 1° and θ_{c1} + 1°). Nevertheless, the peak spectral amplitude at θ_{c1} - 2° is somewhat lower and broader compared to both the reference case of θ = 180° and the case of θ_{c1} + 2°, indicating a relatively lessened coherence in Karman shedding for the θ_{c1} - 2° wire location. The corresponding flow visualization results (not shown here) also verify these observations at θ_{c1} - 2° and θ_{c1} + 2°.

For Re_D = 10,000 and d/D = 0.059, at the first critical wire angle $\theta = \theta_{c1}$, the duration of vortex shedding is found to be 43% of the whole duration of the data examined, which is given at the second row of Figure 4.10. As a last point, one can question how the percentage of the time where the regular Karman shedding occurs changes for different wire sizes and Reynolds numbers. Identical STFT analyses have been run at the first critical angle for other wire sizes and Reynolds numbers in question of this study and the ratio of the time when Karman shedding resumes to the total data recording time is given in Table 4.1 for each case. It can be seen that the percentage of the time during which the vortex shedding occurs at this first critical angle scatter around values lower than 50% for the majority of the cases.

Table 4.1 Percentage of the time during which Karman vortex shedding occurs at the first critical angle (θ_{c1}) for different wire sizes and Reynolds numbers

	Re_D = 5,000	Re_D = 10,000	Re_D = 15,000	Re_D = 25,000	Re_D = 30,000
d/D = 0.029	57	35	48	63	58
d/D = 0.039	39	38	34	33	23
d/D = 0.059	54	43	76	25	31

4.6. Quantitative Features of the Near-Wake and Shear-Layer

So far, the effects of the large-scale tripwire on the flow past a circular cylinder are discussed for different wire-to-cylinder diameter ratios ($0.029 \leq d/D \leq 0.059$) at a sub-critical Reynolds number range of $5{,}000 \leq Re_D \leq 30{,}000$ based on CTA data and hydrogen bubble flow visualization. The results show how the spectral and vortex shedding characteristics change at the critical angular locations of the large-scale wire, denoted as θ_{c1} and θ_{c2} in accord with the literature, at each wire size and Reynolds number. Furthermore, the effects of the Reynolds number and the wire size on these critical angular locations have been identified. Lastly, the unsteady characteristics of Karman vortex shedding at these critical wire locations have been explored with the use of a time-frequency analysis, and the flow visualization. These findings are considered to be novel in this study. However, quantitative information on how the flow features, other than Strouhal number and the strength of Karman vortex shedding, change at these critical wire angles is not addressed, yet. In the literature, such an investigation is previously reported by Ekmekci (2006), and Ekmekci and Rockwell (2010) with the use of PIV measurements of the flow field for a wire-to-cylinder diameter ratio of d/D = 0.029 at a Reynolds number of Re_D = 10,000. Nebres (1992) and Nebres and Batill (1993) also present quantitative information on shear layer spacing and longitudinal

vortex spacing based on their CTA data for a wire-to-cylinder diameter ratio of d/D = 0.089 at a Reynolds number of Re_D = 30,000.

In this section, the flow features are investigated in presence of the largest wire size in this study (d/D = 0.059) initially at a low Reynolds number case (Re_D = 10,000) and, then, at a high Reynolds number case (Re_D = 25,000) in order to explore the changes in the flow structures and reveal the degree of the consistency in the observed patterns with the existing literature. The results presented in these sections (4.6.1. and 4.6.2) are first linked to the CTA data, then further insight on the flow structures is given.

4.6.1. Low Reynolds number case; Re_D = 10,000

4.6.1.1. Spectral features of velocity signals

As a starting point, the variation of the predominant Strouhal number, St, and the spectral amplitude of the velocity fluctuations at the Karman shedding frequency, $S_u(f_K)$, are given as a function of the wire angular location in Figure 4.11. Therein, the values of St and $S_u(f_K)$ obtained from both the CTA and PIV measurements are provided. As the wire angle θ is increased, Strouhal number starts increasing at around the wire location of θ = 32° and reaches its maximum value of St = 0.235 at θ = 42°, according to the CTA data. Based on the velocity signal sampled with PIV at a location of x/D = 2.5 and y/D = 1.25, St reaches a maximum value of 0.24 at the same angular location (θ = 42°). After this θ, both the CTA and PIV data show that an increase of about 1° to 2° in θ results in a drastic decrease of the St value to around 0.18. As the wire location θ is increased further, St shows a decrease and then a gradual increase (i.e., a crater-like trend). After the wire location of θ = 115°, the wire has no effect on the shedding frequency. While the St-θ plots show a similar trend for both of the data sets obtained with CTA and PIV, minor discrepancies exist in the exact values of St. This discrepancy can be attributed to the respective uncertainty levels associated with the measurement techniques used. This uncertainty can be quantified based on the *Root-Sum-Square* equation, whose details can be found in App. A.1. It is found that the uncertainty in St is ΔSt_{PIV} = 0.0108 for the PIV data and ΔSt_{CTA} = 0.0041 for the CTA data.

The variation of the spectral amplitude at the predominant Karman frequency, $S_u(f_K)$, with the wire angular location, θ, determined from the CTA and PIV measurements, is also provided in Figure 4.11 (the bottom plot). The variations of St-θ and $S_u(f_K)$-θ plots are, roughly speaking, inversely related as explained in previous sections. This can also be observed from a comparison of the top

and bottom plots in Figure 4.11. As discussed in Ekmekci and Rockwell (2010), the amplitude of the spectral peak, $S_u(f_K)$, can be viewed as an indirect indicator of the coherence and strength of the Karman vortex shedding. $S_u(f_K)$ and thereby the coherence in Karman vortex shedding decreases between the wire angles $\theta = 32°$ to 43° while *St* increases. At the first critical wire angle ($\theta_{c1} = 43°$), $S_u(f_K)$ reduces in amplitude to about 40% of the reference case ($\theta = 180°$). This angular location, where the strength of Karman instability makes a minimum, marked as θ_{c1}, is in accord with the designation made previously by Ekmekci (2006) and Ekmekci and Rockwell (2010). As the wire angle, θ, is increased further, *St* shows a decrease (as indicated above) while the spectral amplitude, $S_u(f_K)$, gradually increases. The $S_u(f_K)$ reaches its maximum values at wire angular locations between the range of $\theta = 50°$ to 70°. This range is marked as θ_{c2} in Figure 4.11, again in accord with the definition made by Ekmekci and Rockwell (2010). Past these wire locations, the shedding starts to lose its amplified strength and the associated spectral amplitude gradually drops back to the levels encountered at the cases with no significant wire influence (i.e., for $\theta \geq 115°$).

It is clear from what has been presented so far that the coherence and strength of the Karman instability gradually attenuates as the wire location is increased from $\theta = 39°$ to $\theta = 43°$ reaching its minimum strength and coherency at $\theta = 43°$, whereas it is amplified between $55° \leq \theta \leq 70°$. From the evidence presented in Figure 4.11, the first and the second critical angles defined by Ekmekci and Rockwell (2010) are confirmed in PIV data to be $\theta_{c1} = 43°$, and $\theta_{c2} = 50°$ to 70° for $Re_D = 10{,}000$ and $d/D = 0.059$.

4.6.1.2. Time-averaged near-wake and shear-layer structures

In Figure 4.12, the time-averaged patterns of the normalized streamwise velocity $\langle u \rangle / U_o$, streamlines $\langle \psi \rangle$, absolute normalized vorticity $|\langle \omega \rangle D/U_o|$ are provided along with the contour patterns of the spectral amplitude at Karman frequency $S_u(f_K)$ in the first through last columns, respectively. In each row of this figure, the wire is at a different angular location θ, namely at $\theta_{c1} = 43°$, $\theta_{c2} = 55°$, $\theta_{c2} = 70°$, $\theta = 115°$, and $\theta = 180°$ from first row to the last, respectively.

The dashed contour lines of the streamwise velocity component, given in the first column in Figure 4.12, shows negative valued streamwise velocity and hence the reverse flow region. The streamwise extent of the near-wake bubble can be evaluated from a comparison of these pockets of negative $\langle u \rangle / U_o$ contours in Figure 4.12. It can be observed that the near wake extends the most when the wire is at the first critical location $\theta_{c1} = 43°$, and it significantly contracts between

the angles θ_{c2} = 55° and 70°. This observation regarding the extent of the near wake is also evident from the time-averaged streamline $<\psi>$ patterns given in the second column in Figure 4.12, where the streamwise distance of the saddle point from the base is relatively large at θ_{c1} and it is relatively short at θ_{c2}. These distinguishing effects of a straight wire at the critical locations θ_{c1} and θ_{c2} are consistent with Ekmekci and Rockwell (2010).

As a further pronounced effect, at critical angular locations (θ_{c1} = 43° and θ_{c2} = 55° to 70°), the wire induces a large amount of distortion in the near-wake, apparent from the asymmetry in the iso-contours of time-averaged vorticity $|<\omega>D/U_o|$ (the third column of Figure 4.12). It can also be observed that the negative $<u>/U_o$ contours reach upstream toward the wire-side of the cylinder (which is the upper side in the images). This increased spread of the reverse flow as well as the asymmetry in the vorticity contours were attributed earlier by Ekmekci and Rockwell (2010) to the increased entraintment demand of the early development of the shear-layer instability on the wire-side shear layer.

Global contour patterns of velocity spectra at the predominant Karman frequency, $S_u(f_K)$, given in the fourth column of Figure 4.12, depict the influence of the wire on the strength and coherence of the Karman instability over the global near-wake region. Peak amplitudes of spectra and hence the coherence of Karman vortex shedding shows a dramatic decrease when the wire is at θ_{c1} = 43° compared to the reference case at θ =180°. On the other hand, the spectral strength is amplified at the secondary critical locations θ_{c2} = 55° and 70° relative to the reference case of θ = 180°. These observations are consistent with the findings presented in Figure 4.11 and are in good agreement with the previous findings of Ekmekci and Rockwell (2010).

As a further aspect, changes in the vortex formation length and the wake width with the wire angular location θ are determined from the PIV data and shown in Figure 4.13. The vortex formation length, L_F, is defined as the distance between the base of the cylinder and the saddle point, which is the location where the streamlines intersect at the closure of the near-wake. The wake width, w, is determined, in the present study, as the distance between the two points where the streamwise velocity component reaches a value of $0.8U_o$ on either side of the saddle point. In accord with the observations presented in Figure 4.12, the vortex formation length, L_F/D, reaches to its maximum when the wire is at the first critical angle θ_{c1} and it attains its minimum when the wire is at the second critical angles θ_{c2} (Figure 4.13). While the vortex formation length increases

by 53% at θ_{c1}, it decreases by 40% at θ_{c2}. On the other hand, the wake width increases by 14% when the wire is located in the second critical angle compared to the reference case.

A further critical characteristic identified earlier by Ekmekci (2006) and Ekmekci and Rockwell (2010) is the existence of a bi-stable state when the wire is placed at the first critical location. This bi-stable state was shown to involve the intermittency of the shear layer between the re-attachment and no-attachment modes downstream of the wire at broad frequencies, centered on a low frequency value. The PIV measurements in the shear layer within the close proximity of the wire show a similar bi-stable situation, centered on a broad band low frequency. Figure 4.14 shows the contour plots of the autospectral amplitude of the streamwise velocity component decomposed into the low frequency f_L (shown on the left column) and the Karman frequency f_K (shown on the right column). These contour plots are provided for various wire angles; $\theta = 41°$, 43° (θ_{c1}), 45°, 47°, 50° (θ_{c2}), 55° (θ_{c2}), and 180° (reference case) for comparison. For θ at the first critical location (θ_{c1} = 43°), the peak spectral amplitude of velocity fluctuations shows an increase at the low frequency component (f_L) while the spectral amplitude at the Karman frequency (f_K) decreases. The ratio of these frequencies is f_L/f_K = 0.14 at this wire angle, where St = 0.243 for the Karman vortex shedding. The decrease in the coherence and strength of Karman instability observed in these spectral plots in the shear layer region is completely consistent with the results presented in Figure 4.12 over the near-wake region. It is known from the works of Ekmekci and Rockwell that the prevailing low-frequency at θ_{c1} is associated with the bi-stable state of the shear-layer. A further observation is that the peak spectral amplitude of fluctuations at the Karman frequency (f_K) increases significantly when the wire is at the second critical angle, θ = 50° or 55°, compared to the reference case (θ = 180°). Once again, this is also totally consistent with the findings presented in Ekmekci and Rockwell (2010). It is known from the previous work of Ekmekci and Rockwell (2010) that, at the second critical location, the flow separates completely at the wire location. Apparently, this leads to an increase in the wake width and the decrease in the vortex formation length, as observed in Figure 4.13 for the second critical locations.

4.6.2. High Reynolds number case; Re_D = 25,000

4.6.2.1. Spectral features of the velocity signals

Now, let's turn our attention to the high Reynolds number case for Re_D = 25,000 (d/D = 0.059), and start studying the spectral features of the velocity signals sampled with both CTA and PIV.

Similar to the previous analyses, the distributions of the predominant Strouhal number, St, and the spectral amplitude of the velocity fluctuations at Karman shedding frequency, $S_u(f_K)$, are given as a function of the wire angle, θ, in the top and bottom parts of Figure 4.15, respectively. The velocity signals are sampled at a location of $x/D = 4.3$, and $y/D = 3$ with the hot-film (CTA) probe. On the other hand, the sampling point for PIV is located at $x/D = 2.5$, and $y/D = 1.25$. The increase in Strouhal number starts at the wire angle of $\theta = 30°$, and reaches its maximum value of $St = 0.253$ at $\theta = 46°$ according to CTA data. A slight increase in the wire angle beyond this location results in a sharp drop in St to a value of about 0.18 and follows a crater-like distribution with increasing wire angle until the end of range of effective wire angles, $\Delta\theta$. After $\theta = 117°$ (based on CTA data), the wire is ineffective on the vortex shedding frequency. Although the curve plot for St-θ curve shows a similar trend shown in Figures 4.2, 4.4, 4.6, and 4.11, there are slight discrepancies in the values of Strouhal number between the data sets obtained with both experimental methods due to the uncertainties associated with the spectral analysis. The uncertainty analyses are based on *Root-Sum-Square* equation, again, whose details are given in App. A.1. The uncertainty in St is $\Delta St_{PIV} = 0.0042$ for the PIV data and $\Delta St_{CTA} = 0.002$ for the CTA data.

In the second step of our analysis, let's focus on the variation of $S_u(f_K)$ over the wire angles, which is provided in the bottom part of Figure 4.15. The spectral amplitude of velocity fluctuations at Karman vortex shedding frequency decreases consistently within the wire angle range of $30° \leq \theta \leq 46°$ as the value of Strouhal number increases gradually. The coherency and strength of Karman vortex shedding reaches its minimum at $\theta = 46°$, with a 40% drop (based on PIV data) or a 85% drop (based on CTA data) in fluctuation strength. This angular location is considered as the first critical location θ_{c1} in accord with the definition by Ekmekci (2006), and Ekmekci and Rockwell (2010). As the wire angle is further increased, the amplitude of velocity spectra at Karman frequency, $S_u(f_K)$, and Strouhal number, St, continue to follow a roughly inverse relationship until $\theta = 117°$. As Strouhal number decreases, the coherency of Karman shedding increases and reaches its maximum values for a range of wire angles of $50° \leq \theta \leq 70°$. This range is marked as θ_{c2} in the figure.

4.6.2.2. Time-averaged near-wake and shear-layer structures

In the previous section, the critical angles have been determined as $\theta_{c1} = 46°$, and $\theta_{c2} \approx 50°$-$70°$ for $Re_D = 25{,}000$ and $d/D = 0.059$. This section presents the flow structures based on the PIV

measurements related to these critical states of the flow. Figure 4.16 presents the time-averaged patterns of the normalized streamwise velocity $<u>/U_o$, streamlines $<\psi>$, absolute normalized vorticity $|<\omega>D/U_o|$ along with the contour patterns of the spectral amplitude at Karman frequency $S_u(f_K)$ in the first through last columns, respectively. These flow quantities are plotted for the wire angles of θ = 46°, 60°, 70°, 110°, and 180°.

The comparison of the pockets of reverse flow within the near-wake bubble, represented by the dashed lines in the first column of Figure 4.18, shows that the near-wake bubble extends the most at $\theta = \theta_{c1}$, and contracts significantly for $\theta = \theta_{c2}$ compared to the reference case of θ = 180° where the wire is ineffective. This observation can also be made on the time-averaged streamlines ($<\psi>$), presented in the second column, based on the comparison of the streamwise extent of the closed recirculation region. The maximum wake extension and contraction of the near-wake at the first and second critical wire angles respectively are in perfect agreement with the spectral features of the velocity signals.

In addition, the wire is observed to lead to, again, a significant amount of asymmetry on the iso-contours of the time-averaged vorticity ($|<\omega>D/U_o|$), given in the third column, when placed at the critical angular locations (θ_{c1} = 46° and θ_{c2} = 60° to 70°). This distortion in the near-wake region is also evident in the iso-contours of the streamwise velocity component where there is an increase in the suction towards the wire side of the cylinder (upper side in the images). This asymmetry in the vorticity distribution and increase in the reverse flow were both previously associated with the increased entrainment demand of the shear layer and early development of the shear-layer instability on the wire-side shear-layer by the effect of the wire at critical locations (Ekmekci 2006, Ekmekci and Rockwell 2010).

As a final note on Figure 4.16, global contour patterns of velocity spectra at the predominant Karman frequency ($S_u(f_K)$), given in the fourth column, show a significant amount of decrease at the first critical location, and an increase in the second critical locations compared to the reference case. These results are matching with the previous findings presented in Figure 4.15 and are in accord with the effects of the wire at the low Reynolds number case (Re_D = 10,000, d/D = 0.059), as well as the findings of Ekmekci and Rockwell (2010).

At this point, let's turn our attention to how the vortex formation length and wake width are changing as a function of the wire angle, given in Figure 4.17. The vortex formation length, L_F,

increases consistently until the first critical wire angle, θ_{c1}, where it reaches its maximum value of 1.39D. This result is in accord with the findings presented in Figure 4.16 (first row), and consistent with the findings of Ekmekci and Rockwell (2010). At the second critical wire angle of $\theta_{c2} = 60°$, the length of vortex formation stays at its lowest value ($L_F = 0.51D$) due to the wake contraction. Compared to the reference case at $\theta = 180°$, where $L_F = 1.03D$, the increase and decrease in vortex formation length at first and second critical angles are 34%, and 51% respectively. On the other hand, the wake width follows an approximate inverse trend compared to the formation length; it gradually decreases to its minimum value of 1.14D at $\theta_{c1} = 43°$, and increases to its maximum value of 1.61D at around $\theta_{c2} = 70°$. Compared to the reference case in $\theta = 180°$ ($w = 1.31D$), the increase and decrease in the wake width at these angles are 13%, and 22%, respectively. These observations are consistent with the findings of Nebres and Batill (1993) which showed the variation of the shear layer spacing and longitudinal vortex spacing for a larger wire ($d/D = 0.089$) at a higher Reynolds number ($Re_D = 30{,}000$).

In order to explain the changes in the wake width, the time-averaged iso-contours of normalized streamwise velocity ($<u>/U_o$) and time-averaged streamlines ($<\psi>$) are given in Figure 4.18 for the wire locations of $\theta = 43°$, 45°, 47°, 50°, 60°, and 180° in the close proximity region of the wire. Dashed lines for the iso-contours of velocity show negative values, thus represent the reverse flow region. Both of these time-averaged flow quantities show a re-attached flow for $\theta = 43°$ and 45°, which are 3° and 1° degrees before the first critical angle ($\theta_{c1} = 46°$). At these wire locations, Strouhal number is close to $St = 0.25$, and vortex shedding is less coherent compared to the reference case based on Figure 4.15. According to the previous findings of Igarashi (1986), Nebres (1992), Nebres and Batill (1993), Ekmekci (2006), Ekmekci and Rockwell (2010), the flow state at this wire angle is stable and the flow separating at the wire re-attaches to the cylinder surface and transits to a turbulent boundary layer prior to the final separation from the cylinder. This leads to a delayed separation from the cylinder, and leads to a narrower wake. On the contrary, the wake width encountered at the second critical angle of $\theta_{c2} = 50°$ and 60° is increased compared to the reference case. For wire angles $\theta > \theta_{c1}$, the flow state is stable and involves final flow separation at the wire location leading to an increase in the wake width. This phenomenon is shown in Figure 4.18 for $\theta = 47°$, 50°, and 60° (all of which are past $\theta_{c1} = 46°$) where the iso-contours of velocity and streamlines show reverse flow close to the cylinder surface downstream of the wire.

Next, the flow features related to the bi-stable flow state encountered at the first critical wire angle are discussed for the high Reynolds number case (i.e. Re_D = 25,000). In order to evaluate this situation, contour plots of the spectral amplitude of the velocity spectra are given for wire angles of θ = 43°, 45°, 46° (θ_{c1}), 47°, 50° (θ_{c2}), 60° (θ_{c2}), and 180° in Figure 4.19. These global contours show the amplitude of the velocity spectra decomposed into the low frequency, f_L (shown at the left column), and the Karman frequency, f_K (shown at the right column). The low frequency component is of broadband nature and represents the frequency at which the bi-stable flow switches between the stable states encountered before and after the first critical angle (mentioned above). For wire angles smaller than but close to θ_{c1}, i.e. θ = 43° and 45°, the contour plots do not show any evidence of fluctuations at neither of the frequencies. This is, in fact, expected; the fluctuations at the low frequency (f_L) are insignificant due to a steady flow separation at the wire, and re-attachment downstream while the spectral amplitude at Karman frequency (f_K) is low due to the loss of coherency in Karman shedding at these wire angles. At the first critical angle (θ = θ_{c1}), the low frequency component prevails in the whole flow field, i.e. shear-layer region at the wire-side of the cylinder, while the fluctuations at the Karman frequency stay at noise levels. For wire angles greater than the first critical angle (θ = 47°, 50°, and 60°), the amplitudes of fluctuations at the low frequency gradually decrease while the fluctuations at the Karman frequency dominate the region in close proximity of the wire. In addition, the spectral amplitude at Karman frequency, $S_u(f_K)$, are significantly increased for the wire angles of θ = 50°, and 60°, which is consistent with the results given in Figure 4.15, and 4.16.

4.7. Relationship Between Different Sets of Critical Angles and Flow Regimes

So far, the effects of a single, large-scale spanwise wire on the flow around a circular cylinder have been investigated by focusing on the attenuation/amplification characteristics of Karman shedding, the changes in Strouhal number, vortex formation length and wake width as the functions of the wire angle for different wire sizes ($0.029 \leq d/D \leq 0.059$) and Reynolds numbers ($5{,}000 \leq Re_D \leq$ 30,000). The pivotal points of the discussion were the critical angles, θ_{c1} and θ_{c2}, defined by Ekmekci and Rockwell (2010). At this point, it is important to recall that one of the unresolved issues put forward in section 1.4 is the relationship between the critical angles defined in two independent studies (θ_{c1}, θ_{c2}, θ_t, θ_c, θ_m, θ_r, θ_b) and associated flow regimes.

In order to understand how these critical angles are related to each other, it is useful to superimpose these different sets of critical angles; (θ_{c1}, θ_{c2}) defined by Ekmekci and Rockwell (2010), and (θ_t, θ_c, θ_m, θ_r, θ_b) defined by Nebres and Batill (1993) on a single sketch in Figure 4.20. In this figure, variations of the Strouhal number, St, and the spectral amplitude at Karman frequency, $S_u(f_K)$, are sketched as a function of the wire angle, θ, to illustrate the typical behaviour reported in the previous sections, which are aligned with the past studies. The critical angles are marked on both of the plots. Below is a summary of the associated flow regimes compiled from the findings of the past studies (Ekmekci 2006, Ekmekci and Rockwell 2010, Nebres 1992, Nebres and Batill 1993) and the current study with increasing wire angle from $\theta = 0°$ to $\theta = 180°$.

$0° \leq \theta \leq \theta_t$: The Strouhal number and the strength and coherency of the vortex shedding are similar to the reference case and the wire is ineffective. The flow separates at the wire and re-attaches to the cylinder surface. The boundary layer forming after the re-attachment points stays laminar prior to the final separation from the cylinder.

$\theta_t < \theta \leq \theta_c$: Strouhal number consistently increases from its reference value to its maximum value (St_{max}) at $\theta = \theta_c$. In the meantime, the spectral strength of Karman shedding decreases but doesn't reach to its minimum at $\theta = \theta_c$. The flow re-attaches to the cylinder surface downstream of the separation at the wire and transitions to a turbulent boundary layer before the final separation from the body. Vortex formation length increases. Wake width decreases due to the delayed separation of the turbulent boundary layer on the wire side.

$\theta = \theta_{c1}$: The coherency of Karman shedding is at its minimum. There are periods of time where vortex shedding ceases and, also, short periods of time where regular shedding continues. The flow state is bistable, and switches between two stable regimes; steady re-attachment downstream of the wire and steady separation at the wire. This results in a broad-band low frequency component in the velocity fluctuations within the close proximity of the tripwire. This low frequency (f_L) is one order of magnitude smaller than Karman frequency and is dominant within the immediate vicinity of the wire. Strouhal number can vary between St_{max} (observed for $\theta = \theta_c$) and a value lower than the reference value. Vortex formation length reaches to its maximum value.

$\theta = \theta_{c2}$: Strouhal number is typically lower than the reference value. Spectral amplitudes of the velocity fluctuations at Karman frequency reach to their maximum levels. The vortex formation length reaches to its minimum value. Due to the increased lateral oscillatory motion of the near-

wake, and final flow separation occurring at the wire location, the wake width increases to its maximum.

$\boldsymbol{\theta = \theta_m}$: Strouhal number reaches its minimum. The spectral amplitudes of the velocity signals at the Karman frequency are stronger compared to the reference case.

$\boldsymbol{\theta = \theta_r}$: The angular location where a secondary increase in Strouhal number, and a secondary decrease in the coherency of Karman shedding can be observed depending on the wire size and Reynolds number.

$\boldsymbol{\theta = \theta_b}$: The angular location where the range of effective wire angles comes to an end. At this wire location, Strouhal number and the coherence of Karman shedding is at the same level compared with the scenario where the wire has no effect.

$\boldsymbol{\theta_b < \theta \leq 180°}$: At this range of wire angles, the wire is in the base region of the cylinder, and doesn't have any significant effect on the flow.

Although the changes in the wake flow are similar at these critical wire angles, the values of the critical angles, Strouhal number boundaries (St_{max}, St_{min}) and ranges of effective wire angles are depent on the wire size and Reynolds number. The effects of the wire size and Reynolds number were mentioned mostly around the attenuation/amplification of Karman shedding previously at sections 4.3 and 4.4. In the current section, this discussion will be expanded to the whole set of critical angles and Strouhal number boundaries. To serve as a basis, the values of these quantities are given in Table 4.2.

Based on the values of the critical angles and Strouhal number boundaries presented in Table 4.2, following observations are worthwhile to mention. In general, an increase in the wire size or Reynolds number leads to an increase in the effective range of wire angles ($\Delta\theta$), range of wire angles with delayed separation (θ_c - θ_t), and the degree of changes in Strouhal number (St_{max} - St_{min}) in accord with Nebres 1992 and Nebres and Batill 1993. While increase in Reynolds number for a constant wire size leads to a slight increase in the values of the first critical angle (θ_{c1}) for Re_D = 5,000, and 10,000, the value of θ_{c1} remains constant for $Re_D \geq$ 15,000. On the other hand, an increase in the wire size at a constant Reynolds number consistently leads to a decrease in the angular location of the first critical angle. In general, the location of θ_{c1} comes slightly after θ_c. The range of wire angles for the second critical angle is found to start, on average, 8° after the first critical angle. The value of the critical angle θ_m stays between 68° - 69°. The range of wire angles,

where a secondary increase in Strouhal number is observed for $\theta_r \leq \theta \leq \theta_b$, starts around θ = 103° - 112° and lasts for another 5°.

Table 4.2 Values of critical angles and Strouhal number boundaries based on the experimental data of the current study.

Re_D	d/D	θ_t	θ_c	θ_m	θ_r	θ_b	θ_c-θ_t	$\Delta\theta = \theta_b$-θ_t	St_{max}	St_{min}	St_{max} - St_{min}	θ_{c1}	θ_{c2}
5,000	0.029	43	45	68	103	103	2	60	0.214	0.174	0.040	47	53-69
10,000		43	47	69	103	108	4	65	0.215	0.175	0.040	48	53-73
15,000		43	53	69	103	108	10	65	0.248	0.176	0.072	53	57-69
25,000		35	51	69	103	108	16	73	0.246	0.172	0.072	53	57-73
30,000		35	51	69	103	108	18	75	0.248	0.169	0.079	53	55-73
5,000	0.039	33	41	69	103	108	8	65	0.214	0.168	0.046	43	51-66
10,000		39	45	69	103	103	6	64	0.221	0.168	0.053	47	49-69
15,000		33	47	69	103	103	15	71	0.243	0.168	0.075	49	53-73
25,000		30	47	69	103	108	17	78	0.251	0.168	0.083	49	51-73
30,000		30	47	69	103	108	17	78	0.251	0.168	0.083	49	53-69
5,000	0.059	32	40	68	107	107	8	75	0.214	0.161	0.053	42	48-65
10,000		32	43	68	112	122	12	90	0.235	0.168	0.067	44	50-70
15,000		34	46	68	112	117	12	83	0.251	0.168	0.083	46	52-70
25,000		30	46	68	112	117	14	86	0.253	0.163	0.090	46	50-70
30,000		32	44	68	112	117	12	85	0.253	0.163	0.090	46	50-70

4.8. Chapter Conclusions

The flow around a circular cylinder fitted with a single, spanwise wire has been studied for a range of wire sizes ($0.029 \leq \theta \leq 0.059$) and sub-critical Reynolds numbers ($5{,}000 \leq Re_D \leq 30{,}000$). The effects of the wire on the strength and coherency of Karman shedding, the Strouhal number, and the flow structures are investigated as a function of the wire angle with the use of various experimental techniques; namely Constant Temperature Anemometry (CTA), hydrogen bubble flow visualization, and Particle Image Velocimetry (PIV).

The size of the each wire is found to be larger than the unperturbed boundary layer thickness, and, therefore, all the wires considered in this investigation are determined to be a large-scale wire. For all the Reynolds numbers and wire sizes considered here, two types of critical locations were shown to exist on the cylinder surface for the application of a spanwise tripwire. These locations were denoted as θ_{c1} and θ_{c2} in accord with the existing literature. Spectral analysis of the velocity signals provided a straightforward means for determining these locations. θ_{c1} was recognized as the location on the cylinder surface where placing a wire would alleviate the peak spectral amplitude of velocity fluctuations the most. Also, notable irregularities could be identified even from an inspection of the velocity signals for θ_{c1} wire location. This critical location was identified

as a single angle on the cylinder surface. On the other hand, θ_{c2} was associated with a drastic increase in the peak spectral amplitude and was found to encompass a range of angular locations on the cylinder surface, extending roughly from 50° to 70°. While the range of θ_{c2} locations was generally not affected from the Reynolds number and wire size, the value of θ_{c1} was. For a given Reynolds number, increasing the wire size led to a decrease in the value of θ_{c1}. On the other hand, for a given wire size, until a Reynolds number of about 15,000, increasing the Reynolds number increased the value of θ_{c1}, but beyond 15,000, θ_{c1} became independent of the Reynolds number.

The time-frequency analysis of the velocity signals and the long-time records of hydrogen-bubble images in the near wake showed that, with a large-scale wire at θ_{c1}, rhythmic development of Karman vortex clusters ceases at times and resumes at other times. The resumption phase, however, lasted for only a couple of cycles, and for the majority of the time, a no-shedding phase was observed. Another observation in relation to the effect of a wire at the θ_{c1} location was that during the times when the Karman shedding was disrupted, the near-wake bubble extended considerably in the streamwise direction. As for the θ_{c2}, a large-scale wire at a θ_{c2} location pronounced the coherence and strength of the Karman vortices, and the near-wake bubble became significantly contracted.

In addition, this investigation also showed that the spectral amplitude and frequency of the velocity fluctuations corresponding to the Karman instability can be controlled by a single wire only if that wire is located over a certain range of angular locations ($\Delta\theta$), the value of which was found to depend on the Reynolds number and wire size. Within this range of angles, with increasing wire angular location θ, the shedding frequency typically underwent a crater-like variation with a slight rise at the beginning and end of this variation, which is in perfect agreement with the existing literature. On the other hand, the spectral amplitude at the Karman frequency followed a change that has roughly an inverse association with the frequency variation. The general trend was that the spectral amplitude decreases while the *St* increases, and vice-versa. However, it should be noted that what is being mentioned here is an approximate relationship and, for example, the location where placing a wire attenuates the spectral amplitude at Karman frequency the most, i.e., the θ_{c1} location, does not coincide with the location where the frequency reaches a peak. This novel finding of this study provided a basis for the relationship between two different sets of wire angles defined in the literature. Based on this relationship and the findings of the previous studies, a

summary of the flow regimes encountered at different wire angular locations or ranges of wire angles is given.

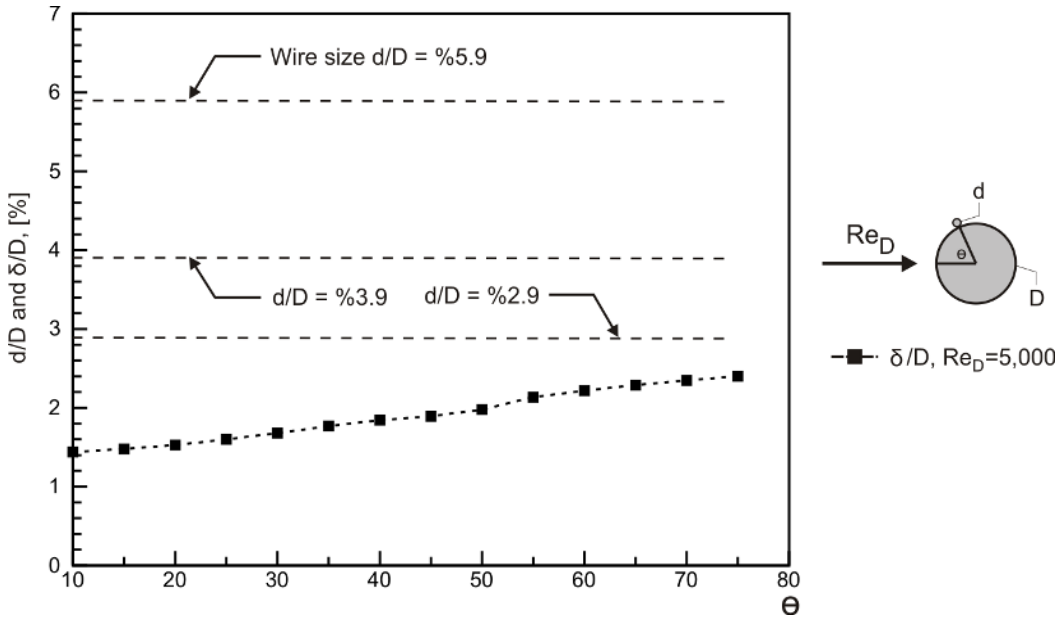

Figure 4.1 Wire scale (*d/D*) compared to the boundary-layer thickness (*δ/D*), forming around a smooth cylinder at Re_D = 5,000.

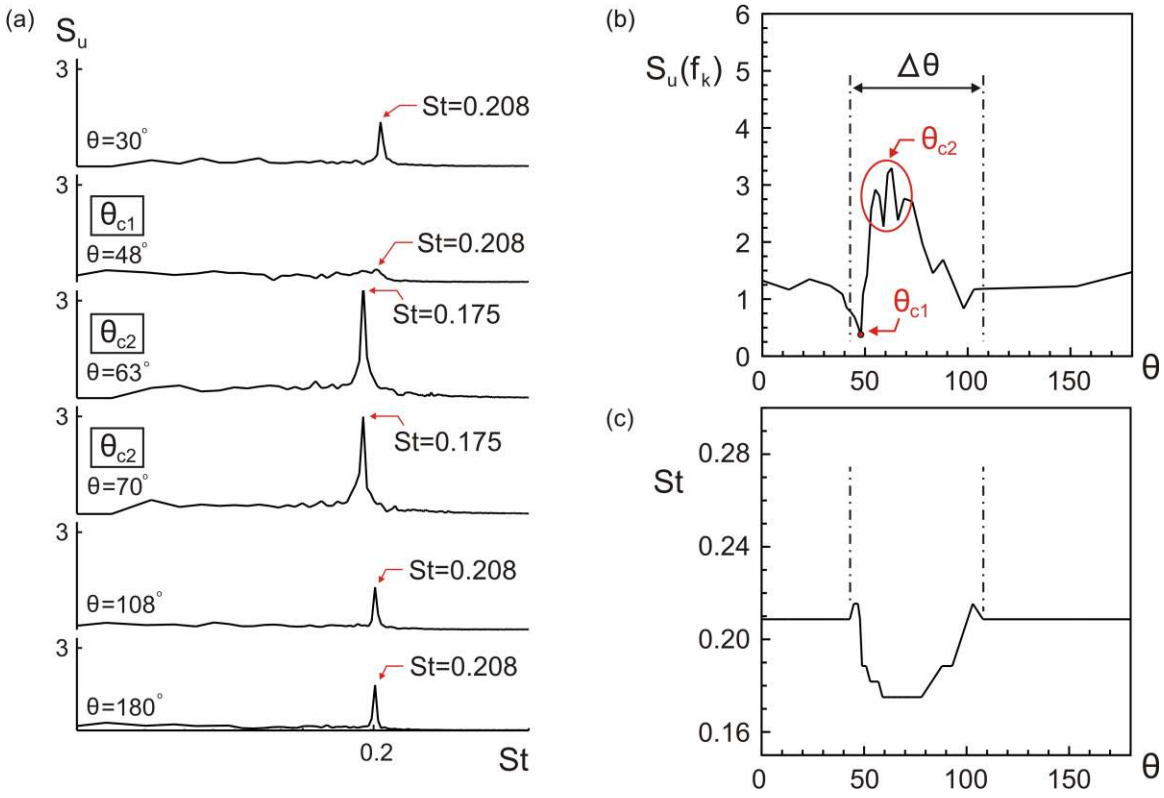

Figure 4.2. (a) Autospectral density S_u of the streamwise velocity component for *d/D* = 0.029 at Re_D = 10,000 are shown for different angular positions, θ, of the wire. Herein, the value of the predominant Strouhal number, *St*, are also indicated for each θ. The horizontal axis in this plot is in log scale. (b) Amplitude of streamwise velocity spectra S_u at the predominant Karman frequency f_K is plotted against wire position, θ. (c) Variation of the prevailing Strouhal number, *St*, of the velocity fluctuations with the wire angular position, θ. The velocity signals used for spectral analysis were acquired at *x/D* = 4.3, *y/D* = 3, and *z/D* = 0.

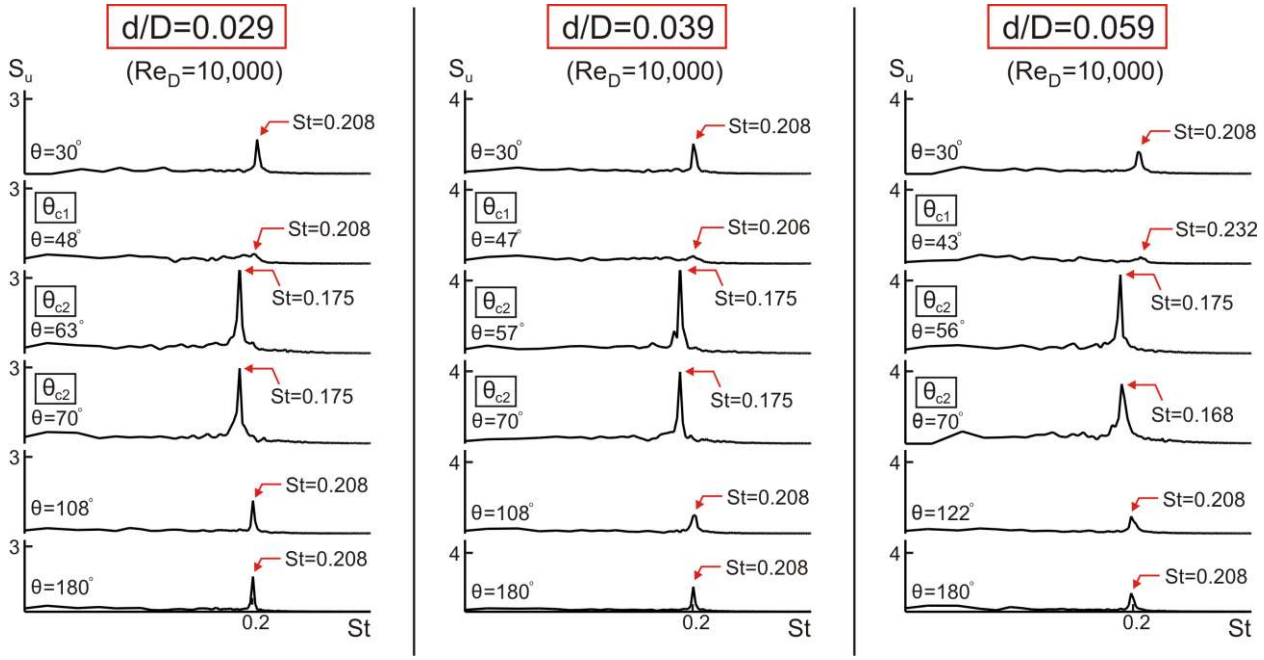

Figure 4.3 Autospectral density S_u of the streamwise velocity component for d/D = 0.029, 0.039, 0.059 at Re_D = 10,000 for selected angular positions, θ, of the wire. The predominant Strouhal number, St, are indicated for each θ (St axis is plotted in log scale).

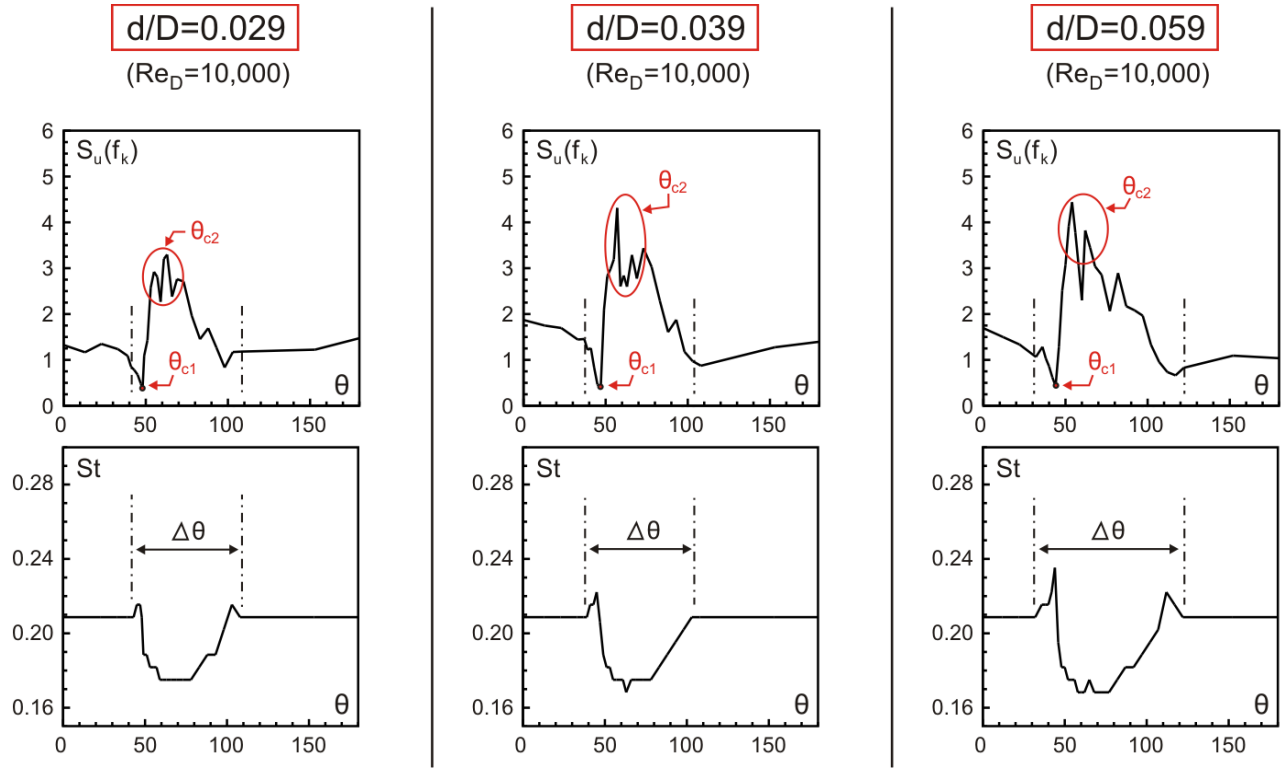

Figure 4.4 Top row: variation in the amplitude of streamwise velocity spectra at the predominant shedding frequency, $S_u(f_K)$, as a function of the wire angular position θ; bottom row: variation in the Strouhal number St as a function of the wire angular position θ for d/D = 0.029, 0.039, 0.059 and Re_D = 10,000.

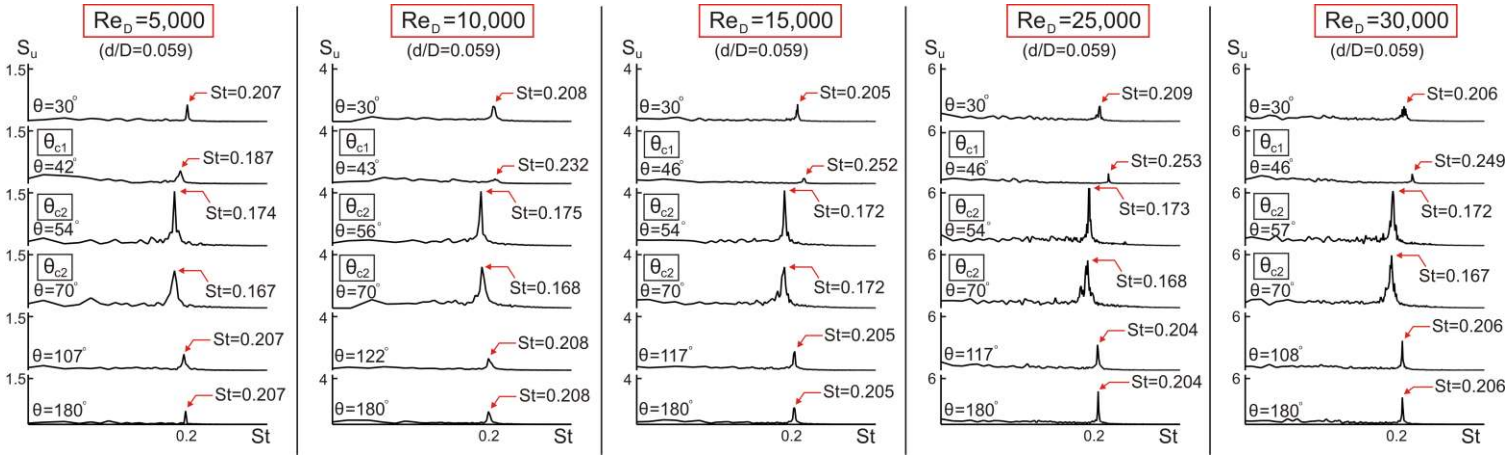

Figure 4.5 Autospectral density S_u of the streamwise velocity component for d/D = 0.059 at Re_D = 5,000 to 30,000 for different angular positions, θ, of the wire. The predominant Strouhal number, St, are indicated for each θ. Note the change in the scale of the vertical axis for Re_D = 25,000, and 30,000 (St axis is plotted in log scale).

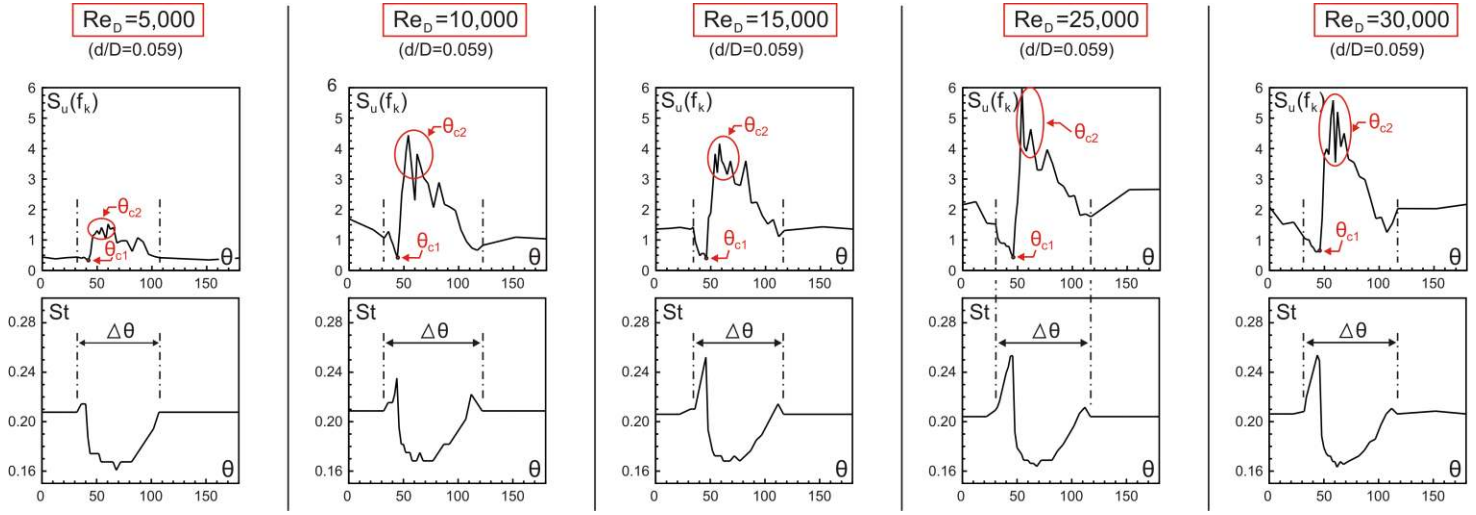

Figure 4.6 Variation of Strouhal number, St, and the amplitude of autospectral density at the shedding frequency, $|S_u(f_K)|$, as a function of wire angle, θ, for 5,000 ≤ Re_D ≤ 30,000 and d/D = 0.059

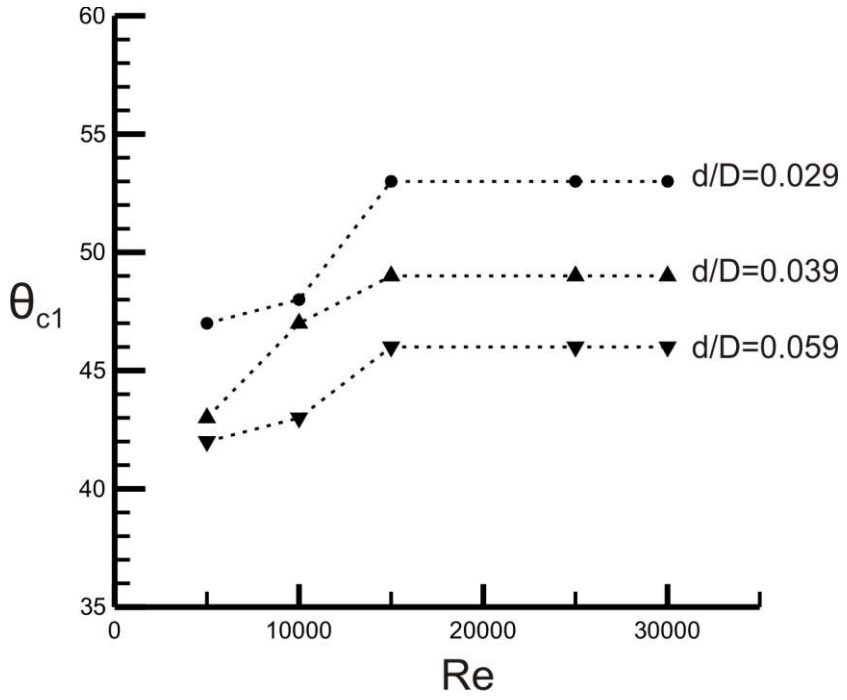

Figure 4.7 Variation of θ_{c1} as the function of Reynolds number for different wire sizes.

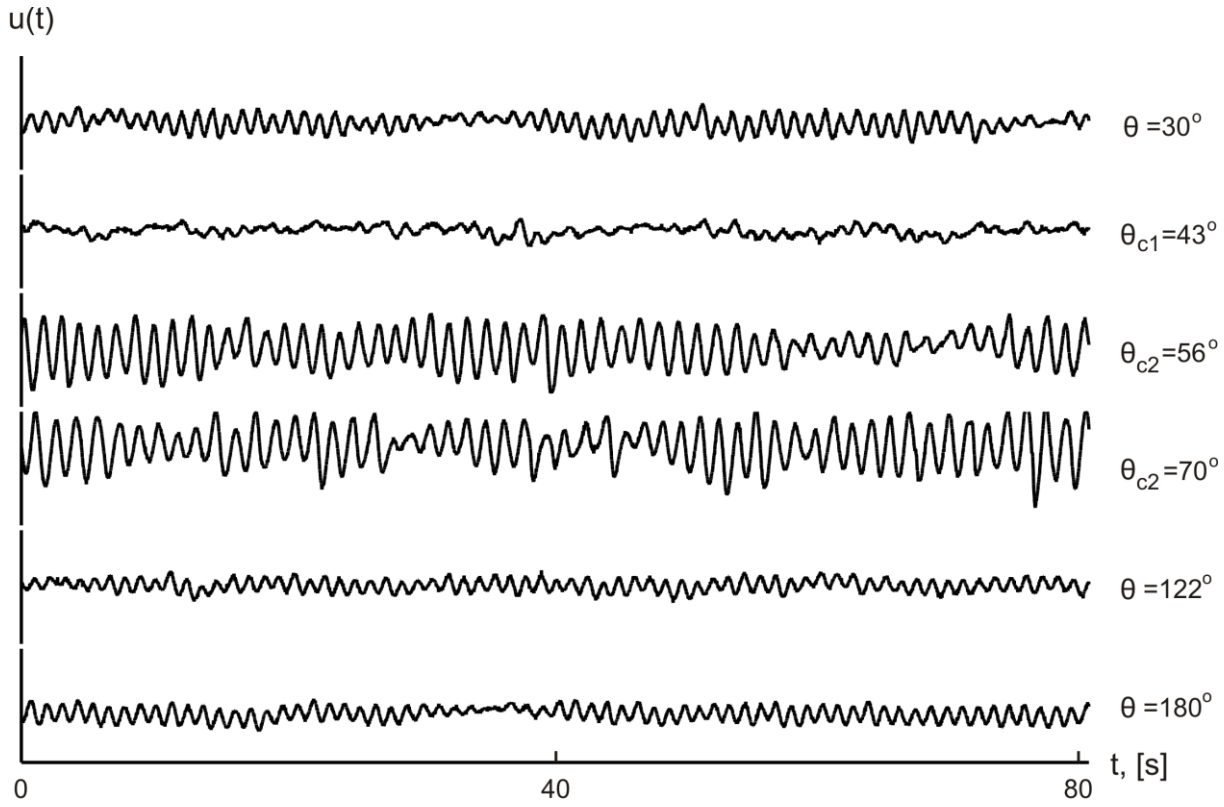

Figure 4.8 Time traces of streamwise velocity component, u, for d/D = 0.059 at Re_D = 10,000. Hot-film probe is located 4.3D downstream and 3D lateral from the cylinder center. For the ease of visual inspection, only a portion of the signal is displayed.

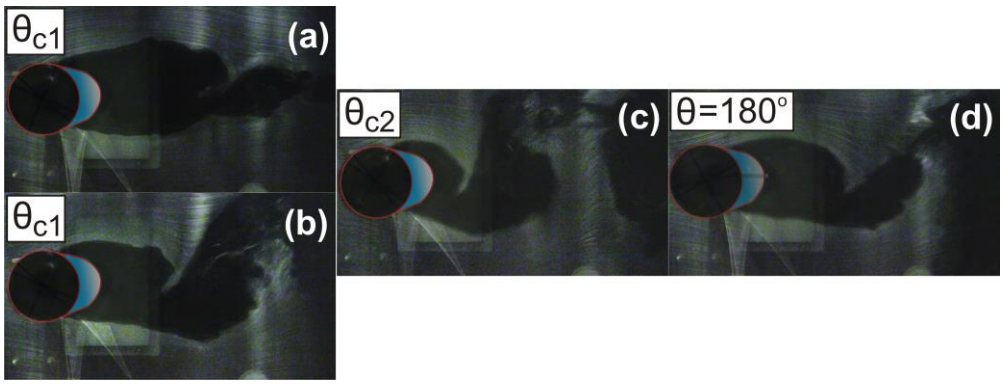

Figure 4.9 Hydrogen bubble visualization of the near wake for d/D = 0.059 at Re_D = 10,000. The wire is (a) at the first critical angle θ_{c1} when the regular Karman vortex shedding is interrupted, (b) at the first critical angle θ_{c1} when the Karman vortex shedding resumes, (c) at a second critical angle θ_{c2}, and (d) when the wire is at the base, i.e., at θ = 180°.

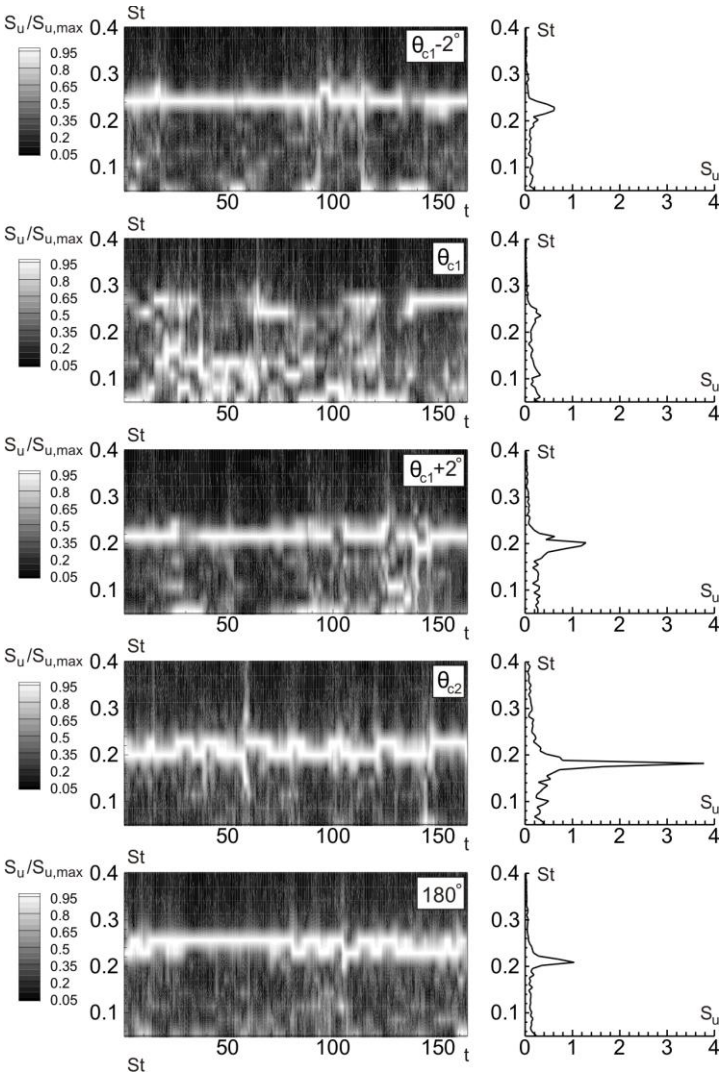

Figure 4.10 Time-frequency spectrogram of the CTA signals for $\theta = \theta_{c1}$-2°, θ_{c1}, θ_{c1}+2°, θ_{c2}, and 180° for d/D = 0.059 and Re_D = 10,000. Also, on the right hand side, corresponding (time-averaged) velocity spectra are provided.

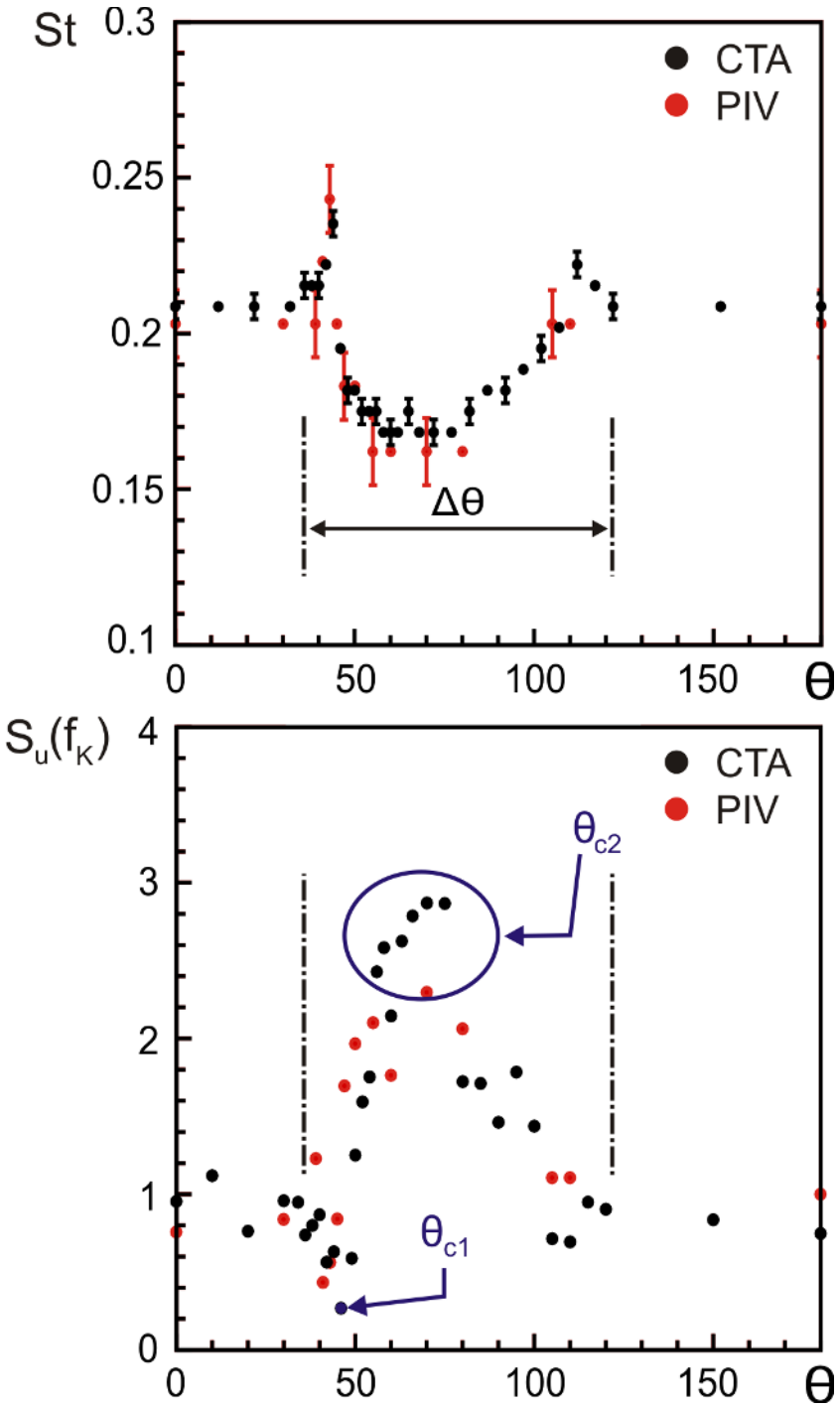

Figure 4.11 The Strouhal number, *St*, and the spectral amplitude of velocity fluctuations, $S_u(f_K)$, at the predominant (Karman) frequency are plotted against the wire angular location θ. Values are estimated from the velocity signals obtained from CTA and PIV measurements. (Re_D = 10,000, d/D = 0.059)

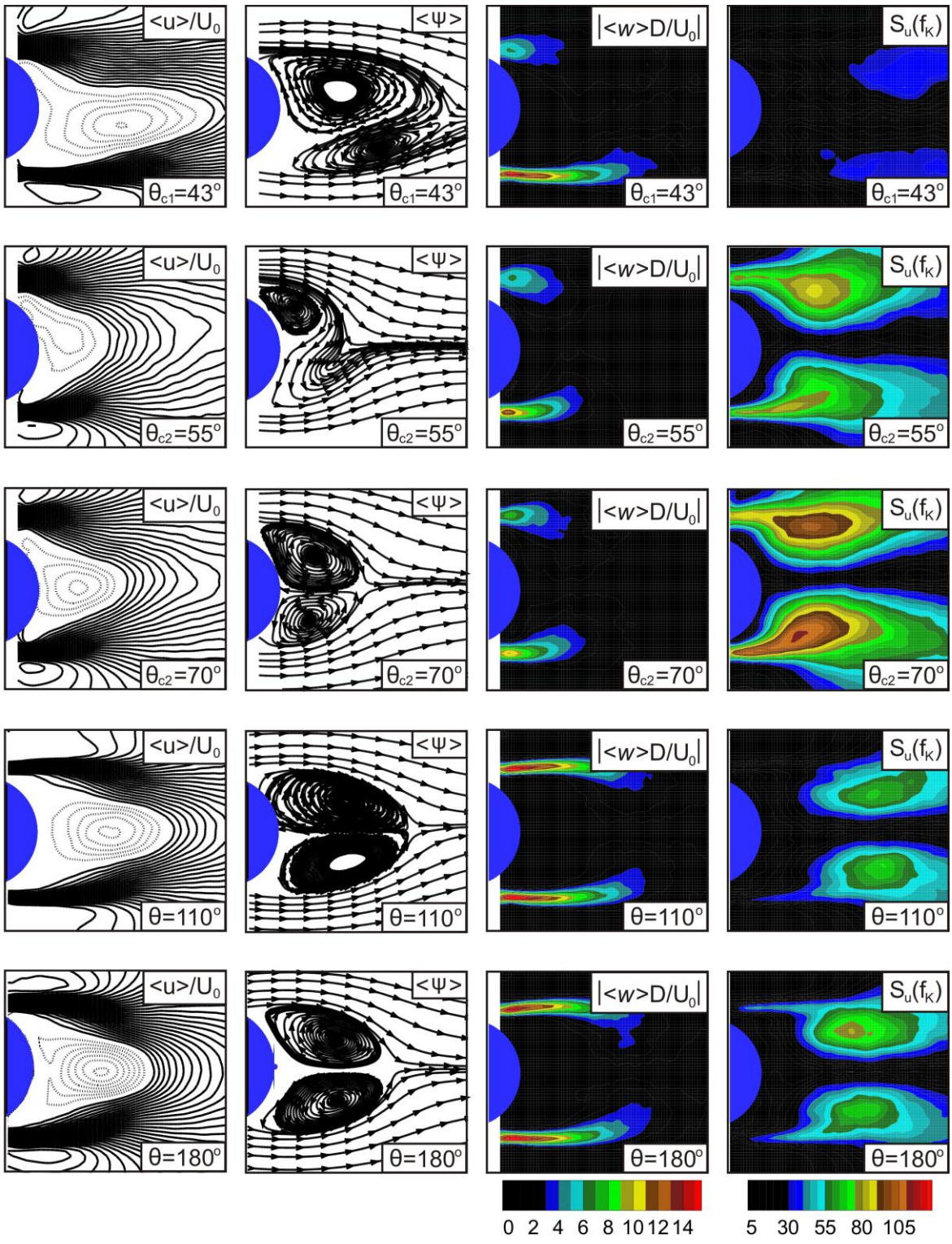

Figure 4.12 Iso-contours of time-averaged, normalized streamwise velocity components ($\langle u \rangle / U_0$; first column), time-averaged streamlines ($\langle \psi \rangle$; second column), time-averaged, normalized vorticity ($|\langle w \rangle D/U_0|$; third column), and iso-contours of the amplitude of streamwise velocity spectra at Karman frequency ($S_u(f_K)$; fourth column). (Re_D = 10,000, d/D = 0.059)

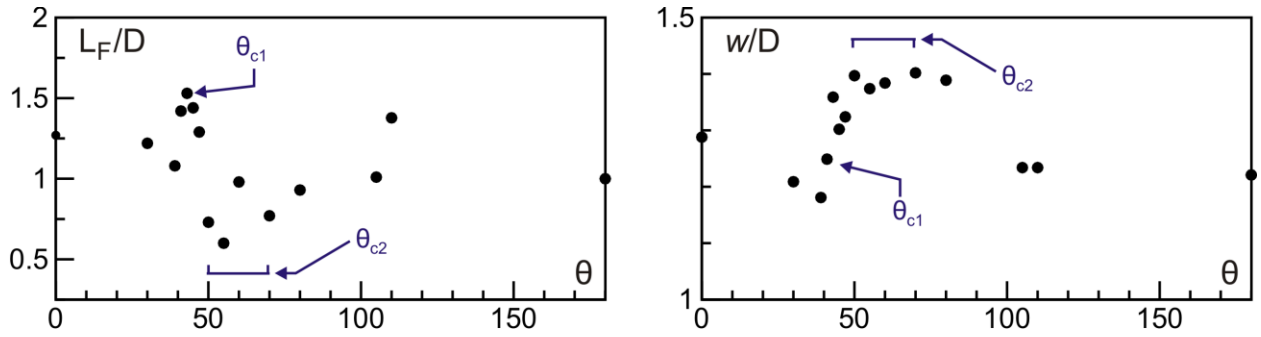

Figure 4.13 Vortex formation length and wake width as a function of wire angle. (Re_D = 10,000, d/D = 0.059)

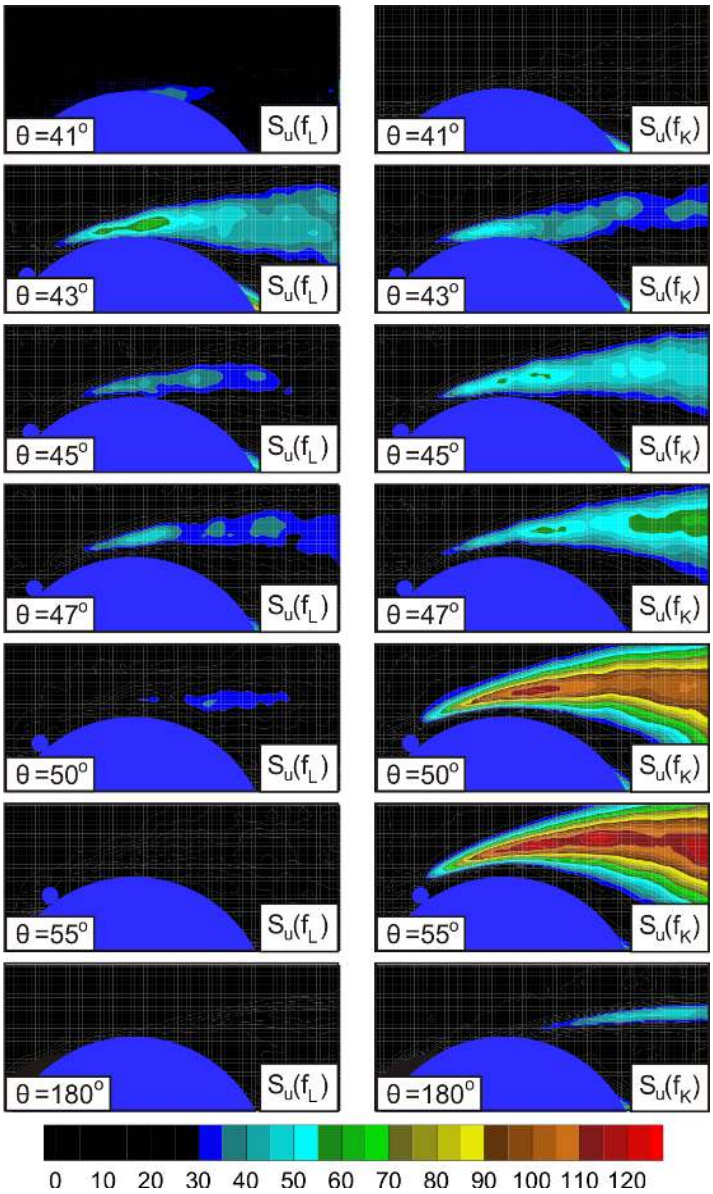

Figure 4.14 Contour patterns of constant amplitude of velocity spectra, $S_u(f)$,decomposed onto two different frequencies: (on the left) f_L; low frequency, (on the right) f_K; Karman frequency. The patterns are shown for selected wire angles of θ = 41°, 43°, 45°, 47°, 50°, 55°, and 180°. (Re_D = 10,000, d/D = 0.059)

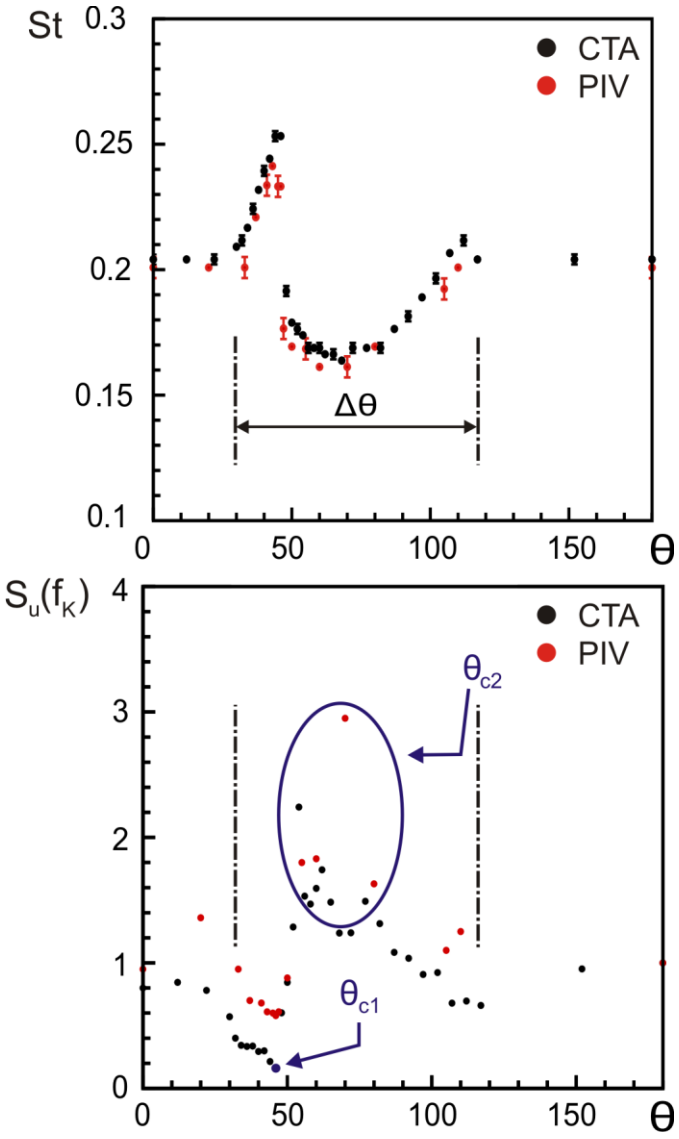

Figure 4.15 The Strouhal number, *St*, and the spectral amplitude of velocity fluctuations, $S_u(f_K)$, at the predominant (Karman) frequency are plotted against the wire angular location θ. Values are estimated from the velocity signals obtained from CTA and PIV measurements. (Re_D = 25,000, d/D = 0.059)

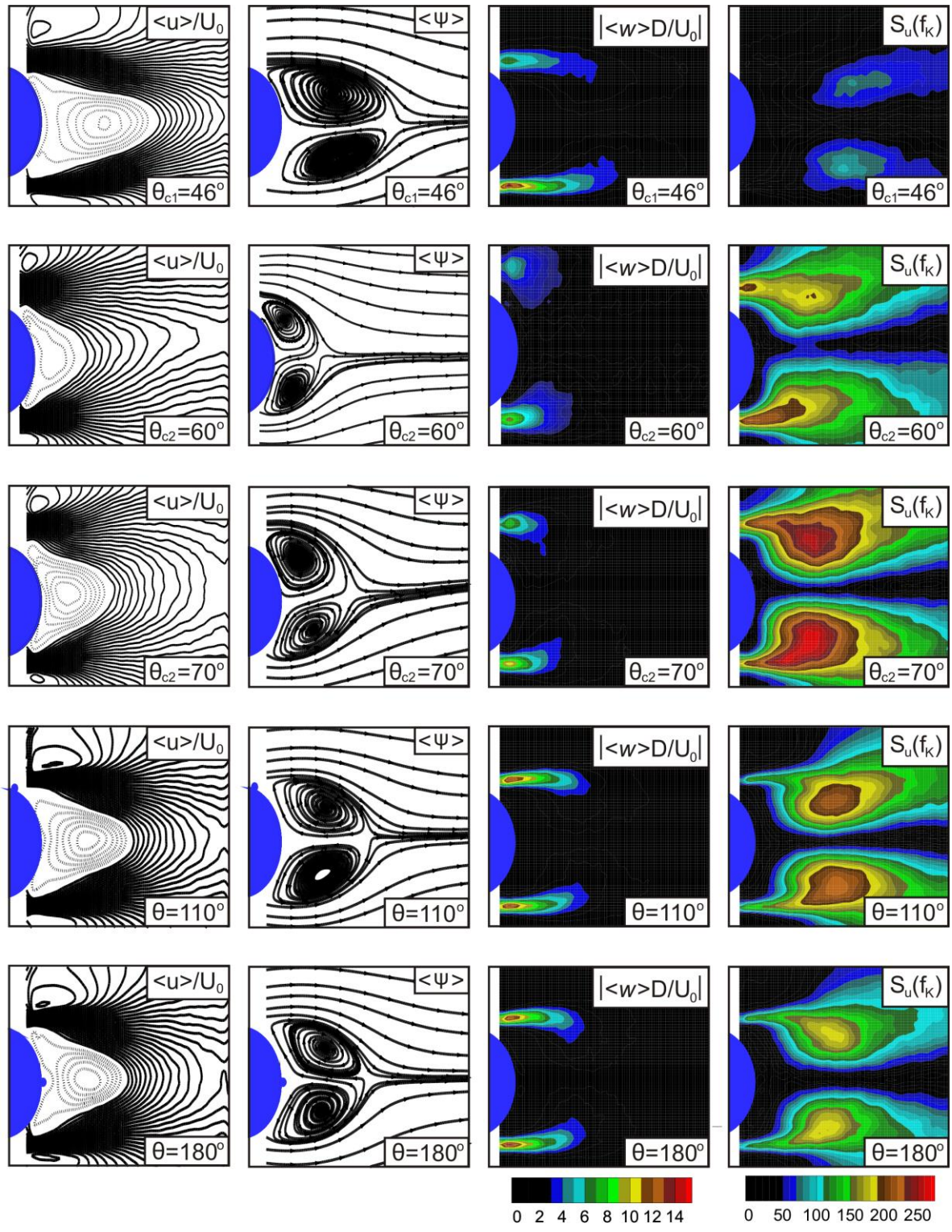

Figure 4.16 Iso-contours of time-averaged, normalized streamwise velocity components (<u>/U_0; first column), time-averaged streamlines (<ψ>; second column), time-averaged, normalized vorticity (|<w>D/U_0|; third column), and iso-contours of the amplitude of streamwise velocity spectra at Karman frequency ($S_u(f_K)$; fourth column). (Re_D = 25,000, d/D = 0.059)

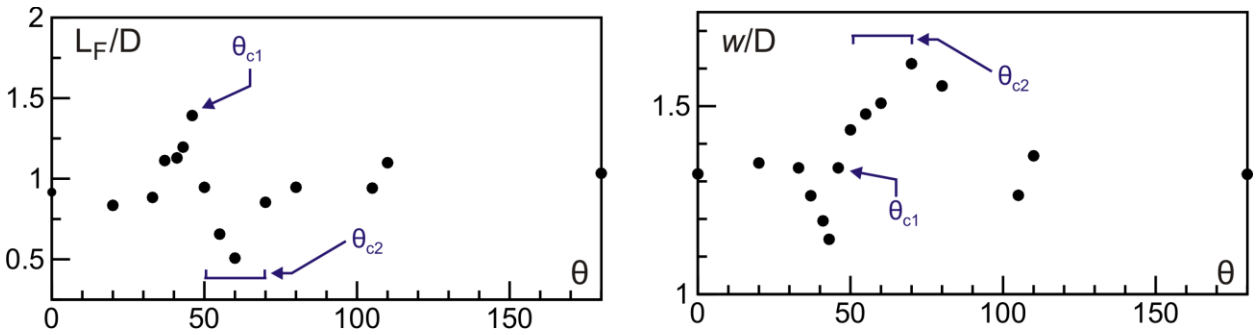

Figure 4.17 Vortex formation length and wake width as a function of wire angle. (Re_D = 25,000, d/D = 0.059)

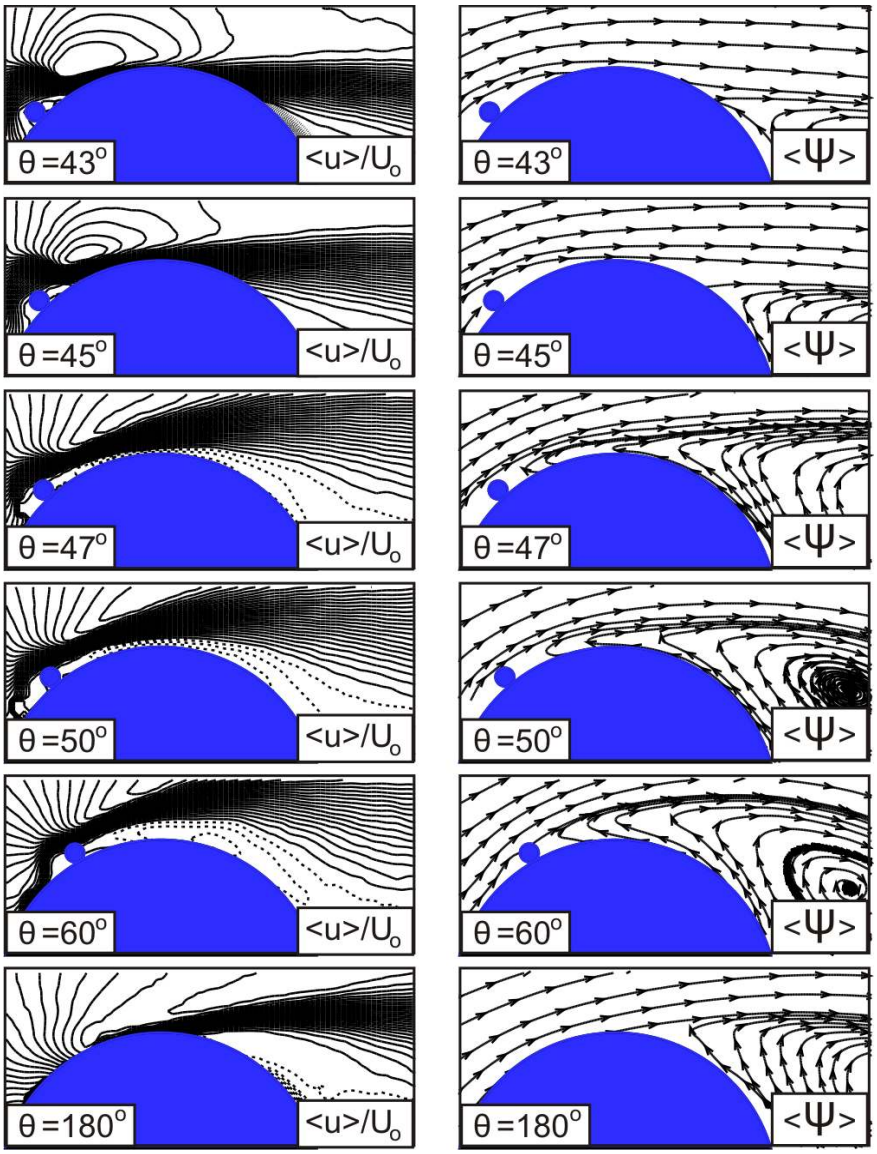

Figure 4.18 Iso-contours of time-averaged, normalized streamwise velocity components ($\langle u \rangle/U_0$; first column), time-averaged streamlines ($\langle \psi \rangle$; second column) in the shear-layer region at the wire-side of the cylinder. (Re_D = 25,000, d/D = 0.059)

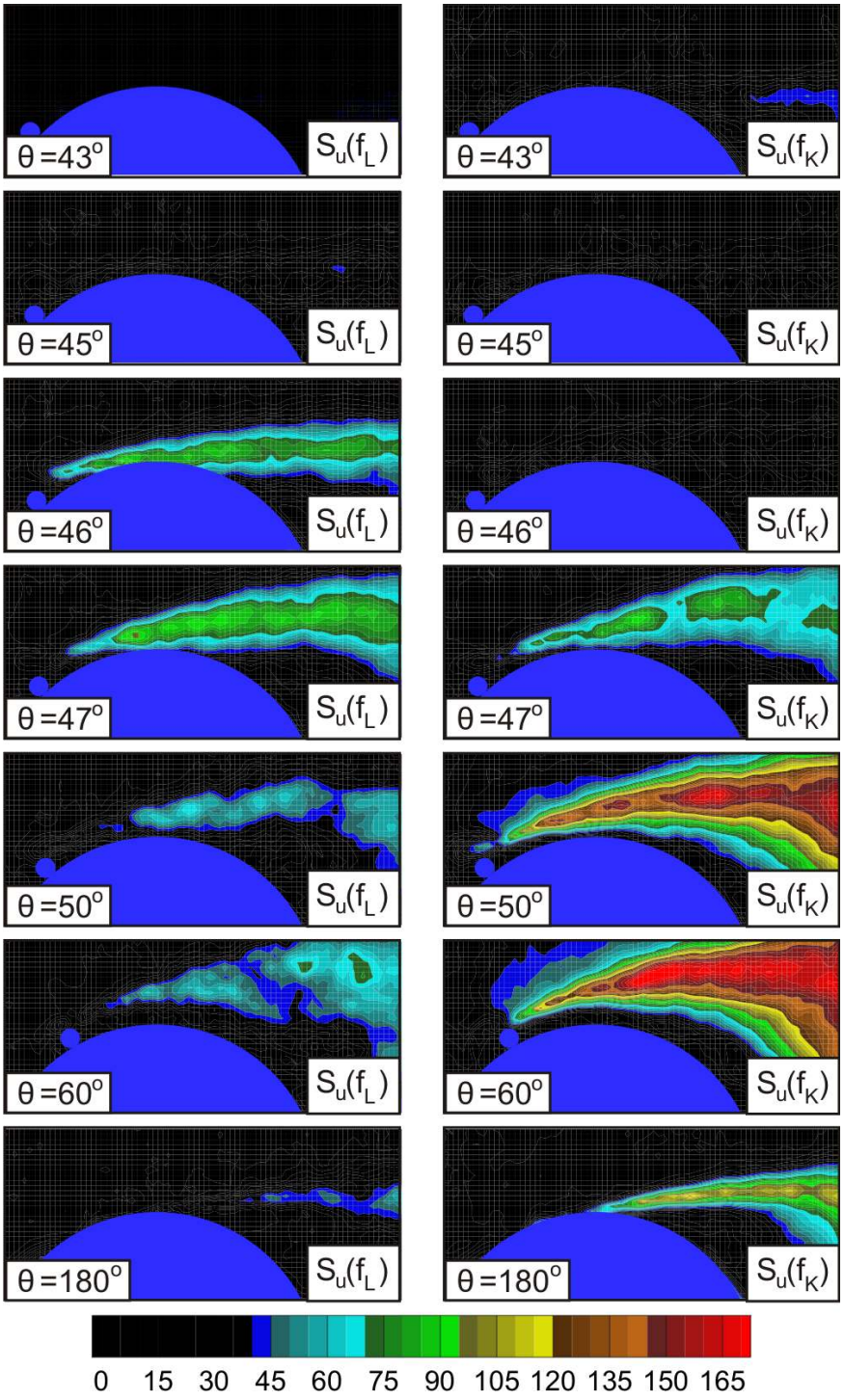

Figure 4.19 Contour patterns of constant amplitude of velocity spectra, $S_u(f)$,decomposed onto two different frequencies: (on the left) f_L; low frequency, (on the right) f_K; Karman frequency. The patterns are shown for selected wire angles of θ = 43°, 45°, 46°, 47°, 50°, 60°, and 180°. (Re_D = 25,000, d/D = 0.059)

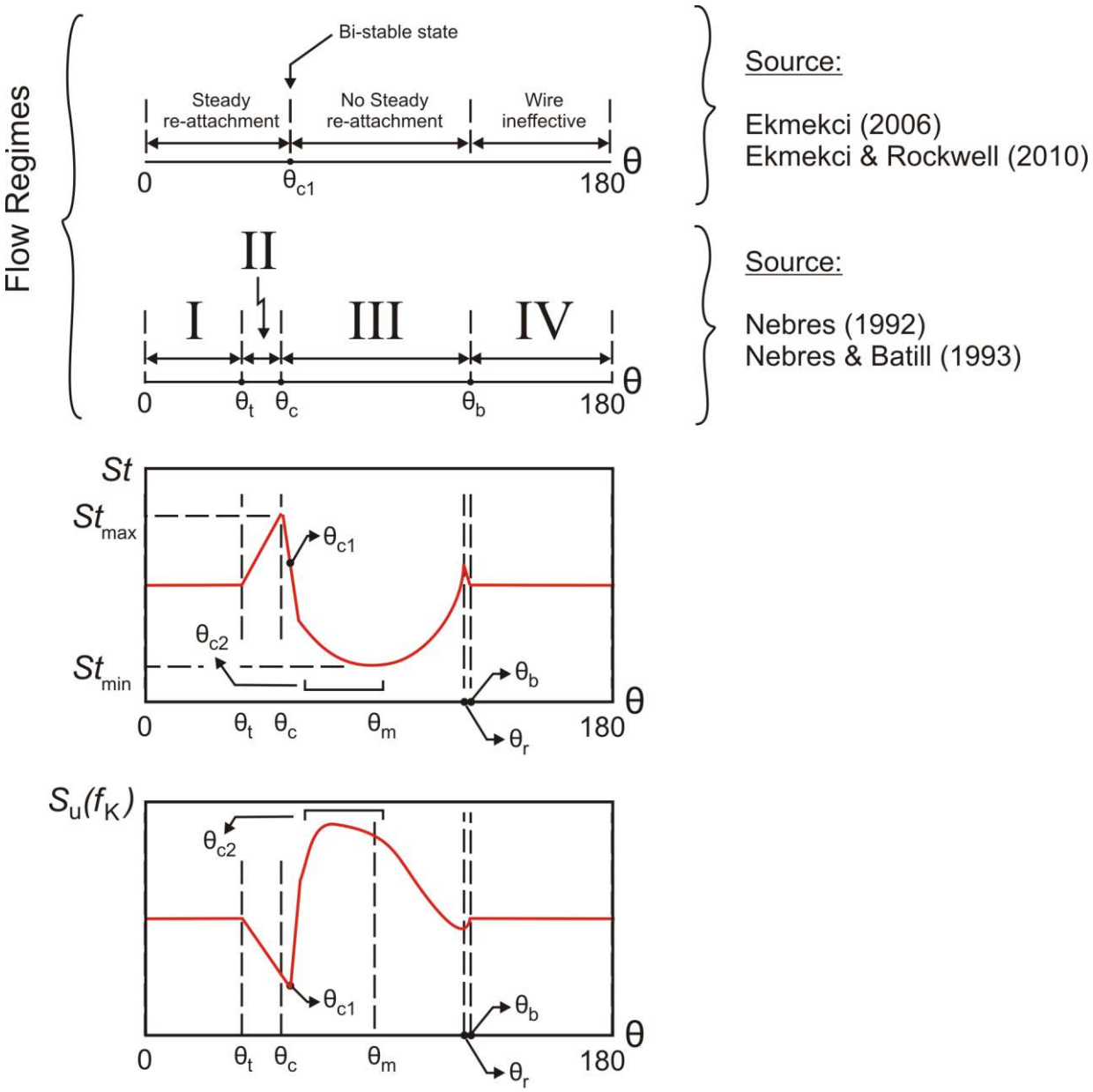

Figure 4.20 Two different sets of critical angles defined by Nebres and Batill (1993), and Ekmekci and Rockwell (2010) together with the associated flow regimes shown in the typical variations of St and $S_u(f_K)$ for a large-scale wire over the range of the wire angles, $0° \leq \theta \leq 180°$ (St-θ, and $S_u(f_K)$-θ plots are not scaled).

Chapter 5

Estimation of Strouhal number in the presence of a single, straight tripwire

In the previous chapter, the effects of a single, large-scale straight tripwire on the flow past a circular cylinder were summarized for different large-scale wire sizes and Reynolds numbers. Reynolds number and the wire size are shown to influence the values of the critical wire angles, and the boundaries of Strouhal number variation, but do not lead to changes in the patterns of the flow response. At this point, it is understood that the typical variation of Strouhal number, i.e. St-θ curves, is the focal point in understanding the flow response and associated changes in the flow features. Considering the practical significance, and the lack of efforts in the estimation of St-θ curves, this chapter presents a model for the estimation of the Strouhal number at a given wire angle (θ), Reynolds number (Re_D), and the wire size (d) applicable for a circular cylinder equipped with a single large-scale tripwire.

5.1. Introduction

The method presented in this chapter for the St-θ curves is constructed such that it requires only the wire size (d), the cylinder diameter (D), and Reynolds number (Re_D) as input from the user. The idea is to transform the parameter space of the problem for the St-θ curves from $St = f(d/D, Re_D, \theta)$ to $St = f(d/\delta, \theta)$, and facilitate the previously shown similarity in the wake response. This feature is considered as an advantage over the previously tested techniques by Nebres (1992) due to the method's robust nature since the flow features such as wake width, base pressure parameter, are not required as inputs from the user.

The estimation model is based on two foundations: *(i)* similarity in the variation of Strouhal number with the wire angle and *(ii)* the changes in the values of the critical wire angles and Strouhal number boundaries. The first foundation collapses the typical St-θ curves in a modified domain of Strouhal number (S^*) and wire angle (θ^*) such that the values of modified wire angles and modified Strouhal number do not vary for different wire sizes and/or Reynolds numbers. The

second foundation models the variation in the values of critical wire angles, and Strouhal number boundaries with respect to the non-dimensional perturbation size (d^*).

Figure 5.1 shows the block diagram for this estimation method. Initially, the non-dimensional perturbation size, $d^* = d/\delta$, is determined. Here, δ represents the unperturbed boundary layer thickness. The value of the boundary layer thickness is estimated using the Blassius method combined with the potential flow theory for the pressure distributions around the cylinder. The angular location at which the boundary layer thickness is determined is selected as $\theta = 45°$ because the pressure distribution obtained by the potential flow theory agrees well with the actual surface pressure measurements up to these angles. In addition, the value of the first critical angle (θ_{c1}) is close to and vary around 45°. Therefore, the ratio of $d/(\delta)_{\theta = 45°}$ will give a rough prediction of the wire-scale and determine if attenuation/amplification in Karman shedding can also be expected or not. After the non-dimensional perturbation size (d^*) is determined, the values of the critical angles and the boundaries of Strouhal number are estimated as the function of d^*. The estimated values of θ_t, θ_c, θ_m, θ_r, θ_b, St_{min}, St_{max} are indicated as a vector called μ. Note that this μ vector excludes the values of θ_{c1}, and θ_{c2} since they are shown to be related to the angular location of θ_c. After this stage, St-θ plots can be estimated using the similarity in the response of the wake, i.e. S^*-θ^*, together with the variables in μ.

The results are presented in three subsections in order to systematically construct an estimation model for St-θ curves at a given d/D and Re_D, and demonstrate its performance. The first part is related to the similarity of St-θ curves based on the experimental results. Using this similarity, a variable transformation from St-θ domain to the modified S^*-θ^* domain is used to obtain a general quantitative relationship between the non-dimensional vortex shedding frequency and the wire angle. After this variable transformation, the variation of the modified Strouhal number (S^*) as the function of the modified wire angle (θ^*) becomes independent of the wire size and Reynolds number. In the second part, it is shown that a linear function can be constructed for the prediction of the critical angles (θ_t, θ_c, θ_m, θ_r, θ_b) and boundaries for St (St_{max}, St_{min}) as a function of the dimensionless protrusion size of the wire d^*. In the last section, the results from the previous parts are combined, and the outcome of the estimation model is compared with the experimental data.

5.2. Part I: Similarity in the Near-Wake Response

The similarity in the wake response, which was previously discussed in Chapter 4, implies a general *St*-θ relationship, which is also shown by Nebres (1992) and Nebres and Batill (1993). Although the change in Reynolds number and wire size affect the values of the critical angles and the limits for the Strouhal number, a quantitative representation of the data can be obtained by a scaling process of *St*-θ curves so that resulting curve is independent of Re_D and *d/D*. A variable transformation has been applied to *St*-θ data using Eqn. (5.1),

$$S^*\left(\theta^*\right)=\begin{Bmatrix} \dfrac{St}{St_{ref}} & ;\theta^* \le d_1 \\ 1.0+c_1\dfrac{St-St_{ref}}{St_{\max}-St_{ref}} & ;d_1<\theta^* \le d_1+d_2 \\ 1.0+c_2\dfrac{St-St_{ref}}{\left|St_{\min}-St_{ref}\right|} & ;d_1+d_2<\theta^* \le d_1+d_2+d_3 \\ \dfrac{St}{St_{ref}} & ;d_1+d_2+d_3<\theta^* \le d_1+d_2+d_3+d_4+d_5 \end{Bmatrix} \tag{5.1}$$

where θ^* is given by Eqn. (5.2),

$$\theta^*=\begin{Bmatrix} d_1\dfrac{\theta}{\theta_t} & ;\theta \le \theta_t \\ \left(d_1\right)+d_2\dfrac{\theta-\theta_t}{\theta_c-\theta_t} & ;\theta_t<\theta \le \theta_c \\ \left(d_1+d_2\right)+d_3\dfrac{\theta-\theta_c}{\theta_r-\theta_c} & ;\theta_c<\theta \le \theta_r \\ \left(d_1+d_2+d_3\right)+d_4\dfrac{\theta-\theta_r}{\theta_b-\theta_r} & ;\theta_r<\theta \le \theta_b \\ \left(d_1+d_2+d_3+d_4\right)+d_5\dfrac{\theta-\theta_b}{180-\theta_b} & ;\theta_b<\theta \le 180 \end{Bmatrix} \tag{5.2}$$

Here, St_{ref} is the value of Strouhal number at $\theta = 180°$ wire location where the wire was shown to have insignificant effect (Nebres 1992, Nebres and Batill 1993). In these equations, c_1, c_2, d_1, d_2, d_3, d_4, and d_5 are arbitrary coefficients, and selected as $c_1=c_2=0.5$, $d_1=1$, $d_2=0.25$, $d_3=1.5$, $d_4=0.25$, and $d_5=1$.

Figure 5.2 shows the collapse of *St*-θ curves for five different Reynolds numbers onto the S^*-θ^* domain after the transformation applied to the data at a fixed wire size of *d/D* = 0.059 (data presented in Figure 4.8) using Eqns. (5.1) and (5.2). The critical angles (θ_t, θ_c, θ_m, θ_r, θ_b) used in

these equations are marked in Figure 5.2 at the boundaries of the regions denoted as I to V. These regions are associated with the following characteristics; in Region I ($0 \le \theta^* \le 1$), modified Strouhal number (S^*) stays constant at $S^* = 1$, or in other words $St = St_{ref}$. In Region II ($1 < \theta^* \le 1.25$), S^* increases linearly until it reaches $S^* = 1.5$. This is analogous to Strouhal number reaching to its maximum value (St_{max}), whose value depends on Re_D and d/D, but S^* does not. In Region III ($1.25 < \theta^* \le 2.75$), S^* follows a crater-like distribution until the modified wire angle $\theta^* = 2.75$ (or $\theta = \theta_r$). Within this crater, modified Strouhal distribution reaches to its minimum value of $S^* = 0.5$ (or in other words $St = St_{min}$) at the modified wire angle $\theta^* = 1.95$ (or $\theta = \theta_m$). In Region IV ($2.75 < \theta^* \le 3$), S^* linearly decreases until it reaches to $S^* = 1$ (or $St = St_{ref}$). Finally, modified Strouhal number stays constant at $S^* = 1$ in Region V ($3 < \theta^* \le 4$). The transformation given by Eqns. (5.1) and Eq. (5.2) ensures that the modified Strouhal number (S^*) stays within the range of $0.5 \le S^* \le 1.5$ over the modified wire angle range of $0 \le \theta^* \le 4$ for any St-θ curve at a given Re_D and d/D. The choice of the constants used in these equations don't change the nature of the abovementioned S^*-θ^* relationship.

The curve fit to the experimental data, defined by Eqn. (5.3)

$$S^*(\theta^*) = \begin{Bmatrix} 1.0 & \theta^* \le 1.0 \\ 1.9897\theta^* - 0.9771 & 1.0 < \theta^* \le 1.25 \\ 0.7635\theta^{*2} - 2.9610\theta^* + 3.3957 & 1.25 < \theta^* \le 2.75 \\ -0.3816\theta^* + 2.1431 & 2.75 < \theta^* \le 3.0 \\ 1.0 & 3.0 < \theta^* \le 4.0 \end{Bmatrix} \qquad (5.3)$$

is shown in Figure 5.2 as a solid line which represents the quantitative relationship between the modified Strouhal number (S^*) and the modified wire angle (θ^*). The average error between the estimated values of S^* using this curve fit in Eqn. (5.3) and the experimental data for S^* is given for all the wire sizes in Table 5.1. The error lies within the range of 3.2% - 6.0% for region II, 5.8% - 9.6% for region III, and insignificant for regions I, IV, and V. The overall error in S^*-θ^* with the use of the curve fit is 5.6%, 4.6% and 3.9% for $d/D = 0.029$, 0.039 and 0.059 respectively.

Table 5.1 Average error in the estimation of S^* for different wire sizes.

	θ^* range						
	I	**II**	**III**	**IV**	**V**	**I-V**	***d/D***
ε_{S^*}, [%]	0.5	4.3	9.6	0.2	0.2	5.6	0.029
	0.3	6.0	6.6	0.4	0.2	4.6	0.039
	0.3	3.2	5.8	0.4	0.1	3.9	0.059

5.3. Part II: Dependency of $\vec{\mu}$ on *d/δ*

Transformation of the data from *St*-θ domain to S^*-θ^* domain leads to a promising curve fit for S^* as a function θ^*, given by Eqn. (5.3), and represents the typical variation of Strouhal number within a reasonable error bound ($3.9\% \leq \varepsilon_{S^*} \leq 5.6\%$ as given in Table 5.1). This curve fit is independent of Re_D and *d/D*, and allows the prediction of the vortex shedding frequency with an inverse transformation from S^*-θ^* domain to *St*-θ domain once the critical angles and *St* boundaries are known. However, how these critical values can be predicted is not determined yet. In this subsection, the changes in the values of the critical angles, and the boundaries for Strouhal number (St_{max}, St_{min}) are analyzed in relation to varying Reynolds number and the wire size, and compared with the previously published data. This analysis is carried out such that a functional relationship is sought between the vector (μ) consisted of these problem variables as a function of the wire size and Reynolds number in the form of $\mu = [\theta_t, \theta_c, \theta_m, \theta_r, \theta_b, St_{max}, St_{min}] = f(d/D, Re_D)$.

At this point, Pi variables governing how the critical angles and Strouhal boundaries change for a single spanwise tripwire in the subcritical Reynolds numbers will be re-arranged from $\mu = f(Re_D, d/D)$ to $\mu = f(d/\delta)$ such that the effects of *d/D* and Re_D on the variables of μ are combined into a single parameter; $d^* = d/\delta$. This rearrangement of Pi variables ensures that an increase in either the Reynolds number or the wire size increases the value of the non-dimensional perturbation size. This is motivated from the similarity in the effects of increasing Reynolds number and wire size as described in Chapter 4, and reported by the previous researchers (Ekmekci and Rockwell 2010, Nebres 1992, Nebres and Batill 1993).

While determining the non-dimensional perturbation size ($d^* = d/\delta$), δ represents the boundary layer-thickness around the smooth cylinder at a circumferential location and is estimated by using the Blasius method given in Schlichting (1968) as described in detail by Nebres (1992). Originally, this procedure requires a surface pressure distribution around the cylinder for a given Re_D in absence of the tripwire in order to compute the boundary layer thickness. For this purpose, the potential flow theory is used for the pressure distribution ($c_P(\theta) = 1 - 4\sin^2\theta$) around the cylinder

in absence of the wire prior to flow separation so that surface pressure measurements are avoided in the model for its robustness. In addition, the angular location where the boundary layer thickness (δ) is estimated is selected as $\theta = 45°$. The predicted values of the boundary layer thickness for each Reynolds number considered in this study are given in Table 2 together with the results obtained from experimental pressure distributions where data is available. Comparison of these values shows a good agreement in the determination of the boundary layer thickness at this angular location ($\theta = 45°$).

Table 5.2 Estimated boundary layer thickness measurements based on two different methods. (1) Current measurements, (2) Measurements by Nebres (1992)

Re_D	$\delta_{theoritical}/D$, x10^3	$\delta_{experiment}/D$, x10^3
5,000	1.87	1.89 (1)
10,000	1.32	1.38 (1)
15,000	1.08	n/a
25,000	0.83	n/a
30,000	0.76	0.81 (2)

The values of the variables in the vector $\mu = [\theta_t, \theta_c, \theta_m, \theta_r, \theta_b, St_{max}, St_{min}]$ are given in Table 5.3 as a function of d/D, Re_D, and d/δ, where δ is determined from Table 5.2 using potential flow theory for pressure distributions. As the size of the perturbation with respect to the size of the boundary layer ($d^* = d/\delta$) increases, the range of the effective wire angles ($\Delta\theta = \theta_b - \theta_t$) and the degree of change in St ($St_{max} - St_{min}$) increase. In addition, the range of angles where Strouhal number increases at the beginning of its crater-like variation ($\theta_c - \theta_t$) also increase with the perturbation size (d^*). Since an increase in either the wire size (d/D) or Reynolds number (Re_D) mean an increase in the nondimensional perturbation size (d^*), these observations are consistent with the findings presented in Chapter 4 and those reported by Nebres (1992) and Nebres and Batill (1993).

In Figure 5.3, the values of the variables in the vector μ are plotted for an extending range of d^* for $1.4 \leq d^* \leq 20.3$ including the data from the current study (shown with black dots), and the data presented in Nebres (1992) and Nebres and Batill (1993) (blue dots). In the data of Nebres and Batill (1993), the values of St_{max} and St_{min} are not corrected for the blockage ratio (7.3%) of their experiments. However, the Strouhal number boundaries presented in this study (Table 5.3) are corrected for the blockage effects. For consistency, blockage correction is applied to the values of Strouhal numbers provided by Nebres (1992) and Nebres and Batill (1993) according the procedure given in App. B. In addition, the error in the determination of St_{max} and St_{min} in this study is calculated by applying Root-Sum-Square equation, described by Moffat (1988), as also

described in App. A. Estimated error levels for the Strouhal number (ε_{St}) are given in Table 2.4, and are 3.67%, 2.05%, 1.36%, 0.97%, and 0.88% of the reference value of $St_{ref} = 0.2$ at Re_D = 5,000, 10,000, 15,000, 25,000, and 30,000 respectively.

Table 5.3 Critical angles and the Strouhal number boundaries for all the experimental configurations in question.

$d^* = d/\delta$	Re_D	d/D	θ_t	θ_c	θ_m	θ_r	θ_b	θ_c-θ_t	θ_b-θ_t	St_{max}	St_{min}	St_{max}-St_{min}
1.550	5,000	2.90	43	47	69	103	108	4	65	0.215	0.175	0.040
2.084	5,000	3.90	33	41	69	103	108	8	65	0.214	0.168	0.046
2.192	10,000	2.90	43	47	69	103	108	4	65	0.215	0.175	0.040
2.685	15,000	2.90	43	53	69	103	108	10	65	0.248	0.176	0.072
2.948	10,000	3.90	39	45	69	103	103	6	64	0.221	0.168	0.053
3.154	5,000	5.90	32	40	68	107	107	8	75	0.214	0.161	0.053
3.466	25,000	2.90	35	51	69	103	108	16	73	0.246	0.172	0.072
3.611	15,000	3.90	33	47	69	103	103	15	71	0.243	0.168	0.075
3.797	30,000	2.90	35	51	69	103	108	18	75	0.248	0.169	0.079
4.460	10,000	5.90	32	44	68	112	122	12	90	0.235	0.168	0.067
4.661	25,000	3.90	30	47	69	103	108	17	78	0.251	0.168	0.083
5.106	30,000	3.90	30	47	69	103	108	17	78	0.251	0.168	0.083
5.462	15,000	5.90	34	46	68	112	117	12	83	0.251	0.168	0.083
7.052	25,000	5.90	30	46	68	112	117	16	86	0.253	0.163	0.090
7.725	30,000	5.90	32	44	68	112	117	12	85	0.253	0.163	0.090

Based on the variation of the variables in μ vector, given in Figure 5.3 for $1.4 \le d^* \le 20.3$, it can be seen that an increase in d^* leads to a decrease in the values of θ_c, θ_t, and St_{min}, and an increase in the values of θ_r, θ_b, and St_{max}. The value of θ_m stays relatively constant around 68° to 69°. These general trends, identified in Figure 5.3, are represented with a linear function of d^* for each variable (blue dashed lines in Figure 5.3) and given by Eqn. (5.4),

$$\begin{bmatrix} \theta_t \\ \theta_c \\ \theta_m \\ \theta_r \\ \theta_b \\ St_{\max} \\ St_{\min} \end{bmatrix} (d^*) = \begin{bmatrix} 42.6 \\ 51.7 \\ 69.8 \\ 99.2 \\ 103.3 \\ 0.232 \\ 0.174 \end{bmatrix} + \begin{bmatrix} -1.18 \\ -0.94 \\ -0.017 \\ 1.56 \\ 1.65 \\ 0.00117 \\ -0.00184 \end{bmatrix} (d^*) \qquad (5.4)$$

5.4. Part III: Construction and Application of the Estimation Model

In the previous sections, a quantitative relationship has been established between the modified Strouhal number (S^*) and the modified wire angle (θ^*). This relationship was shown to be valid for any wire size and Reynolds number considered in this study within an error bound of $3.9\% \le \varepsilon_{S^*} \le$

5.6%. This enables the prediction of vortex shedding frequency as long as the critical angles and Strouhal boundaries are known for a given wire size, and Reynolds number configuration. As a next step, the variations of the critical angles, the maximum and minimum values of Strouhal number attainable with a single large-scale wire are evaluated as the function of the nondimensional perturbation size (d^*). In this section, previously presented results will be combined and the model will be used to estimate the Strouhal number variation with θ for each case considered herein.

The roadmap of the current proposed model is given in Figure 5.1 as discussed previously. Initially, the non-dimensional surface protrusion size (d^*) is found using the pressure distribution obtained from the potential flow theory with the procedure given in App. C for a given Re_D and d/D value. After the variables of μ are computed using Eq. (5.4), the wire angle range can re-organized in the modified wire angle axis such that $0° \le \theta \le 180°$ can be converted to $0 \le \theta^* \le 4$, and S^* can be calculated using Eqns. (5.2) and Eqn. (5.3) respectively for the desired wire angles. Finally, St can be calculated using Eqn. (5.5) where $c_1 = c_2 = 0.5$.

$$St = \begin{Bmatrix} St_{ref} & \theta \le \theta_t \\ \left(St_{\max} - St_{ref}\right)\left(S^* - 1\right)/c_1 + St_{ref} & \theta_t < \theta \le \theta_c \\ \left|St_{\min} - St_{ref}\right|\left(S^* - 1\right)/c_2 + St_{ref} & \theta_c < \theta \le \theta_r \\ St_{ref} & \theta_r < \theta \le 180 \end{Bmatrix} \qquad (5.5)$$

The average error in the estimated values of St, ε_{St}, can be observed in Figure 5.4(a). The average error lies somewhere between 1.8%-6.2% of the reference Strouhal number, i.e. $St(\theta = 180°)$. Three major contributing factors to the error of this model can also be identified. One of them involves the error in the estimation of the critical angles, especially θ_t and θ_c, resulting in offset of St values along the θ axis. The second part of the error comes from the error in the estimation of St_{max}, leading to an over-estimation of St. While the former situation is exemplified in Figure 5.5(c) for $Re_D = 5{,}000$ and $d/D = 0.059$ ($d^* = 3.15$), a representative case of the latter is given in Figure 5.4(b) for $Re_D = 10{,}000$ and $d/D = 0.029$ ($d^* = 2.19$). Estimation of St within the crater-like pattern can also contribute to the overall error in the estimation since the error levels for S^*-θ^* curve fit for region III, given in Table 5.1, ranges between 5.8%-9.6%. In Figure 5.4(d), an example of accurate estimation is given for $Re_D = 15{,}000$ and $d/D = 0.059$ ($d^* = 5.46$). The average error for these three cases are 2.95%, 6.16%, and 1.86% for Figure 5.4(b), 5.4(c), and 5.4(d) respectively.

5.5. Chapter Conclusions

Inspired by the similarity of the wake response to the tripwire (as discussed in Chapter 4), efforts have been put forward in order to estimate the vortex shedding frequency as a function of wire angle, i.e. St-θ curves. This proposed estimation model requires only the wire size (d), the cylinder diameter (D) and the Reynolds number (Re_D) as inputs from the user, and consists of two major parts.

The first portion of the model applies a variable transformation to the variation of the Strouhal number with the wire angle for each wire size and Reynolds number. This variable transformation collapses the experimental data onto a single curve defined in the S^*-θ^* domain which is independent of the wire size and Reynolds number, where S^* and θ^* represent the modified Strouhal number and the modified wire angle respectively.

The second part of this model involves the estimation of a vector containing the problem variables such as the critical angles and the boundaries of the Strouhal number, i.e. $\mu = [\theta_t, \theta_c, \theta_m, \theta_r, \theta_b, St_{max}, St_{min}]$. These variables are found to be a linear function of the non-dimensional perturbation size, $d^* = d/\delta$. Here, the symbol δ represents the boundary layer thickness at the angular location of $\theta = 45°$ in absence of the wire, and is estimated by using the Blassius method combined with the potential flow theory required for the surface pressure distribution at any given Reynolds number. Application of the established model on the cases investigated during this study, and comparison of the results with the experimental data reveal an average error of 1.8-6.2% on St-θ plots. Although this estimation model is a novel technique and associated errors are low for its application, three error sources have been identified: *(i)* the error in the estimation of the critical angles (especially θ_t and θ_c) leading to the horizontal shift of the estimated St-θ curves, *(ii)* the error in the estimation of the St_{max} value leading to the over- or under-estimation of the increase in the Strouhal number for the wire angle range of $\theta_t \leq \theta \leq \theta_c$, and *(iii)* the average error of the curve-fit to the S^*-θ^* domain.

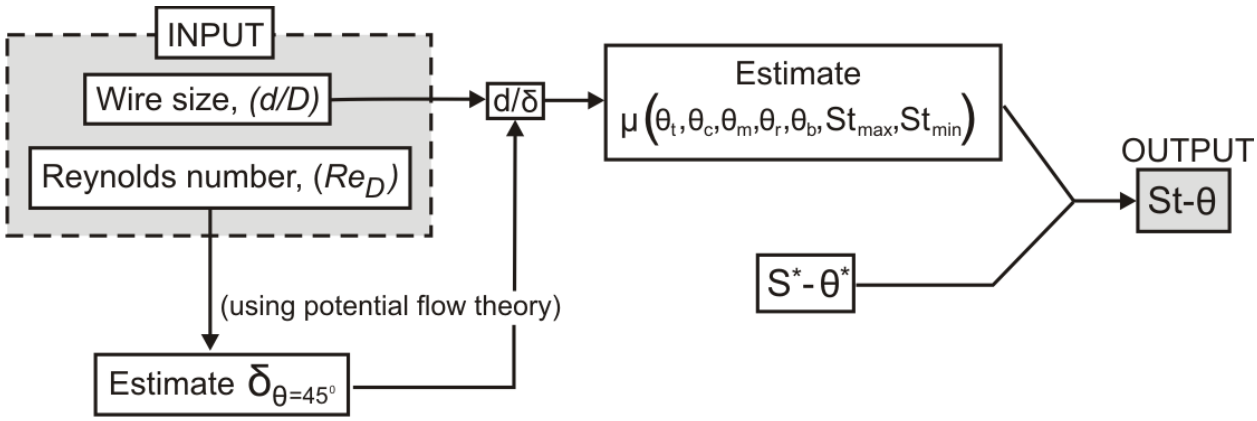

Figure 5.1 Block diagram of the estimation model for the vortex shedding frequency as the function of the wire angle.

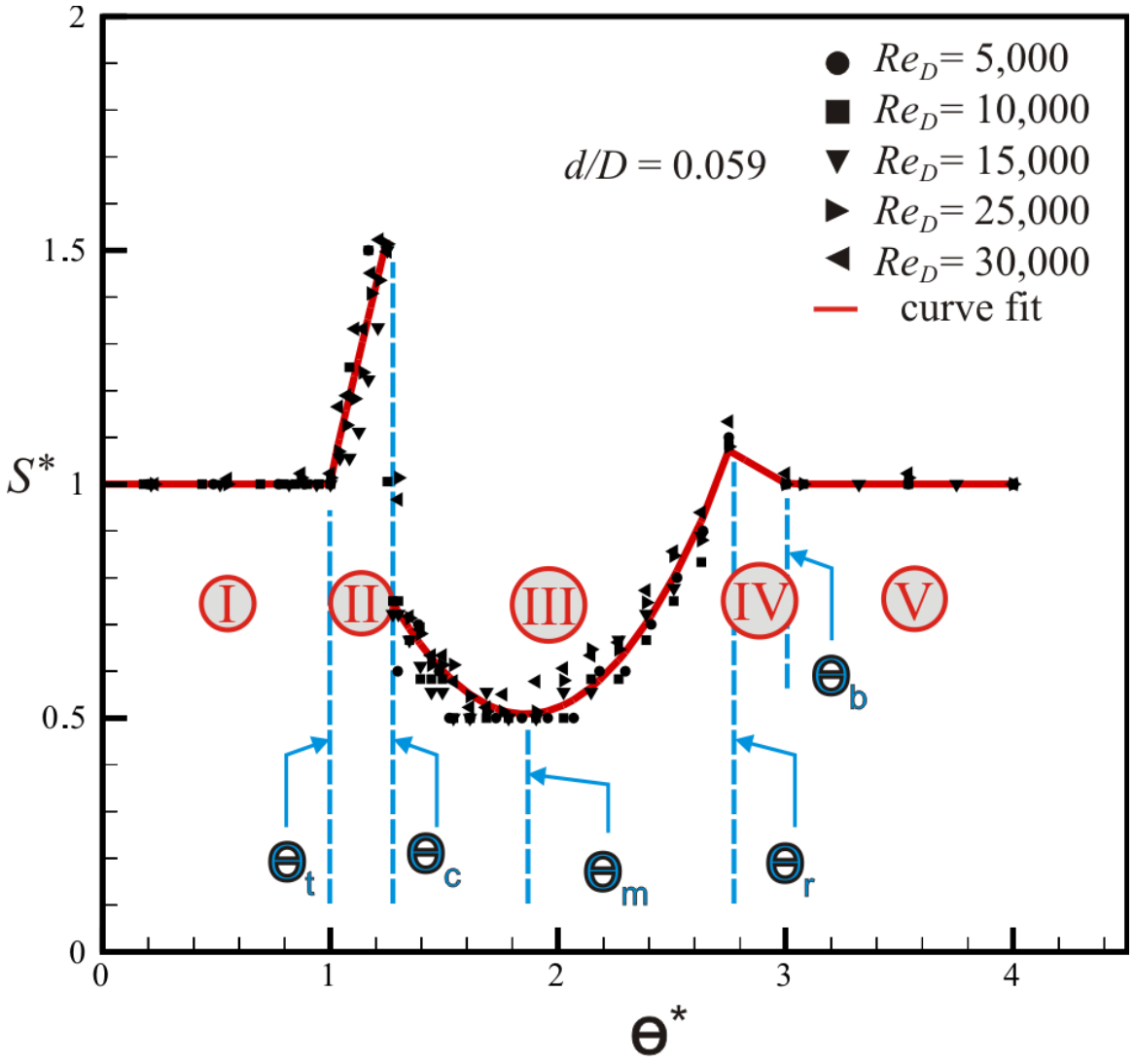

Figure 5.2 S^*-θ^*plot for various Re_D and a fixed d/D.

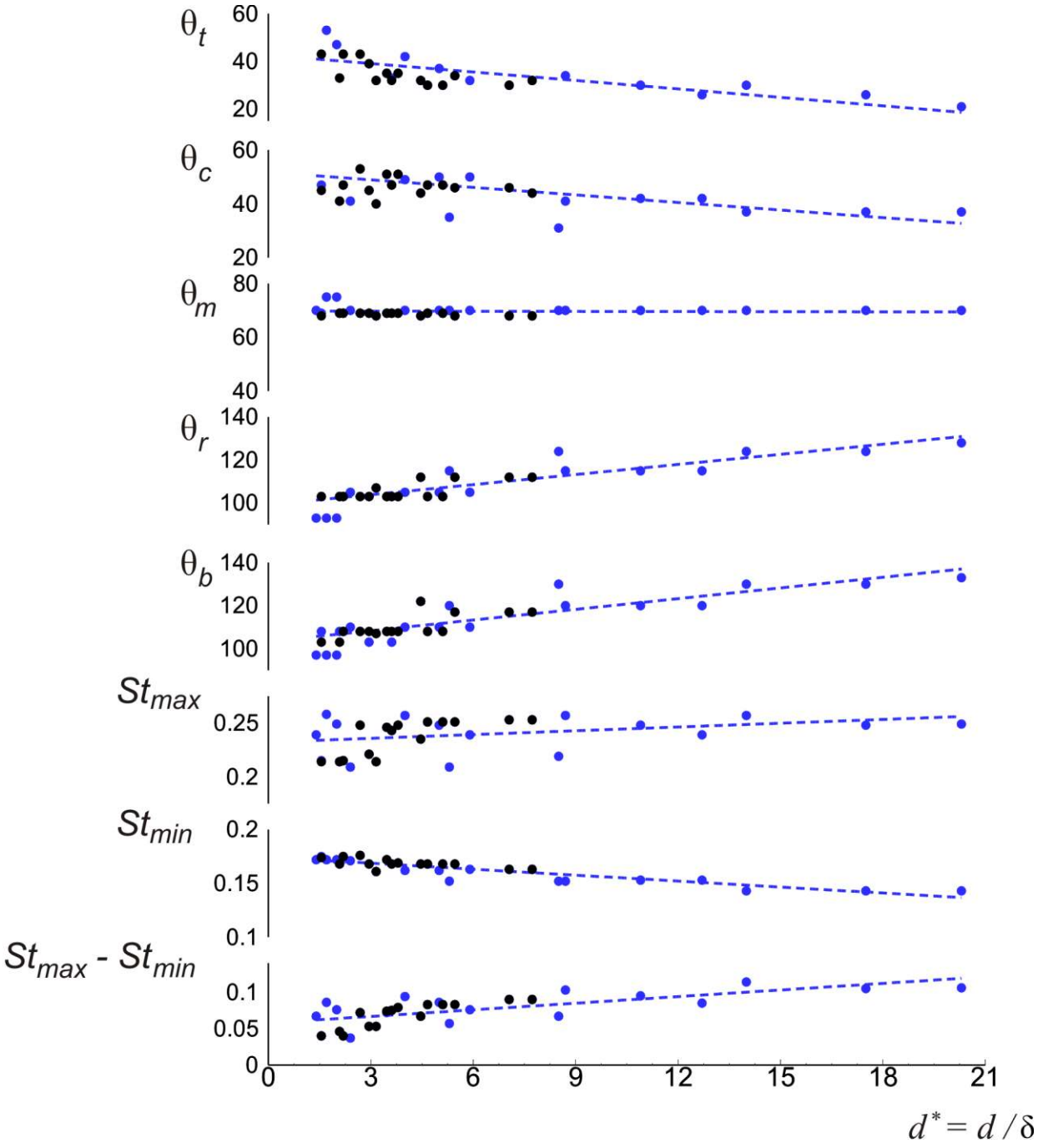

Figure 5.3 Distribution of μ variables over d/δ (● current study, ● Nebres and Batill 1993).

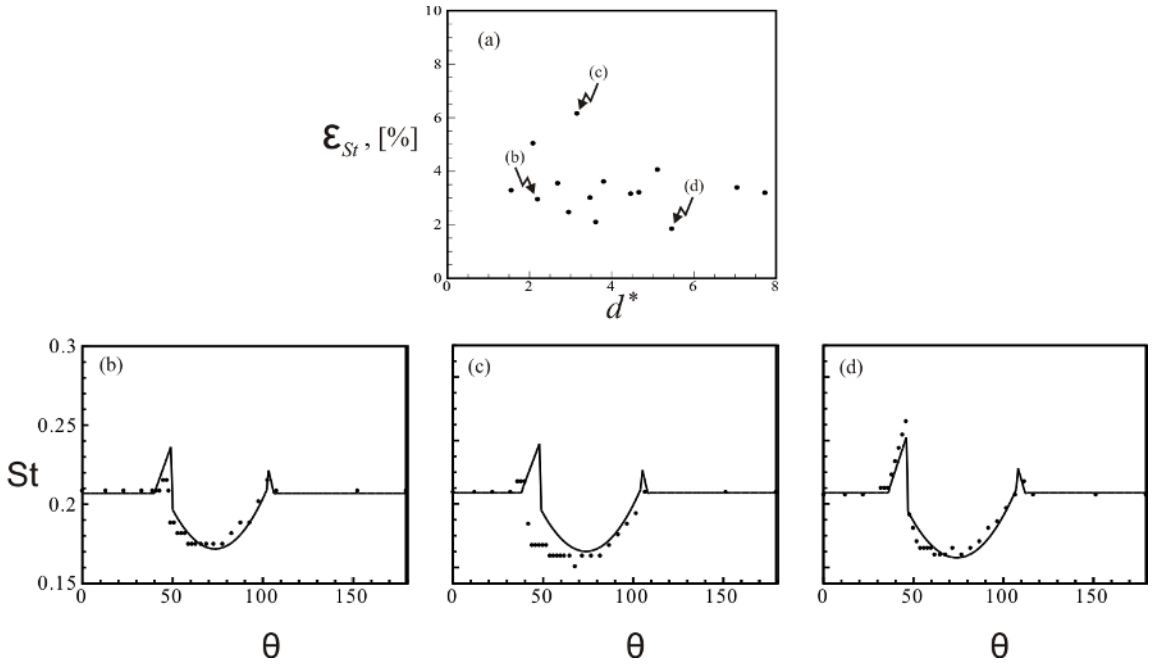

Figure 5.4 Error analysis on the estimation model: (a) Average error for the estimated values of *St* as a function of d^* = d/δ, (b)-(d) Strouhal values as a function of θ; • experimental — estimation. (b) Re_D = 10,000, d/D = 0.029, d/δ = 2.19, (c) Re_D = 5,000, d/D = 0.059, d/δ = 3.15, and (d) Re_D = 15,000, d/D = 0.059, d/δ = 5.46.

Chapter 6

Concluding Remarks / Recommendations for Future Research

In this dissertation, control of the flow past a circular cylinder has been studied with the use of a single tripwire on the surface of a cylinder. The tripwire is stretched parallel to the longitudinal axis of the cylinder. Prior to the investigation of flow control via the tripwire, the junction flow characteristics and the degree of two-dimensionality in the cylinder wake have been studied in absence of the wire. The use of an endplate with a sharp leading edge on each end of the cylinder is determined as the appropriate experimental setup in promotion of the quasi two-dimensional vortex shedding. Using this experimental setup, the effects of the wire have been experimentally evaluated as a function of the wire angle with respect to the oncoming flow direction for different wire sizes and Reynolds numbers. For a detailed understanding of the flow response to this two-dimensional flow perturbation, the investigation was carried out using various experimental techniques, such as Particle Image Velocimetry (PIV), Constant Temperature Anenometry (CTA), and hydrogen bubble flow visualization. Throughout this study, the wire-to-cylinder diameter ratios were selected as d/D = 0.029, 0.039, and 0.059. At the sub-critical range of Reynolds numbers studied herein ($5{,}000 \leq Re_D \leq 30{,}000$), all wires were determined to be a large-scale perturbation since the size of each wire was greater than the thickness of the boundary layer growing around the smooth cylinder.

One of the novel findings of this dissertation is the existence of two critical angular locations for the implementation of the large-scale wire for varying Reynolds numbers and wire sizes. These locations are denoted as θ_{c1} and θ_{c2} in accord with the existing literature. θ_{c1} is recognized as the location on the cylinder surface where placing a wire alleviates the peak spectral amplitude of velocity fluctuations the most with notable irregularities. This critical location is identified as a single angle on the cylinder surface. On the other hand, θ_{c2} is associated with a drastic increase in the peak spectral amplitude and is found to encompass a range of angular locations on the cylinder surface, extending roughly from 50° to 70°. While the range of θ_{c2} locations is unaffected from the

Reynolds number and wire size, the value of θ_{c1} is dependent on these parameters. For a given Reynolds number, increasing the wire size led to a decrease in the value of θ_{c1}. However, for a given wire size and until a Reynolds number of 15,000, increasing the Reynolds number increases the value of θ_{c1}. From Re_D = 15,000 to 30,000, θ_{c1} is found to be independent of the Reynolds number.

Another new understanding on the flow past a circular cylinder in presence of a single large-scale tripwire is the resumption of the rhythmic development of Karman vortex clusters for short periods of the time when the wire is placed at θ_{c1}. However, for the majority of the time, a no-shedding phase was observed consistent with the existing literature. Another observation in relation to the effect of a wire at the θ_{c1} location was that during the times when the Karman shedding was disrupted, the near-wake bubble extended considerably in the streamwise direction. As for the θ_{c2}, a large-scale wire at this angular location leads to significant increase in the coherence and strength of the Karman vortices, and the near-wake bubble became significantly contracted in accord with the existing literature.

This study also shows that the spectral amplitude and frequency of the velocity fluctuations corresponding to the Karman instability can be controlled by a single wire only if that wire is located over a certain range of angular locations ($\Delta\theta$), the value of which was found to depend on the Reynolds number and wire size. Within this range of angles, with increasing wire angular location θ, the shedding frequency typically underwent a crater-like variation with a slight rise at the beginning and end of this variation, which is in perfect agreement with the existing literature. As a novel finding, the spectral amplitude at the Karman frequency is observed to follow a change that has roughly an inverse association with the frequency variation.

Inspired by the similarity of the wake response to the tripwire, a model is established for the estimation the vortex shedding frequency as a function of wire angle, i.e. St-θ curves. This proposed estimation model, which is another contribution to the literature, requires only the wire size (d), the cylinder diameter (D) and the Reynolds number (Re_D) as inputs from the user. In this model, there are two foundations: *(i)* a quantitative relationship between the modified Strouhal number (S^*) and the modified wire angle (θ^*) which is independent of the Reynolds number and the wire size, and *(ii)* the linear variation of the critical wire angular locations and Strouhal number boundaries with the non-dimensional perturbation size (d^*). Application of the established model on the cases investigated during this study, and comparison of the results with the experimental

data reveal an average error between 1.8% and 6.2% on St-θ plots. The sources of the errors in the estimation of the vortex shedding frequency have also been identified.

While the results of this dissertation improve our understanding on the degree of flow control with a single large-scale wire, the application of the findings for the control of flow-induced forces (and vibrations) needs further discussion. This discussion is given in App. D.

6.1. Recommendations for Future Research

The results of the current study, together with the important findings of Nebres (1992), Nebres and Batill (1993), Ekmekci (2006) and Ekmekci and Rockwell (2010), clearly demonstrate how the near-wake flow responds to a single wire for different wire sizes and sub-critical Reynolds numbers. This study also presents a novel method to estimate St-θ curves. Aside from the potential use of the results, as discussed above, the application of a single, tripwire on the surface of a circular cylinder is mainly driven by the search for a thorough understanding of the flow structures due to the surface protrusion, and is interpreted as a guide for more complex flow control problems. These configurations can take the form of multiple tripwires stretched parallel to the cylinder axis, or the form of single (or multiple) wires wound around the cylinder in helical orientations. While the former case still constrains the problem to a two-dimensional frame, the latter becomes a three-dimensional flow perturbation. The following is a discussion on the unresolved issues and potential research topics on the use of trip wires.

(i) Single, straight tripwire: The variation of the vortex shedding frequency, strength and coherency of Karman shedding and the flow structures as a function of the wire angle are shown to undertake trends similar in each case considered for different wire sizes and Reynolds numbers as long as the wire is a large-scale flow perturbation. When compared to the data represented by Nebres and Batill (1993), the current study bases these results to relatively low values of the non-dimensional perturbation size of d^* ($1.55 \leq d^* \leq 7.72$) where $d^*=d/\delta$. However, the data reported by Nebres (1992) also show similar trends in the variation of the critical angles for a wider range; $1.40 \leq d^* \leq 20.30$. Still, the upper limit of this perturbation size up to which the flow response undertakes similar flow states is still questionable. Future research should focus more on the variation of the wire sizes larger than $d/D = 0.142$, and the Reynolds numbers greater than $Re_D =$ 40,000 (up to $Re_D \approx 300{,}000$). The constraint on Reynolds number ensures the formation of a laminar boundary layer around the plain cylinder, and thus the transition in the re-attached

boundary layer after the wire might still occur. Another note on the upper limit of the wire size is the limiting case for $d/D \geq 1$ where the tripwire size (d) is larger than or equal to the main cylinder (D). In this case, the roles might change; the wire can be considered as the main cylinder with the diameter d, and the main cylinder will become the wire with a wire size of D since both of the structures have circular cross-sectional geometries.

(ii) Multiple, straight tripwires: This research area can be viewed as a mid-step between single straight wires to multiple helical wires. Interestingly in this problem, each wire would be at a certain wire angle with respect to the free-stream direction, and the possibility of superimposing the results from a single wire case onto the case of multiple wires is quite an interesting question.

(iii) Helical wires: Let's consider the helical configuration with one-wire start wound around the cylinder with a certain pitch (P), which is defined as the spanwise distance traveled during one revolution of the wire around the cylinder surface. As long as the pitch-to-cylinder diameter (P/D) is smaller than the aspect ratio of the cylinder (L/D), the wire will sweep a wire angle range of 2π, and, for example, pass through the first critical angle (θ_{c1}) twice per pitch. Since the effect of the wire at a certain wire angle is known from the research on a single straight wire, the comparison of the flow features for a helical wire (three-dimensional flow constrained by the whole cylinder) with the straight wire case (flow within the cross-sectional plane) would be an important milestone. In particular, the spanwise distribution of flow structures and how Karman vortices link with each other and/or interact with the spanwise secondary instabilities would be interesting.

References

Adrian R.J., 1991, “Particle-Imaging techniques for experimental fluid mechanics”, *Annu. Rev. Fluid Mech.,* **23**, 261-304.

Adrian R.J., 2005, “Twenty years of particle image velocimetry”, *Experiments in Fluids*, **39**, 159-169.

Alam M.M., Zhou Y., Zhao J.M., Flamand O., Boujard O., 2010, "Classification of the tripped cylinder wake and bi-stable phenomenon", *International Journal of Heat and Fluid Flow*, **31**, 545-560.

Anderson Jr.J.D., 2001, *Fundamentals of Aerodynamics 3rd Edition*, McGraw-Hill Books.

Asanuma T., Takeda S., 1965, “A study on the flow visualization by the hydrogen-bubble method”, Bulletin of JSME, **8**(32), 599-608.

Baker C.J., 1978, “Vortex flow around the bases of obstacles”, *Ph.D. Thesis*, Cambridge University.

Baker C.J., 1979, "The laminar horseshoe vortex", *J. Fluid Mech.*, **5**(2), 347-367.

Baker C.J., 1980, "The turbulent horseshoe vortex", *Journal of Wind Engineering and Industrial Aerodynamics*, **6**, 9-23.

Baker C.J., 1985, "The position of points maximum and minimum shear stress upstream of cylinders mounted normal to flat plates", *Journal of Wind Engineering and Industrial Aerodynamics*, **18**, 263-274.

Bearman P.W., 1965, "Investigation of the flow behind a two-dimensional model with a blunt trailing edge and fitted with splitter plates", *J. Fluid Mech.*, **21**(2), 241-255.

Bearman P.W., 1967, “On vortex street wakes”, *J. Fluid Mech.*, **28**(4), 625-641.

Bruun H.H., 1996, “Hot-film anemometry in liquid flows”, *Meas. Sci. Technol.*, **7**, 1301-1312.

Blackmore, A., 2011, “The use of endplates for a cylinder in the sub-critical flow regime”, *M.Sc. Thesis*, University of Toronto Institute for Aerospace Studies.

Chyu, C.K., Rockwell, D., 2002, "Near-wake flow structure of a cylinder with a helical surface perturbation", *Journal of Fluids and Structures*, **16**(2), 263-269.

Clayton B.R., Massey B.S., 1967, “Flow visualization in water: a review of techniques”, *J. Sci. Instrum.,* **44**, 2-11.

Cowdrey C.F., Lawes J.A., 1959, "Drag measurements at high Reynolds numbers of a circular cylinder fitted with three helical strakes", *Nat.Phys. Lab.*, Teddington, UK, Aero rep. No. 384.

Curle N., 1962, "*The laminar boundary layer equations*", Oxford Press.

Davenport W.J., Simpson R.L., 1990, "Time-dependent and time-averaged turbulence structure near the nose of a wing body junction", *Journal of Fluid Mechanics*, **210**, 23-55.

Deng G.B., Piquet J., 1992, "Navier Stokes computations of horseshoe vortex flows", I*nternational Journal for Numerical Methods in Fluids*, **15**, 99-124.

Dong S., Karniadakis G.E., Ekmekci A., Rockwell D., 2006, "A combined direct numerical simulation-particle image velocimetry study of turbulent near wake", *J. Fluid Mech.*, **569**, 185-207.

ELD Inc., 2009. Water Channel User Manual.

Eisenlohr H., Eckelmann H., 1989, "Vortex splitting and its consequences in the vortex street wake of cylinders at low Reynolds numbers", *Physics of Fluids A*, **1**, 189-192.

Ekmekci A., 2006, "Control of the near-wake of a circular cylinder: effects of surface disturbances", *Ph.D. Dissertation*, Dept. of Mechanical Engineering and Mechanics, Lehigh University.

Ekmekci A., Rockwell D., 2010, "Effects of a geometrical surface disturbance on flow past a circular cylinder: a large-scale spanwise wire", *J. Fluid Mech.*, **665**, 120-157.

Ekmekci A., Rockwell D., 2011, "Control of flow past a circular cylinder via a spanwise surface wire: effect of the wire scale", *Experiments in Fluids*, **51**, 753-769.

Escauriaza C., Sotiropoulos F., 2011a, "Reynolds number effects on the coherent dynamics of the turbulent horseshoe vortex system", *Flow, Turbulence, and Combustion*, **86**, 231-262.

Escauriaza C., Sotiropoulos F., 2011b, "Lagrangian model of bed-load transport in turbulent junction flows", *J. Fluid Mechanics*, **666**, 36-76.

Every M.J., King R., Weaver D.S., 1982, "Vortex-excited vibrations of cylinders and cables and their suppression", *Ocean Engineering*, **9**(2), 135-157.

Fage A., Johansen F., 1927, "The structure of vortex streets". *A.R.C. Reports and Memoranda* No 1143.

Fage A., Warsap J., 1929, "The effects of turbulence and surface roughness on the drag of a circular cylinder", *British Aero. Res. Comm.*, R.&M. No.1283.

Fox T.A., West G.S., 1990, "On the use of endplates with circular cylinders", *Experiments in Fluids*, **9**, 237-239.

Fujita, H., Takahama, H., Kawai, T., 1985, "Effects of tripwires on heat transfer from a circular cylinder in cross flow (1st report, the pressure distribution around the cylinder and the drag coefficient)", *Bulletin of JSME* **28** (235), 80-87.

Gand F., Deck S., Brunet V., and Sagaut P., 2010, "Flow dynamics past a simplified wing-body junction", *Physics of Fluids*, **22**, 115111.

Gartshore I.S., Khanna J., Laccinole S., 1979, "The effectiveness of vortex spoilers on a circular cylinder in smooth and turbulent flow", *5th Intern. Conference Wind Engineering*, Fort Collins, Colorado.

Gharib M., 1996, “Perspective: The experimentalist and the problem of turbulence in the age of supercomputers”, *Journal of Fluid Engineering*, **118**, 233-242.

Gaster M., 1969, "Vortex shedding from slender cones at low Reynolds numbers", *J. Fluid Mech.*, **38**, 565-576.

Gerrard J.H., 1966, "The mechanics of vortex formation region of vortices behind bluff bodies", *J. Fluid Mech*. **25**(2), 401-413.

Gerrard J.H., 1978, "The wakes of cylindrical bluff bodies at low Reynolds numbers", *Phil. Trans. Roy. Soc. Lond. A*, **288**, 351-382.

Gerich D., Eckelmann H., 1982, "Influence of end plates and free ends on the shedding frequency of circular cylinders", *J. Fluid Mech.*, **122**, 109-121.

Greco J.J., 1990, “The flow structure in the vicinity of a cylinder-flat plate junction: flow regimes, periodicity, and vortex interactions”, *M.Sc. Thesis*, Lehigh University.

Griffin O.M., 1978, “A universal Strouhal number for the ‘locking-on’ of vortex shedding to the vibrations of bluff cylinders”, *J. Fluid Mech.*, **85**, 591-606.

Hama F.R., 1962, “Streaklines in a perturbed shear flow”, *Physics of Fluids*, **5**(6), 644-650.

Hammache M., Gharib M., 1989, "A novel method to promote parallel vortex shedding in the wake of circular cylinders", *Physics of Fluids*, **1**, 1611-1614.

Hammache M., Gharib M., 1991, "An experimental study of the parallel and oblique vortex shedding from circular cylinders", *J. Fluid Mech.*, **232**, 567-590

Hangan H., Kim J., 2003, "Aerodynamic slot-control for 2D square prisms", *Journal of Wind Engineering and Industrial Aerodynamics,* **91**, 1847-1857.

Hart D.P., 1998, “High-speed PIV analysis using compressed image correlation”, *Journal of Fluids Engineering*, **120**, 463.

Hart D.P., 1999, “Super-resolution PIV by recursive local correlation”, *Journal of Visualization*, 10.

Hirsch G., Ruscheweyh H., Zutt H., 1975. "Damage on a 140 m high steel stack due to wind-induced transverse vibration" (in German), Der Stahlbau, 2:33.

Hover F.S., Triantafyllou M.S., 1999. The effects of small wires on vortex-induced vibration parameters for cylinders. Flow-Induced Vibration ASME 389, 97-102.

Hover F.S., Triantafyllou M.S., 2000. Dependence of flow-induced vibration parameters on spanwise trip-wires. Flow Induced Vibration (ed. Ziada and Staubli), 91-96.

Hover F.S., Tvedt H., Triantafullou M.S., 2001, "Vortex-induced vibrations of a cylinder with tripwires", *J. Fluid Mech.*, **448**, 175-195.

Humble R.A., 2008, “Unsteady flow organisation of a shock wave/boundary layer interaction” *Ph.D. Dissertation*, Technical University of Delft.

Irwin P.A., 2010, "Vortices and tall buildings: A recipe for resonance", *Physics Today*, **63**(9), 68-69.

Igarashi T., 1986, "Effect of tripwires on the flow around a circular cylinder normal to an airstream", *Bull. Japan. Sic. Mech. Engng*, **29**, 2917-2924.

James D.F., Truong Q.S., 1972, "Wind load on cylinder with spanwise protrusion', *Proc. ASCE, J. Engng. Mech. Div.*, **98**, 1573-1589.

Jorgensen F.E., 2002, "How to measure turbulence with hot-wire anemometers; a practical guide", Dantec Dynamics.

Khoury, E., 2012, "The influence of end conditions on vortex shedding from a circular cylinder in sub-critical flow", *M.Sc Thesis*, Institute for Aerospace Studies, University of Toronto.

King R., 1977, "A review of vortex shedding research and its application", *Ocean Engineering*, **4**, 141-171.

Kumar R.A., Sohn C., Gowda B.H.L., 2008, "Passive control of vortex-induced vibrations: An overview", Recent Patents on Mechanical Engineering, **1**, 1-11.

Lekakis I., 1996, "Calibration and signal interpretation for single and multiple hot-wire/hot-film probes", *Meas. Sci. Technol.*, **7**, 1313-1333.

Lin C., Hsieh S.C., 2003, "Convection velocity of vortex structures in the near wake of a circular cylinder", *Journal of Engineering Mechanic*s, **129**, 1108-1118.

Lin C., Chiu P., Shieh S., 2002, "Characteristics of horseshoe vortex system near a vertical plate-base plate juncture", *Experimental Thermal and Fluid Science*, **27**, 25-46.

Lugt H.J., Vortex Flow in Nature and Technology, Wiley, 1972.

Luo S.C., Xia H.M., 2005, "Parallel vortex shedding at $Re=O(10^4)$ - a transverse control cylinder technique approach", *J. Fluid Mech.*, **541**, 143-165.

Maskell E.C., 1965, "A theory of the blockage effects on bluff bodies and stalled wings in a closed wind tunnel", Aeronautical Research Council Reports and Memoranda, R.&M. No: 3400.

Miller G.D., Williamson C.H.K., 1994, "Control of three-dimensional phase dynamics in a cylinder wake", *Experiments in Fluids*, **18**, 26-35.

Moffat R.J., 1988, "Describing the uncertainties in experimental results", *Experimental Thermal and Fluid Science*, **1**, 3-17.

Nakagawa K., Fujino T., Arita Y., Ogata Y., Masaki K., 1959, "An experimental investigation of aerodynamic instability of circular cylinder at supercritical Reynolds numbers", *Proc. 9th Jpn. Congr. Appl. Mech*., 235-240, Tokyo, Japan.

Nakagawa K., Fujino T., Arita Y., Shima K., 1963, "An experimental study of aerodynamic devices for reducing wind-induced oscillatory tendencies of stacks", *Symp. Natl. Phys. Lab.*, Teddington, UK, 774-795.

Narashimha R., Prasad S.N., 1994, "Leading edge shape for flat plate boundary layer studies", *Experiments in Fluids*, **17**, 358-360.

Naudascher E., Rockwell D., 2005. Flow-induced vibrations: an engineering guide. Dover Publications, Inc., Mineola, New York.

Nebres J.L.V., 1992, "Wake similarity and vortex formation for two-dimensional bluff bodies", *Ph.D. Dissertation*, Dept. of Aerospace and Mechanical Engineering, University of Notre Dame.

Nebres J., Batill S., 1993, "Flow about a circular cylinder with a single large-scale surface perturbation", *Experiments in Fluids*, **15**, 369-379.

Norberg C., Sunden, B., 1987, "Turbulence and Reynolds number effects on the flow and fluid forces on a single cylinder in cross flow", *Journal of Fluids and Structures*, **1**, 337-357.

Norberg C., 1994, "An experimental investigation of the flow around a circular cylinder: influence of aspect ratio", *J. Fluid Mech.*, **258**, 287-316.

Okamoto Y., Hanawa J., Kameoka T., 1971, "Visualization techniques of closed conduit flows by hydrogen bubble methods", *Bulletin of JSME*, **14**(76), 1088-1094.

Perry A.E., Chong M.S., Lim T.T., 1982, "The vortex shedding process behind two dimensional bluff bodies", *J. Fluid Mech.* **116**, 77-90.

Prasad A., Williamson C.H.K., 1997, "Three-dimensional effects in turbulent bluff-body wakes", *J. Fluid Mech.*, **343**, 235-265.

Raffel M., Willert C.E., Wereley S.T., Kompenhans J, 2007. Particle Image Velocimetry: a practical guide, 2nd Edition, Springer.

Rasmussen C.G., 1967, "The air bubble problem in water flow hot-film anemometry", DISA Info. No 5, 21-26.

Robinson S.K., 1991, "Coherent motions in the turbulent boundary layer", *Annu. Rev. Fluid Mech.*, **23**, 601-639.

Roshko A., 1954, "On the drag and shedding frequency of two-dimensional bluff bodies", *National Advisory Committee for Aeronautics*, Technical Note 3169.

Roshko A., 1955, "On the wake and drag of bluff bodies". *Journal of the Aeronautical Sciences* February, 124-132.

Roshko A., 1993, "Perspectives on bluff body aerodynamics", *Journal of Wind Engineering and Industrial Aerodynamics*, **49**, 79-100.

Ruscheweyh H., 1981, "Straked in-line steel stacks with low mass-damping parameter", *Journal of Wind Engineering and Industrial Aerodynamics,* **8**, 203-210.

Samways A.L., Ali J., Al-Deen M.F.N., Bruun H.H., 1994, "The calibration of and measurements with cylindrical hot-film probes in water flows", *Meas. Sci. Technol.*, **5**, 1551-1559.

Sahin B., Ozturk N.A., Akilli H., 2007, "Horseshoe vortex system in the vicinity of the vertical cylinder mounted on a flat plate", *Flow Measurement and Instrumentation*, **18**, 57-68.

Scarano F., Riethmuller M.L., 1999, "Iterative multigrid approach in PIV image processing with discrete window offset", *Experiments in Fluids*, **26**, 513-523.

Scarano F., Riethmuller M.L., 2000, "Advances in iterative multigrid PIV image processing", *Experiments in Fluids [Suppl.]*, S51-S60.

Schlichting H., 1968, *Boundary-Layer Theory 6th Edition*, McGraw-Hill Book Company.

Schraub F.A., Kline S.J., Henry J., Runstadler Jr. P.W., Littell A., 1965, "Use of hydrogen bubbles for quantitative determination of time-dependent velocity fields in low-speed water flows", Journal of Basic Engineering, 429-444.

Scruton C., Walshe D.E.J., 1957, "A means for avoiding wind-excited oscillations of structures with circular or nearly circular cross section", *Natl. Phys. Lab. Aero Rep. 335.*

Seal C.V., Smith C.R., Akin O., Rockwell D., 1995, "Quantitative characteristics of a laminar, unsteady necklace vortex system at a rectangular block-flat plate juncture", *J. Fluid Mech.*, **286**, 117-135.

Simpson R.L., 2001, "Junction flows", *Annu. Rev. Fluid Mech.*, **33**, 415-443.

Slaouti A., Gerrard J.H., 1981, "An experimental investigation of the end effects on the wake of a circular cylinder towed through water at low Reynolds numbers", *J. Fluid Mech.*, **112**, 297-314.

Stager R., Eckelmann H., 1991, "The effect of endplates on the shedding frequency of circular cylinders in the irregular regime", *Physics of Fluids*, **3**(9), 2116-2121.

Stansby P.K., 1974, "The effects of end plates on the base pressure coefficient of a circular cylinder", *Aeronautical Journal*, **78**, 36-37.

Szepessy, S., Bearman, P.W., 1992, "Aspect ratio and end plate effects on vortex shedding from a circular cylinder", *J. Fluid Mech.*, **234**, 191-217.

Szepessy, S., 1993, "On the control of circular cylinder flow by end plates", Eur. J. Mech., B/Fluids, **12**(2), 217-244.

Szepessy S., 1994, "On the spanwise correlation of vortex shedding from a circular cylinder at high subcritical Reynolds number", *Physics of Fluids*, **6**, 2406-2416.

Thomas A.S.W., 1987, "The unsteady characteristics of laminar junction flows", *Physics of Fluids*, **30**(2), 283-285.

Tritton D.J., 1959, "Experiments on the flow past a circular cylinder at low Reynolds numbers", *J. Fluid Mech.*, **6**, 547-567.

Van Atta C., Gharib M., 1987, "Ordered and chaotic vortex streets behind circular cylinders at low Reynolds numbers", *J. Fluid Mech.*, **174**, 113-133.

Visbal M.R., 1991, "Structure of laminar juncture flows", *AIAA Journal*, **29**(8), 1273-1282.

Vollmers H., 2001, "Detection of vortices and quantitative evaluation of their main parameters from experimental velocity data", *Meas. Sci. Technol.*, **12**, 1199-1207.

Warschauer K.A., Vijge J.B.A., Boschloo G.A., 1974, "Some experiences and considerations on measuring turbulence in water with hot-films", *Appl. Sci. Res.*, **29**, 81-98.

Weaver W., 1961, "Wind-induced vibrations in antenna members", *Proc. Am. Soc. Civ. Eng.*, **87**, 141-165.

Wei Q, Wang J.M., Chen G., Lu Z.B., Bi W.T., 2008, "Modification of junction flows by altering the section shapes of the cylinders", *Journal of Visualization*, **11**(2), 115-124.

Westerweel J., Dabiri D., Gharib M., 1997, "The effect of a discrete window offset on the accuracy of cross-correlation analysis of digital PIV recordings", *Experiments in Fluids*, **23**, 20-28.

Westerweel J., 1994, “Efficient detection of spurious vectors in particle image velocimetry data”, *Experiments in Fluids*, **16**, 236-247.

Willert C.E., Gharib M., 1991, “Digital particle image velocimetry”, *Experiments in Fluids*, **10**, 181-193.

Willert C.E., 1996, “The fully digital evaluation of photographic PIV recordings”, *Applied Scientific Research*, **56**, 79-102.

Williamson C.H.K., 1988, "Defining a universal and continous Strouhal-Reynolds number relationship for the laminar vortex shedding of a circular cylinder", *Physics of Fluids*, **31**, 2742-2744.

Williamson C.H.K., 1989, "Oblique and parallel modes of vortex shedding in the wake of a circular cylinder at low Reynolds numbers", *J. Fluid Mech.*, **206**, 579-627.

Williamson C.H.K., 1992, "The natural and forced formation of spot-like 'vortex dislocations' in the transition of a wake", *J. Fluid Mech.*, **243**, 393-441.

Williamson C.H.K., 1996, "Vortex dynamics in the cylinder wake", *Annu. Rev. Fluid Mech.*, **28**, 477-539.

Woodgate L., Mabey J.F.M., 1959, "Further experiments on the use of helical strakes for avoiding wind-excited oscillations of structures of circular or nearly circular section", *Nat. Phys. Lab.*, Teddington, UK, Aero Rep. No. 381.

Zabat M., Browand F.K., Plocher D., 1992, “In-situ swinging arm calibration for hot-film anemometers”, *Experiments in Fluids*, **12**, 223-228.

Zdravkovich M.M., 1981, "Review and classification of various aero- and hydrodynamic means for suppressing vortex shedding". *Journal of Wind Engineering and Industrial Aerodynamics,* **7**, 145-189.

Zdravkovich, M.M., 2003. Flow around circular cylinders. Oxford Science Publications Vol.2: Applications.

Zhou, T., Razali, S.F.M., Cheng, Z.H.L., 2011, "On the study of vortex-induced vibration of a cylinder with helical strakes", *Journal of Fluids and Structures*, **27**, 903-917.

App. A. **Uncertainty Analysis**

The analysis used in the quantification of the uncertainty associated with the determination of Strouhal number is based on the Root-Sum-Square (RSS) method proposed by Moffat (1988). This method evaluates the uncertainty in a certain quantity, R, which is a function of independent variables; x_1, x_2, ... , x_n. The basic equation of uncertainty analysis is given by Eqn. A.1, and is named as the root-sum-square equation. Here, the partial derivative term is referred to as the sensitivity coefficient of the relevant independent variable.

$$\varepsilon_R = \left\{ \sum_1^n \left(\frac{\partial R}{\partial x_i} \varepsilon_{x_i} \right)^2 \right\}^{1/2} \qquad \text{(A.1)}$$

App. A.1. Strouhal Number

The uncertainty in Strouhal number, where $St=fD/U_0$, is quantified by using RSS method. Applying Eqn. (A.1), one can derive the equation of uncertainty in Strouhal number as given in

Eqn. (A.2). $$\varepsilon_{St} = \left\{ \left(\frac{D}{U_0} \varepsilon_f \right)^2 + \left(\frac{f}{U_0} \varepsilon_D \right)^2 + \left(-\frac{fD}{U_0^{\,2}} \varepsilon_{U_0} \right)^2 \right\}^{1/2} \qquad \text{(A.2)}$$

In this equation, each of the terms within the square-root are associated with the contributions to the uncertainty in Strouhal number associated with the determination of the predominant frequency, cylinder diameter, and the free-stream velocity respectively. The uncertainty terms associated with each independent variable are taken as $\varepsilon_f = f_{aq} / 2n_{aq}$ (varies for different experimental techniques/setup), ε_D = 0.35mm, and ε_{U_0} = 1.25mm/s. On the other hand, the sensitivity coefficients depend on Reynolds number.

App. A.2. PIV Measurements

For the estimation of the random error in a single PIV measurement, RSS method is applied to Eqn. (A.3)

$$u = \frac{\Delta x}{\Delta t} \qquad \text{(A.3)}$$

used for the calculation of the velocity vector. Here, the uncertainty analysis is performed on the streamwise velocity component (u) but applies to the cross-flow velocity component (v) as well. The symbols Δx and Δt represent the displacement of the particles computed by the cross-correlation scheme and the time interval between Frame A and Frame B, respectively. The resulting uncertainty equation is given by Eqn. (A.4).

$$\varepsilon_u = \sqrt{\left(\frac{\partial u}{\partial \Delta x}\varepsilon_{\Delta x}\right)^2 + \left(\frac{\partial u}{\partial \Delta t}\varepsilon_{\Delta t}\right)^2} \qquad \text{(A.4)}$$

In Eqn. (A.4), the coefficients $\varepsilon_{\Delta x}$ and $\varepsilon_{\Delta t}$ are the sensitivity coefficients for the computed particle displacement and the time interval between the frames in a PIV recording. The displacement of the particles (Δx) are computed by Eqn. (A.5).

$$\Delta x = k(CC) \qquad \text{(A.5)}$$

The application of RSS method to Eqn. (A.5) yields the sensitivity coefficient for the particle displacement, which is given in Eqn. (A.6).

$$\varepsilon_{\Delta x} = \sqrt{\left(\frac{\partial \Delta x}{\partial k}\varepsilon_k\right)^2 + \left(\frac{\partial \Delta x}{\partial CC}\varepsilon_{CC}\right)^2} \qquad \text{(A.6)}$$

In Eqns. (A.5) and (A.6), the symbols k and CC represent the magnification factor and the pixel displacement computed from the cross-correlation scheme. The magnification factor ($k = l_c / n_c$) also has its associated uncertainty, given by Eqn. (A.7).

$$\varepsilon_k = \sqrt{\left(\frac{\partial k}{\partial l_c}\varepsilon_{l_c}\right)^2 + \left(\frac{\partial k}{\partial n_c}\varepsilon_{n_c}\right)^2} \qquad \text{(A.7)}$$

In Eqn. (A.7), l_c and n_c represent length scale used in PIV spatial calibration and the distance in pixels used in this length scale, respectively. Combining Eqns. (A.6) and (A.7) with (A.4), the uncertainty equation for a single PIV measurement is obtained, and given in Eqn. (A.8).

$$\varepsilon_u = \sqrt{\left\{\frac{1}{\Delta t}\sqrt{\left(k\varepsilon_{CC}\right)^2 + \left(CC\sqrt{\left(\frac{\varepsilon_{l_c}}{n_c}\right)^2 + \left(-\frac{l_c}{n_c^{\,2}}\varepsilon_{n_c}\right)^2}\right)^2}\right\}^2 + \left\{\frac{kCC}{\left(\Delta t\right)^2}\varepsilon_{\Delta t}\right\}^2} \tag{A.8}$$

According to these formulations, using $\varepsilon_{CC} = 0.1pixel$ (Raffel *et al.* 2007), $\varepsilon_{l_c} = 0.1\% l_c$ (Humble 2008), $\varepsilon_{n_c} = 0.1$ (Humble 2008), $\varepsilon_{\Delta t} = 0.4\%\Delta t$ (Humble 2008) and using the magnification factors given in the dissertation for different experimental configurations, the uncertainty in the PIV measurements are estimated as $0.026U_0$.

App. B. **Blockage Correction**

Blockage constraint on the flow past a bluff body was studied by Maskell, and a theoretical method was proposed for the correction of certain experimental values/results such as dynamic pressure, free-stream velocity, and vortex shedding frequency (Maskell 1965). The necessity of its application on the experimental data relies on the fact that the blockage imposed by the bluff body lead to significant changes on the upstream free-stream flow.

In this dissertation, his results were applied only to the vortex shedding frequency due to the increase in the free-stream velocity as a result of high blockage ratio in the experiments ($B = 8.3\%$) using Eqn. (B.1). In this equation, St_c, and k_c represent the corrected vortex shedding frequency, and corrected base parameter respectively. In order to calculate the values of the base parameters (k and k_c), which are calculated using Eqns. (B.2), and (B.3) respectively, the values of drag coefficient (c_D) and base pressure coefficient (c_{PB}) are taken from Hover *et al.* (2001), and Norberg (1994), respectively. Calculated values are given in table B.1 below.

$$St_c = (k_c/k)St \qquad \text{(B.1)}$$

$$k = \sqrt{1 - c_{PB}} \qquad \text{(B.2)}$$

$$k_c(k, B, c_D) = \sqrt{0.5\left(1 + k^2 - c_D B + \sqrt{(1 + k^2 - c_D B)^2 - 4k^2}\right)} \qquad \text{(B.3)}$$

Table B.1. Values of base parameters for the application of blockage correction

Re_D	k	k_c	k_c/k
5,000	1.40	1.3072	0.9337
10,000	1.45	1.3711	0.9455
15,000	1.46	1.3833	0.9474
25,000	1.46	1.3833	0.9474
30,000	1.48	1.4071	0.9507

App. C. **Estimation of the Boundary Layer Thickness**

The boundary layer thickness was estimated using a Blassius method, previously outlined by Nebres (1992), and can be summarized as following step-by-step procedure.

- Obtain the distribution of pressure coefficient around the cylinder; $c_P(\theta)$
- Calculate the circumferential distribution of the streamwise velocity at the boundary layer edge using Eqn. (C.1).
- Using a curve-fit, determine the values of u_1, u_2, and u_3 defined in Eqn. (C.2), where θ is given in radians.
- At each angular location of θ, construct the velocity profiles using Eqn. (C.3) where η is a non-dimensional variable defined by Eqn. (C.4) and its range is defined as $0 \le \eta \le 5.2$. The functions $f_1'(\eta)$, $f_3'(\eta)$, and $f_5'(\eta)$ are tabular functions given in Curle (1962).
- The value of η where $u(\theta, \eta)/U_0$ reaches 99% of the velocity at the boundary layer edge, i.e. $U(\theta)/U_o$, is denoted as η_{BL}. Using this value, the boundary layer thickness can be calculated using Eqn. (C.5).

$$U(\theta)/U_0 = \sqrt{1 - c_P(\theta)} \qquad \text{(C.1)}$$

$$U(\theta)/U_0 = u_1\theta + u_3\theta^3 + u_5\theta^5 \qquad \text{(C.2)}$$

$$u(\theta,\eta)/U_0 = u_1\theta f_1'(\eta) + 4u_3\theta^3 f_3'(\eta) + 6u_5\theta^5 f_5'(\eta) \qquad \text{(C.3)}$$

$$\eta = (y/D)\sqrt{2u_1\,\mathrm{Re}_D} \qquad \text{(C.4)}$$

$$(\delta/D) = \eta_{BL}\Big/\sqrt{2u_1\,\mathrm{Re}_D} \qquad \text{(C.5)}$$

App. D. **Discussion: Application of the Results**

The cross-sectional forces acting on the body, as a result of the imbalance in the surface pressure distribution, are drag force and lift force acting on the streamwise and cross-flow directions, respectively. The coefficients of these unsteady forces are given in Eqns. (D.1),

$$\overrightarrow{c_D}(t) = \left(\overline{c_D} + \tilde{c_D} \sin(4\pi f_K t) \right) \hat{i} \qquad \text{(D.1)}$$

and (D.2).

$$\overrightarrow{c_L}(t) = \left(\overline{c_L} + \tilde{c_L} \sin(2\pi f_K t) \right) \hat{j} \qquad \text{(D.2)}$$

In these equations, the symbols "~", and "‾" represent the amplitudes of the fluctuating, and the mean force coefficients respectively, and f_K denotes the vortex shedding frequency.

For a smooth circular cylinder, the mean-lift force is equal to zero due to two vortices being shed from the cylinder with opposite rotational direction with same amplitude per vortex shedding cycle. However, the mean-drag force coefficient depends on the Reynolds number and is well documented. While the major structural oscillations are occurring in the cross-flow direction at the vortex shedding frequency as a result of the fluctuating lift force, there are minor oscillations at twice the vortex shedding frequency in the streamwise direction due to the fluctuating component of the drag force. At this point, it is worthwhile to remember that the primary goal of flow control is to manipulate the flow structures such that the amplitudes of the fluctuating lift, and the mean drag force components are, in most cases, reduced, and/or the resonance conditions are avoided by manipulating the vortex shedding frequency.

As a starting point, let's focus on the changes in Strouhal number as the function of wire angle for a stationary cylinder. By simply attaching a tripwire on the cylinder surface within the range of effective wire angles ($\Delta\theta$), one can have control on the vortex shedding frequency to a significant degree. While manipulating the vortex shedding frequency, the wire can lead to different effects on the cross-sectional forces depending on the wire angle range selected. Two particular ranges of wire angle are important, i.e. $\theta_t \leq \theta \leq \theta_c$, and $\theta = \theta_{c2}$, and their implications are explained below (applicable to a stationary cylinder).

(i) For $\theta_t \leq \theta \leq \theta_c$: The increase in vortex formation length, and the decrease in the coherency of the shed vortices are expected to lead to a decrease in the base suction pressure on the cylinder, and, therefore, a reduction in the fluctuating lift, and drag forces induced by the shed vortices is expected. This statement is also supported by the force measurements by Hover *et al.* (2001) although the results in their experiments are related to the application of two tripwires symmetrically located around the cylinder. In addition, a reduction in the wake width also implies a reduction in the time-averaged momentum deficit in the wake region, and, together with the delayed separation from the wire-side, is an indirect indicator of mean drag reduction. Force measurements by Nebres (1992) and Nebres and Batill (1993) show a decrease in mean-drag, and increase in the mean-lift forces for this range of wire angles. The increase in the mean-lift force can be due to the asymmetric conditions in the final separation state of the boundary layer at either side of the cylinder; the boundary layer is turbulent prior to the final separation at the wire side, and is laminar at the smooth side of the cylinder.

(ii) For $\theta = \theta_{c2}$: The increased wake width, and decreased vortex formation length with amplified Karman shedding encountered in this wire angle range are expected to lead to significant increases in the amplitudes of the fluctuating lift and drag forces. In addition, the degree of asymmetry shown in the time-averaged flow structures with respect to the cylinder centerline is an indirect indicator of a non-zero mean-lift force. Although the increase in the amplitudes of the forces are, in general not desired, some applications can benefit from this range of wire angles as long as the structure is designed to withstand these forces; *(i)* energy harvesting in the wake of a circular cylinder with the use of piezoelectric materials, and *(ii)* the first column of tubes in a heat exchanger bundle for enhanced heat transfer.

As a unidirectional flow control method, the effects of a single tripwire on the flow control is sensitive to the changes in the free-stream direction since it would affect the wire angle. Based on the experimental data, the above-mentioned changes in the flow for $\theta_t \leq \theta \leq \theta_c$ can be achieved within a maximum tolerance of ±9° for the changes in the flow direction. In case the application is at a different Reynolds number and/or wire size used in this study (or Nebres'), the established estimation model can also be used. On the contrary, the range of the wire angles for $\theta = \theta_{c2}$ is rather constant and is given by $50° \leq \theta_{c2} \leq 70°$, thus giving a tolerance of approximately ±10° for the changes in the flow direction when the wire is place at $\theta = 60°$.